The Dissertation Committee for Eric M. Matzel

Certifies that this is the approved version of the following dissertation:

The Anisotropic Seismic Structure of the Earth's Mantle:

Investigations using Full Waveform Inversion

Committee:

_____

Stephen Grand, Supervisor

_____

Cliff Frohlich

_____

Douglas Smith

_____

Paul Stoffa

_____

Clark Wilson

The Anisotropic Seismic Structure of the Earth's Mantle: Investigations using Full Waveform Inversion

by

Eric M. Matzel, B.S., M.A.

Dissertation

Presented to the Faculty of the Graduate School of

the University of Texas at Austin

in Partial Fulfillment

of the Requirements

for the Degree of

Doctor of Philosophy

The University of Texas at Austin

December, 2002

Acknowledgements

I would like to thank the many people who directly and indirectly helped make this work possible. First of all, I would like to thank my family who have always encouraged me to pursue my goals and supported my education. My father, in particular, inspired me with his own love of science and discovery.

My supervisor, Dr. Stephen Grand, taught me the essentials necessary to work in seismology and to understand and interpret seismic data. He helped flesh out ideas for this Dissertation project and encouraged me to work on seismic inversion. He also encouraged me to present and publish my findings.

Brian Schlottmann and Tom Johnson provided hours of discussions on science, politics and life in general and helped keep my time at U.T. interesting.

Finally, I'd like to thank Jennifer, who allowed me to talk for hours about seismic anisotropy without ever looking bored.

The Anisotropic Seismic Structure of the Earth's Mantle:

Investigations using Full Waveform Inversion

Publication No. _____

Eric M. Matzel, Ph.D.
The University of Texas at Austin, 2002

Supervisor: Stephen P. Grand

I have developed a waveform inversion procedure to invert 3 component broadband seismic data for models of the anisotropic seismic structure of the Earth and applied the technique to an investigation of wave propagation through anisotropic media and earthquake data sampling the upper mantle beneath the East European platform. The procedure combines the conjugate-gradient and very fast simulated annealing methods and attempts to minimize a cross-correlation misfit function comparing data to synthetic seismograms. A series of inversion passes are performed over a range of frequency and time windows to progressively focus in on structural details. The intent is to obtain P and S velocity models that simultaneously match all components of the data (radial, vertical and tangential). The variables in the problem are the seismic velocities (α and β) as a function of depth. When radial anisotropy is required this set is expanded to include the five variables that determine the seismic velocities in a radially anisotropic medium (α_h, α_v, β_h, β_v, η).

I investigate the propagation of seismic waves through radially anisotropic media, evaluate which elements of radial anisotropy are best resolved by seismic data and discuss strategies for identifying radial anisotropy in the Earth. S anisotropy, $\beta\%$, and the horizontal component of P velocity, α_h, are typically well resolved by multicomponent seismic data. P anisotropy, $\alpha\%$, and η are often poorly resolved and trade off with one another in terms of their effect on S_V arrivals. Erroneous structure will be mapped into models if anisotropy is neglected. The size of the erroneous structure will be proportional to the magnitude of anisotropy present and extend well below the anisotropic zone. The effects of anisotropy on P

models produced with an isotropic assumption are most similar to the effects on isotropic S_H models. When comparing isotropic models, α/β_{sh} is therefore often a better measure than α/β_{sv} for characterizing mantle petrology. Isotropic S_H, S_V and P models developed separately using the same data set can provide a good initial estimate of the presence, location and magnitude of anisotropy and those results can be used to create an initial model for an anisotropic inversion solving simultaneously for all 3 components of the data.

       Finally, I present models for the P and S velocity structure of the upper mantle beneath the East European platform including an analysis of radial anisotropy. The data are 3-component broadband seismograms from strike-slip earthquakes located near the edge of the platform and recorded in Russia and Europe. The timing, amplitude and interference characteristics of direct arrivals (S, P), multiply reflected arrivals (SS, PP), converted phases and surface waves provide very good radial resolution throughout the upper 400 km of the mantle. The platform is underlain by a radially anisotropic seismic mantle lid extending to a depth of 200 km with a largely isotropic mantle below. The model has a positive velocity gradient from 41 km to 100 km depth, and a relatively uniform velocity structure from 100 km to 200 km depth with high S_H and P_H velocities (4.77 km /s, 8.45 km/s). Shear anisotropy is uniform at 5% ($\beta_H > \beta_V$) from 41 to 200 km depth, drops to 2% from 200 to 250 km and is isotropic below that. The average shear velocity from 100 to 250 km is also uniform at 4.65 km/s and the drop in anisotropy is matched by a drop in β_H to 4.70 km/s combined with an increase in β_V to 4.60 km/s. Below 250 km there is a positive velocity gradient in both P and S velocity down to 410 km. P anisotropy is not well resolved, but P structure mimics the S_H velocity structure, suggesting that P is also anisotropic within the lid.

Table of Contents

Chapter 1

Introduction

Seismic waves provide the most direct measurement of the properties of the interior of the Earth and are sensitive to the thermal, petrological and tectonic structures they pass through. High-resolution models of the seismic structure of the Earth are necessary to gain a full understanding of how the Earth evolves over time. The data obtained by seismic networks contain a wealth of information, but much of that information has not been deciphered because of the difficulties involved. The interpretation of seismic waves is complicated because several variables contribute to the final shape of the waveform at the receiver. These variables include the P and S velocities (α, β) and density (ρ) throughout the rock sampled by the waves. The mineralogy, chemical composition, and temperature of the medium through which the seismic wave travels influence these variables in different ways. If a coherent orientation is present (such as fine layering or mineral alignment), then seismic anisotropy will also be important. Due to computational limitations, may studies of the interior of the Earth use only a portion of the available data.

The mantle is commonly divided into several layers based on radial discontinuities and gradients in the seismic velocity structure (Anderson, 1989). These include the lithosphere, asthenosphere, transition zone and lower mantle. The lithosphere consists of the crust and the shallowest part of the mantle that move coherently over geologic time. The asthenosphere underlies the lithosphere, is weak and flows plastically under geologic stresses. A negative seismic velocity gradient in the upper mantle is typically identified by seismologists as the lithosphere-asthenosphere boundary. The depth of the lithosphere-asthenosphere boundary varies widely as a function of tectonic province, from essentially zero at mid ocean ridges to several hundred kilometers beneath continents. Silver (1996) suggests that the asthenosphere vanishes beneath continents and that continental plates are directly coupled to the mantle below. The transition zone is defined by two seismic discontinuities at 410 and 660 kilometers depth. Figure 1 illustrates the radial structure of the Earth.

Gradients and discontinuities in seismic velocity are attributed to different causes. Gradients can occur simply as a result of increasing pressure and temperature, without

1

requisite changes in composition or mineralogy. Sharp changes in mineralogy, mineral phase, or chemical composition create discontinuities. There are three global seismic discontinuities of interest in this study: the Moho, the 410 km depth discontinuity and the 660 km depth discontinuity. These last two discontinuities represent several-percent increases in P and S velocities over a few 10's of kilometers in depth. The 410 km discontinuity is believed to be due to a phase transition from α-olivine to the β-spinel structure, whereas the 660 km discontinuity is believed to be an endothermic phase change from γ spinel structure to a perovskite structure and magnesiowustite (Agee, 1993; Weidner and Ito, 1987). It is still debated whether convection within the mantle crosses the 660 km discontinuity or whether the upper and lower mantle are unmixed, a question which requires accurate measurements of the magnitude, depth and sharpness of the boundary. In addition to these global discontinuities, regional studies have found evidence for smaller local discontinuities, most notably at 220 km beneath continents and at 520 km within the transition zone. For the purpose of this study, the shallow mantle is defined as the mantle above the global discontinuity at 410 km. The transition zone is the region between the 410 km and 660 km discontinuities. The lower mantle is everything below the 660km discontinuity and above the core-mantle boundary. This study will produce seismic models for the shallow mantle and the transition zone.

Recent research in experimental mineralogy allow us to interpret seismic models in terms of possible mantle mineral compositions (Anderson and Bass, 1984; Bass and Anderson, 1984; Duffy and Anderson, 1989; Li et al., 1998b, 1998c; Knoche et al., 1998; Weidner and Ito, 1987; Ita and Stixrude, 1992). These experiments involve measurements of the elastic moduli of single crystals and crystal aggregates at mantle pressures and temperatures. Bulk and shear moduli can be directly related to seismic velocity of each mineral phase with respect to depth. The density of the mineral phases can also be directly measured. The average seismic velocity and density at any depth is a combination of the velocities and densities of the minerals present. Seismic profiles can be created based on lab data and compared to seismic observations to develop a compositional model (figure 2). Petrologic models have been developed which explain the first-order seismic structure, but questions still remain as to whether the mantle is homogeneous or chemically stratified. Two possible models are pyrolite (Ringwood, 1975) and piclogite (Bass and Anderson, 1984).

2

Radial structure of the upper mantle

Crust

Moho

Lithosphere/Asthenosphere

220

Transition Zone

410

520

660

Lower Mantle

0

100

200

300

400

500

600

700

800

900

1000
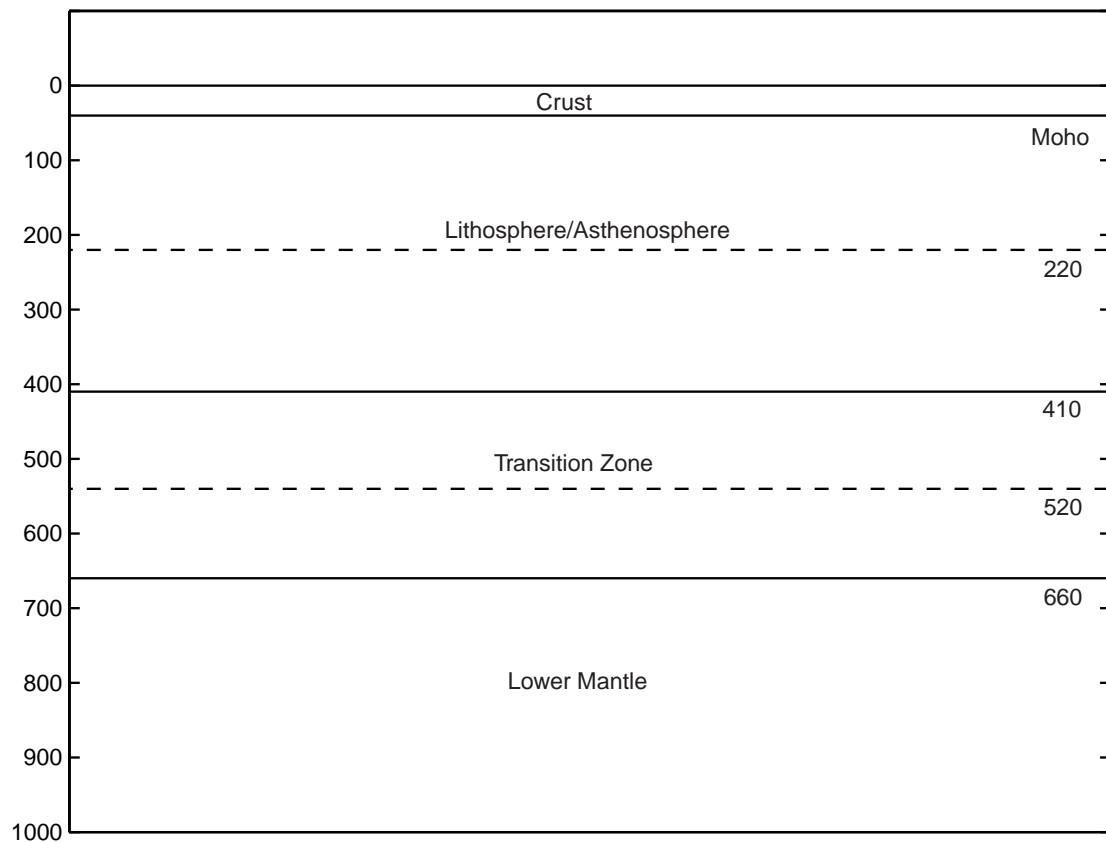
Figure 1. The radial structure of the upper mantle with major discontinuities identified. The dashed lines at 220 km and 520 km indicate that these discontinuities are not universally observed.

Figure 2. P and S velocities calculated for various mantle minerals and compared to seismic models (GCA, CJF, SNA, TNA). Olivine (ol), grossularite (gr), jadeite (jd), majorite (mj), perovskite (pv), and ilmenite (il). Na, Mg and Ca indicate sodium, magnesium and calcium rich members (from Duffy and Anderson, 1989)

Pyrolite is an olivine rich (> 60%), model which identifies the 410 and 660 discontinuities strictly as phase boundaries. The piclogite model contains significantly less olivine (< 40%). Neither model provides an exact ma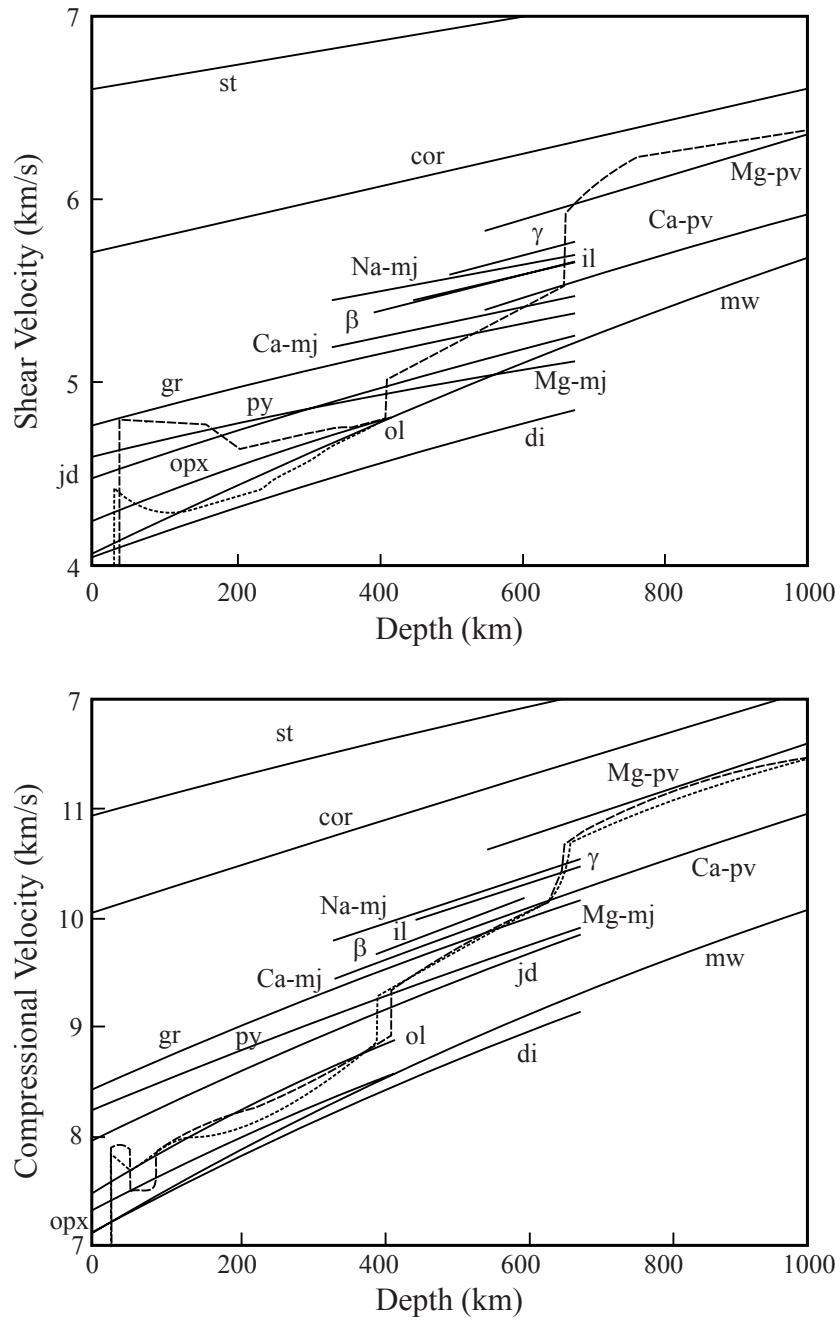tch to published seismic velocity models. The 410 km discontinuity predicted by piclogite is much smaller than observed and the gradient within the transition zone is correspondingly too large. Pyrolite does a better job predicting the 410 km jump, but predicts a steep gradient in the transition zone. Each predicts a velocity jump near 520 km, but the jump is much larger in the piclogite model. Many experimental petrologists prefer the pyrolite model for its fit to the observed density and bulk sound velocity of the upper mantle and transition zone (Ita and Stixrude, 1992; Ming et al., 1992). Gaherty et al. (1999) also concludes that the detailed structure of the 410 km discontinuity requires a high-olivine (55%) pyrolite-like composition. In contrast, piclogite is often found to be a better fit for the observed properties of the transition zone (Estabrook and Kind, 1996; Bass and Anderson, 1984). Part of the uncertainty is that the experimental work is still incomplete. Many of the predicted phase assemblages have not yet been reproduced in the lab, and consequently the predicted densities and velocities associated with them are estimates based on other work (Ming, 1992). Until recently, lab measurements were made at ambient temperatures and moderate pressures and the differentials were extrapolated incurring errors of a few percent (Knoche et al., 1998). Furthermore, the size of the discontinuity at 410 km and the transition zone gradient are so sensitive to the amount of olivine present that uncertainties in seismic measurements allow a wide range of petrologic solutions.

Seismic Phases

Seismic data provide a tremendous amount of information about the Earth's interior. Each seismogram includes direct and multiply reflected arrivals, converted phases and surface waves. The data are extremely complicated by the large number of arrivals present and this makes it difficult to fully utilize seismic data. Many studies use only a small portion of the data available, focusing on travel times or specific phases for instance, discarding the rest or treating it as noise. As computation speeds have increased and methods for generating full response synthetics have been developed, more of the data have been accessible to

interpretation. In this study, I use the full waveform, from the start of the first body wave through the surface waves in an inversion to calculate models of mantle structure.

One consequence of the sharp increases in velocity at 410 and 660 km is that several direct body waves sampling different depths in the Earth can arrive at the same receiver. At the teleseismic distances in this study the direct arrivals S and P and multiple phases SS and PP traveling above the 410 km discontinuity and above the 660 km discontinuity can all be readily observed on the seismograms (figure 3). The timing, amplitude, and interference characteristics of these phases provide excellent constraints on the seismic structure of the upper mantle. These are used as first order constraints in the seismic inversion.

Love and Rayleigh surface waves provide some of the best constraints of the very shallowest part of the mantle (less than about 200 km depth). Velocity profiles can be made based on the phase or group velocities of these phases as a function of frequency. A mismatch between the Love and Rayleigh wave travel times also provides an excellent measurement of anisotropy (Forsyth, 1975; Regan and Anderson, 1984).

The vertical, radial and tangential components of the data are measurements of the 3 dimensional displacement oriented with respect to the direction between source and receiver. Each component is sensitive to different seismic phases. The tangential component isolates purely S_H motion and contains only S body phases and Love waves and has been used extensively to obtain S wave structure in the Earth. The radial and vertical components contain both P and S_V components including the Rayleigh waves.

Figures 4 and 5 demonstrate the ability of seismic data to discern both the extent and location of structural anomalies in the mantle. In the first case (figure 4), synthetics for 2 models (A and B) are compared to a reference model at 3 different frequencies. Resolution is highly dependent on the frequency band used. A seismogram that appears very simple at low frequency may appear very complex if the high frequency cutoff is increased. Long wavelength data are most sensitive to the average velocity structure and to the velocity gradients. The additional arrivals seen at the higher frequencies are very sensitive to the fine details of the model. Seismic data are also quite sensitive to the location of structural anomalies (figure 5). A small perturbation at the top of the mantle (A) has a very different affect on the seismograms than a similar perturbation at depth (B).

Seismic Anisotropy in the Earth's Mantle

In an anisotropic medium, physical properties vary as a function of direction. Seismic waves travel through such a medium at velocities that vary as functions of polarization and direction of propagation. Anisotropy is an inherent feature of most minerals and mineral assemblages found in the upper mantle (Kern, 1993; Nicolas and Christensen, 1987). These anisotropies tend to average out over the large scale if individual crystals are oriented randomly, however, if some force tends to align them, the medium as a whole can become anisotropic.

Seismic anisotropy in the upper mantle is typically attributed to the alignment of the mineral olivine due to tectonic forces (Artyushkov, 1984; Anderson, 1989). This implies that measurements of anisotropy are measurements of mantle flow and deformation history. A critical element lacking from most analyses of seismic anisotropy is an explicit demonstration of the location and depth extent of the anisotropy. This is important because anisotropy can be a result of relict flow frozen into the lithosphere or active deformation in the asthenosphere. In the first case it represents an historical record of tectonism, in the second it is a picture of present day convection.

It is also important to consider anisotropy when comparing different seismic models. S models, for instance, often focus on either the radial component (S_V) or tangential component (S_H) of the data, but this is not always stated explicitly. When comparisons are made between such models, variations may be interpreted as fundamental differences in Earth structure. If the subsurface is isotropic this is unimportant, if anisotropic it can lead to erroneous conclusions. Neglecting anisotropy can also bias isotropic models because the velocity is a function of incidence angle in anisotropic media (Regan and Anderson, 1984).

Seismic studies generally have concluded that the upper mantle is highly anisotropic, but the location, extent and magnitude of this anisotropy is uncertain (Ekstrom and Dziewonski, 1998, Montagner and Tanimoto, 1991; Gaherty and Jordan, 1995). The anisotropy is often represented as a transversely isotropic layer with a vertical symmetry axis with several percent differences between the vertical and horizontal seismic wave speeds. Anisotropy is typically observed by measuring the mismatch of Love and Rayleigh surface waves or the relative arrival times of body wave phases such as S_H and S_V. Surface wave

measurements have poor resolution below about 200 kilometers depth, and measurements of body wave phases integrate the effects of anisotropy along the entire path length. Travel paths that pass through different tectonic regions of the mantle also often complicate the data.

Figure 6 illustrates how anisotropy can be observed in seismic data. Tangential and radial component synthetics are plotted for a simple Earth model. The solid lines are the isotropic model results. The dashed lines are for the same model with β_v 2% slower from the Moho to 220 km. The tangential component synthetics are affected, but to a smaller degree than the radial component. Note, in particular, the large delay in the Rayleigh wave relative to the Love wave. This discrepancy between Love and Rayleigh waves is the observation most often used to identify anisotropy in the upper mantle, and is most sensitive to the shallow part of the mantle. A mismatch between the S_H and S_V body wave arrivals is more difficult to detect, but is also used to identify radial anisotropy. Figure 7 demonstrates that the location and extent of anisotropy are also resolvable with seismic data. Note that the delay in the Rayleigh waves is a characteristic of shallow anisotropy and that determining the depth extent of anisotropy relies in part on measuring the timing of the body wave arrivals. In figure 7a, a model with anisotropy from the Moho to 220 km is compared to a model with anisotropy from 220 to 410 km. Note the large shift seen in the Rayleigh wave arrival is not present in the model with a deep anisotropic layer, but the delay in the SS arrival is still present. Figure 7b compares a model with anisotropy from the Moho to 220km with a model with anisotropy from the Moho to 410 km. Notice that the Rayleigh wave shift is very similar for both cases, but a measurable shift can be seen in the SS arrivals. Finally, figure 7c compares the case with shallow anisotropy to a case with anisotropy exclusively in the transition zone. A very large difference is seen in the SS travel time between the two cases.

Upper Mantle Models

Studies of the Earth's upper mantle have found a general relationship between the tectonic age of the crust and the velocity structure of the underlying mantle, with the highest velocities associated with the ancient cratons and the lowest velocities found beneath oceanic spreading centers and continental tectonic belts. Common features include the presence of a seismic high velocity region at the top of the mantle overlying a region of decreased

8
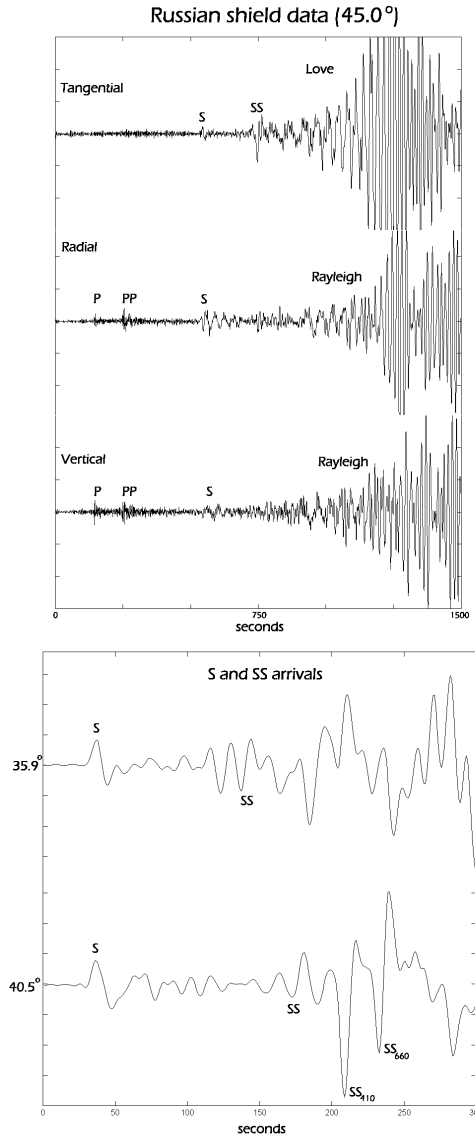
Figure 3. (top) Unfiltered tangential, radial and vertical component data for a shield path at 45° distance. Major arrivals are identified for reference including the Love and Rayleigh surface waves.

(bottom) S and SS arrivals identified on the tangential component of 2 shield seismograms (low-pass filtered with a corner frequency at 100 mHz). The subscripts 410 and 660 identify arrivals produced by the sharp jumps in velocity at those depths.
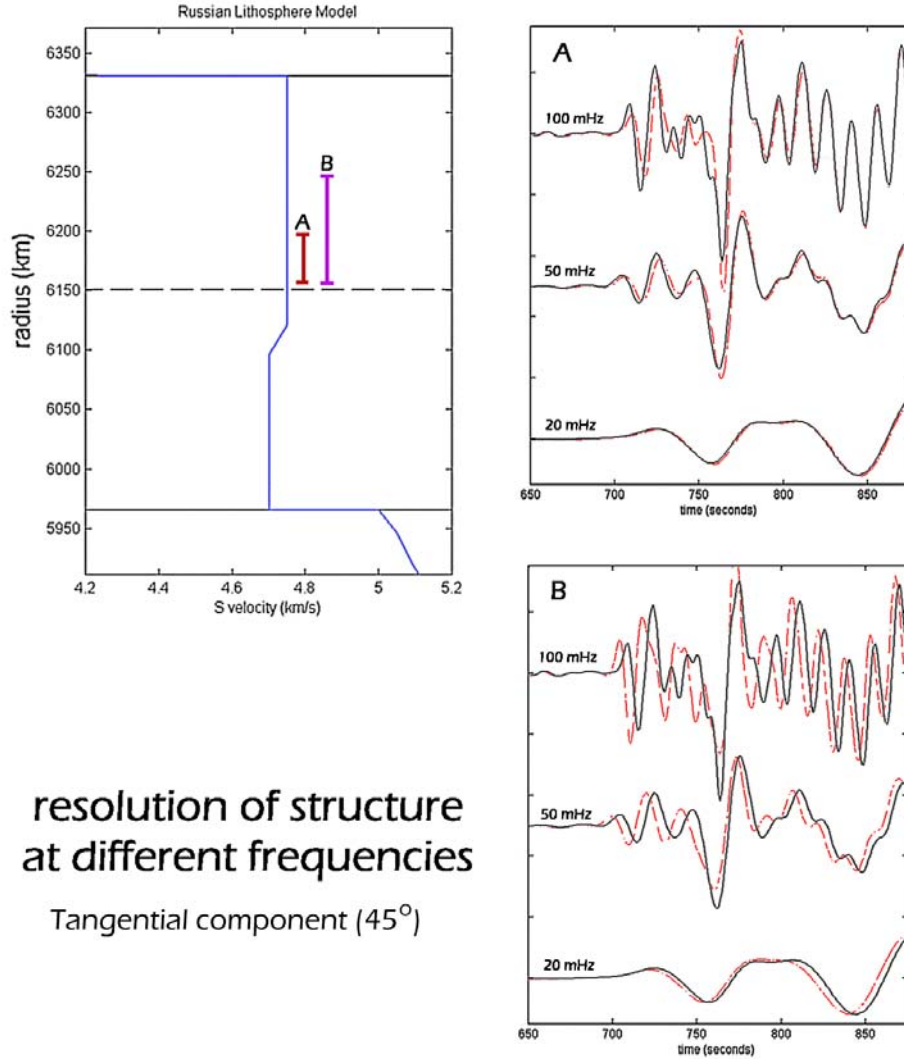
Figure 4. Sensitivity of data to seismic structure at different frequencies. 3 models are compared, a reference model and 2 perturbations to that model (A and B). Model A has a 1% increase in velocity compared to the reference model over the 50 km range shown. Model B has a 1% increase in velocity over a 100 km range. Tangential component synthetics for the reference model (solid lines) are compared to those for the model perturbations (dashed lines) to illustrate the resolvability. The traces are plotted at 3 different bandwidths, with the high corner cutoff frequency indicated. The source-receiver offset is 45°.

resolution of structure at different depths
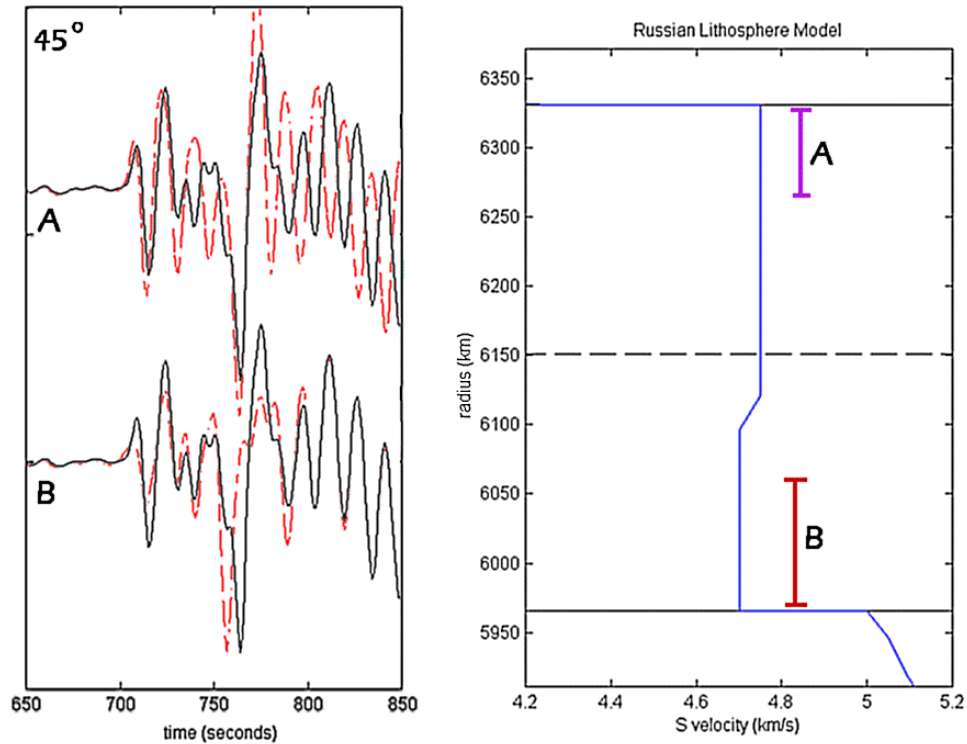
Figure 5. Resolvability of structure at different depths. 3 models are compared, a reference model and 2 perturbations to that model (A and B). Model A has a 1% increase in velocity at the top of the mantle compared to the reference model. Model B had a 1% increase in velocity at the bottom of the mantle. Tangential component synthetics for the reference model (solid lines) are compared to those for the model perturbations (dashed lines). Note that different portions of the seismograms are affected in the two cases.
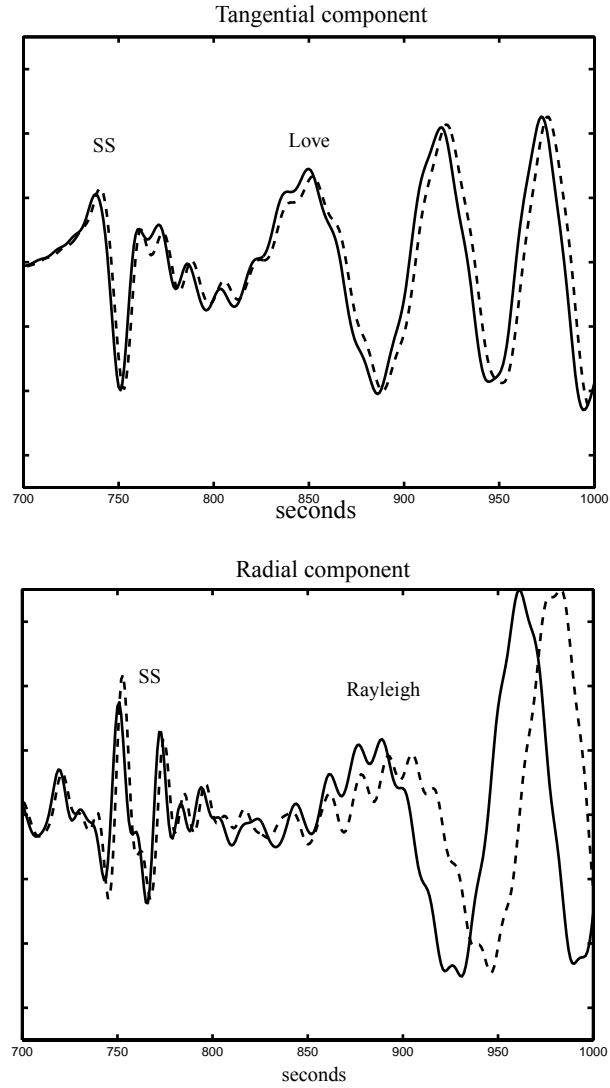
Figure 6. Sensitivity of data to anisotropic structure. Tangential and radial component synthetics are plotted for an isotropic model (solid lines) and a radially anisotropic model (dashed lines). The source-receiver offset is 44°. Major arrivals are identified for reference. Each model (isotropic and anisotropic) has the same β_h structure. β_v is 2% slower than β_h from the Moho to 220 km depth in the anisotropic model

    (a) Tangential component synthetics

    (b) Radial component synthetics, $\eta = 0.90$
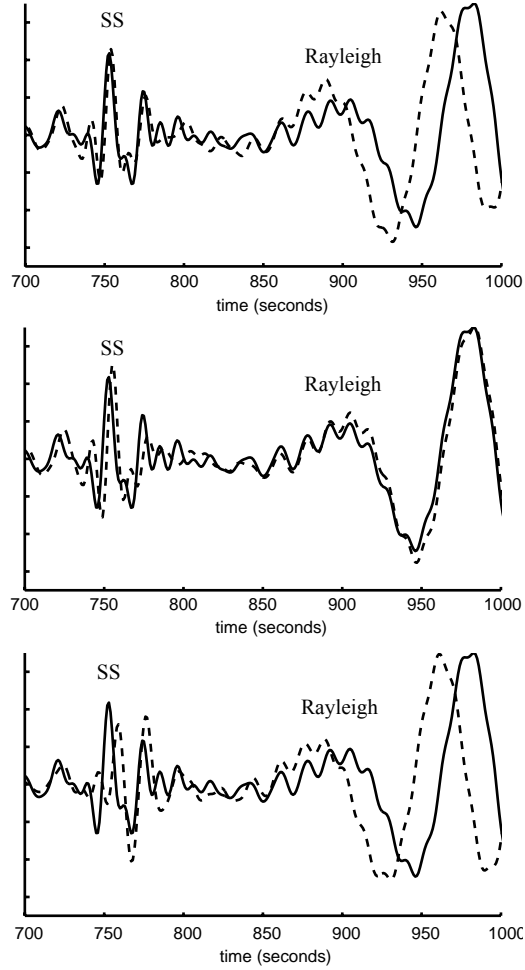
Figure 7. Sensitivity of data to the location and extent of anisotropy. Radial component synthetics for the anisotropic model shown in figure 6 (solid lines) are plotted relative to 3 other anisotropic models (dashed lines). Each model has the same β_{sh} structure and tangential component synthetics are very similar to one another. In each case the solid line is a synthetic for a model with 2% anisotropy from the Moho to 220 km depth.

   (a) 2% anisotropy from 220 – 410 km depth (no anisotropy from the Moho to 220km)

   (b) 2% anisotropy from the Moho to 410 km depth

   (c) 2% anisotropy from 410 – 660 km depth (no anisotropy above 410 km)

13

velocities. These are referred to respectively as the seismic lid and low velocity zone (LVZ). The stable ancient cratons are typically underlain by deep high velocity root systems including fast seismic lids extending to 200 km or more. Phanerozoic regions have thinner lids and lower velocities and recently active regions have essentially no seismic lid and extremely low velocities. Beneath continents, velocity variations of several percent can extend down to the 410 km discontinuity or even deeper. This is illustrated in figure 8.

The relationship between seismic velocity and tectonic age is most easily understood for oceanic regimes, where it appears to be directly related to the thickening of the lithosphere as the plate cools. Velocities are slowest directly beneath the spreading ridges and increase rapidly with the age of the plate (figure 9). The increase in velocity occurs first in the shallowest portion of the plate and propagates down over time resulting in the formation of a fast seismic lid over a LVZ. Forsyth (1975) first observed that the lid thickness is proportional to the square root of the age of the plate, more than doubling in thickness between 5 and 10 Ma. The results of his study of the Nazca plate have been largely reproduced by other researchers in studies of the Pacific ocean, Fiji trough, Philippean Sea and Atlantic ocean (Leeds, 1975; Regan and Anderson, 1984; Gaherty et al., 1999; Xu and Wiens, 1997; Grand and Helmberger, 1984b; Zhao and Helmberger, 1993). Most of the lateral heterogeneity in the oceanic mantle is due to the variations in lid thickness and velocity. The mantle below the lid is much more homogeneous, suggesting that it is free to mix over geologic time scales. Together, these observations suggest that the lid represents both a thermal and mechanical boundary layer. The thickening lid is believed to be the lithosphere and the underlying LVZ is thought to be a zone of partial melting.

Beneath continents the situation is more complicated. The general relationship of higher velocities under older regimes still holds, but there is more variability between provinces of similar age. As in oceanic regions, the seismic lid is associated with the thermal state of the mantle. The lid is thickest beneath the cold, stable cratons, reaching 200-250km depth. There is virtually no lid beneath active, tectonic areas (Grand and Helmberger, 1984a; Walck, 1984). Unlike the oceanic case, however, there are large variations in mantle velocity below the lid, suggesting that the thermal and mechanical boundary layers are decoupled. Deep roots of high P and S velocity lie beneath the Archaen cratons and extend well below the mantle lid (Given and Helmberger, 1980; Grand and Helmberger, 1984a; Paulssen, 1987;
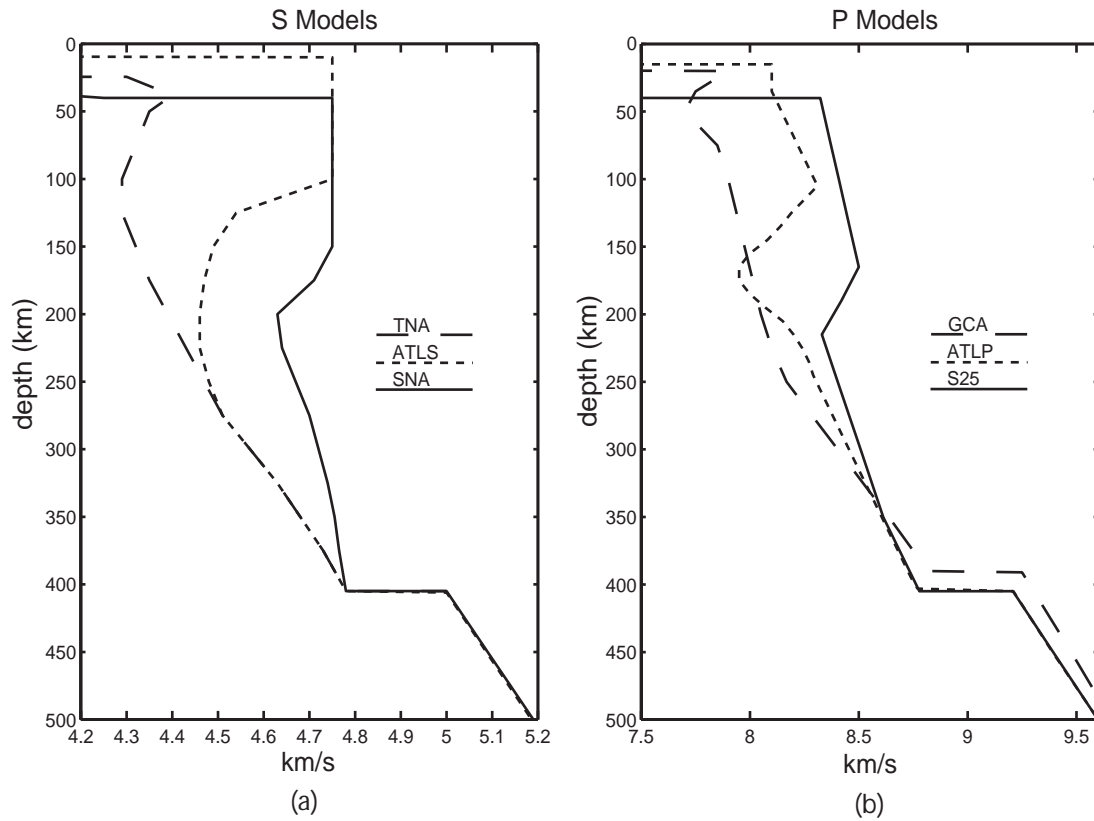
Figure 8. (a) Upper mantle S models for 3 tectonic regimes: a continental craton (SNA, Grand
and Helmberger, 1984a), a tectonically active continent (TNA, Grand and Helmberger,
1984a), and an oceanic region (ATLS, Grand and Helmberger, 1984b).(b) P models for the
same regions: (S25, Lefevre and Helmberger, 1989; GCA, Walck, 1984; ATLP, Zhao and
Helmberger, 1993)
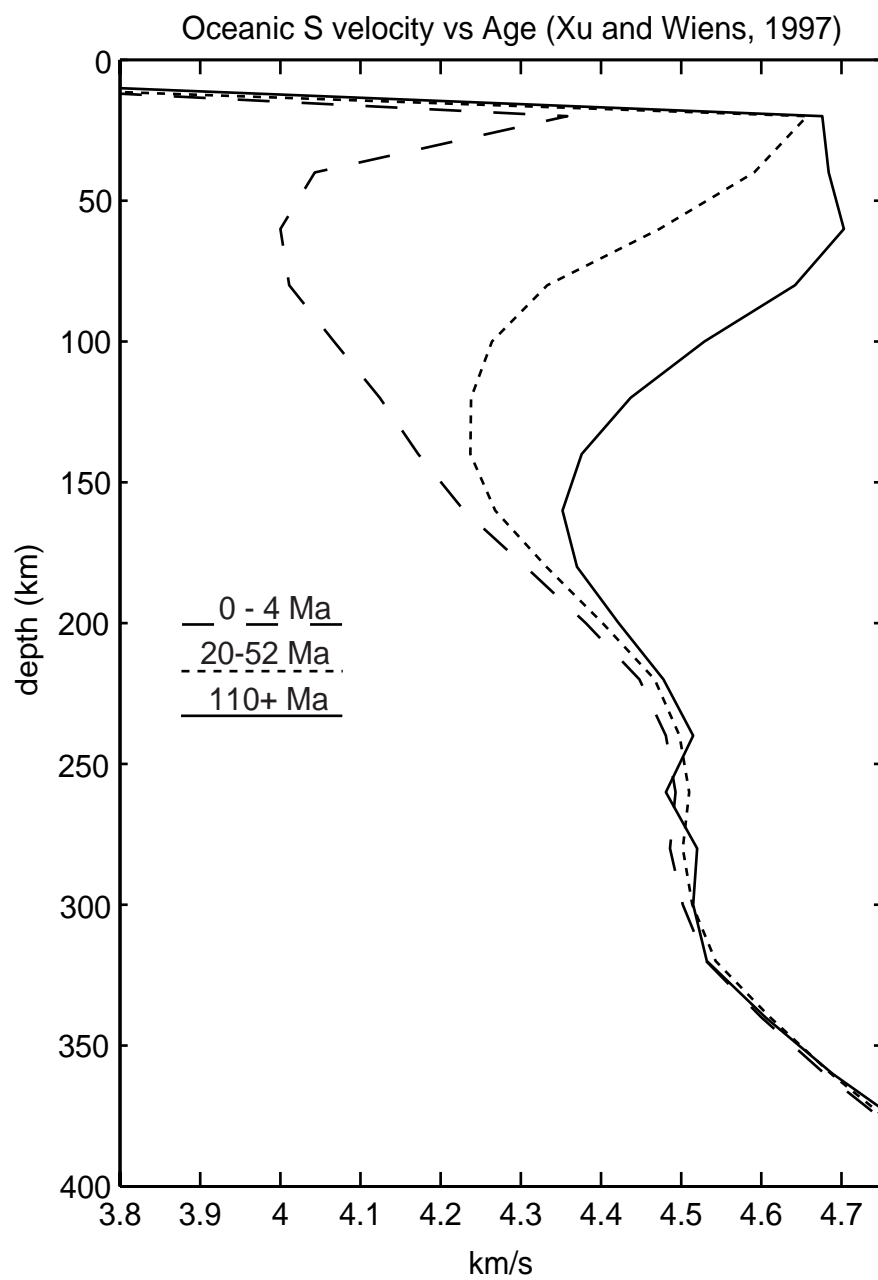
Figure 9. Oceanic upper mantle structure as a function of the age of the plate. (Xu and Wiens, 1997)
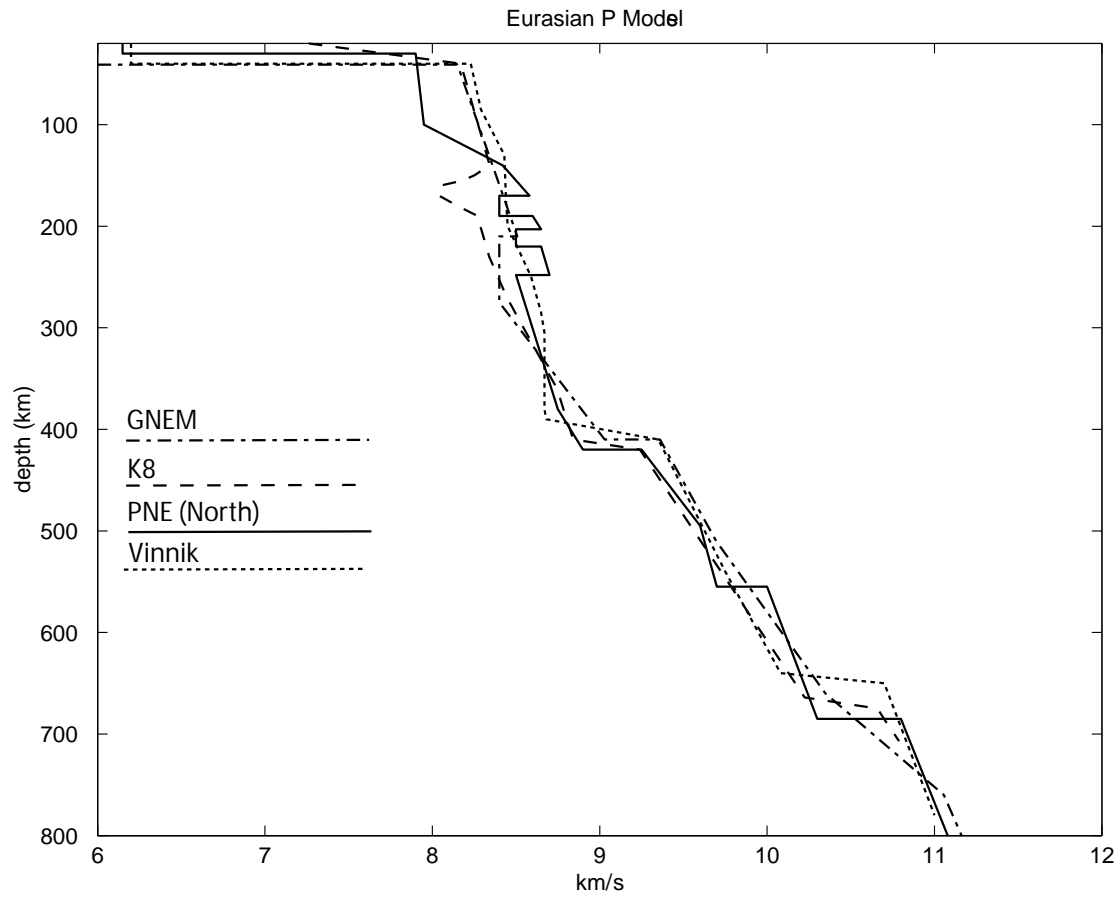
Figure 10. A comparison of several P models for Eurasia. GNEM (Ryberg et al., 1995), PNE-North (Mechie et al., 1993), and Vinnik (Vinnik and Ryaboy, 1981) were obtained using data from the Peaceful Nuclear Explosions experiment conducted in the Soviet Union. K8 (Given and Helmberger, 1980) used earthquake sources.

Lefevre and Helmberger, 1989; Vinnik, et al., 1996, Priestley, 1999) . This suggests that the tectonic plates may reach hundreds of kilometers in thickness in places. Jordan (1975) refers to the region of the Earth that moves coherently during plate tectonics as the tectosphere. He interprets the deep cratonic roots as evidence that cratons are compositionally distinct from the surrounding mantle, allowing them to remain stable on geologic time scales. Anderson (1995) points out that another interpretation is that the roots represent cold mantle downwellings.

The structure of both P and S velocity models show heterogeneity in the upper several hundred kilometers, related to tectonic regime. The details differ, however, and questions remain about how to relate the two. In particular, LVZ's are more consistently found in S models than in P models, and often vary in thickness and location when found in both. Part of the problem is that most studies still model either S or P structure only, and differences in the data and methodology used make direct comparison of the structures difficult. The relationship between S and P velocity is important, because a drop in S velocity without a corresponding drop in P velocity may indicate the presence of partial melt. That is the interpretation of Rodgers and Bhattacharyya (2001) who modeled both P and S structure for the central U.S. and found a shear LVZ, but none for P. However, Gaherty et al. (1999) identified both a P and S LVZ beneath Australia related to the transition from anisotropic to isotropic mantle.

Some of the most detailed P velocity models were obtained using data from the Peaceful Nuclear Explosions (PNE) experiment conducted in the 1970's and 1980's in the Soviet Union. The experiments allowed them to collect 3-component short period P-wave data for long-range profiles covering much of the Siberian and Russian platforms. 1-D and 2-D models of these profiles been developed to investigate the structure of the upper mantle and transition zone and indicate significant vertical and lateral heterogeneity throughout the region (figure 10) (Mechie et al., 1993, Morozova et al., 1999, Pavlenkova and Yegorkin, 1983, Ryberg et al.,1995, Ryberg et al., 1998, Vinnik and Ryaboy, 1981). The heterogeneity of the upper 100 km correlates well with heat flow measurements and the age of different tectonic units, with slower velocities associated with younger regions (Pavlenkova and Yegorkin, 1983). The observation of a teleseismic Pn phase followed by a long noisy coda has been iterpreted as evidence that the shallowest mantle consists of a zone of small

randomly distributed scatterers which serve as a waveguide (Ryberg et al., 1995). Their observations suggest that the zone extends to at most 100 km depth, below which there is a fundamental change in either the scale of the heterogeneity, or the value of seismic attenuation, Q. It is also notable that the depth, sharpness and magnitude of the transition zone discontinuties vary markedly from one model to the next (figure 10). This may reflect real differences in structure along the different profiles, or may be the result of the different methods used. Among the common features of these models is a distinct LVZ at around 200-300 km, similar to the depth range often found in shear wave studies of continental regimes. Unfortunately, due to the nature of the sources involved, there was no complimentary S wave data to use for comparison.

The purpose of this work is to develop a seismic inversion procedure to produce simultaneous P and S velocity models of the upper mantle and to apply that procedure to investigate the seismic structure of the upper mantle beneath cratons. The inversion was designed to match both timing and amplitude information of the body and surface wave arrivals in the data. Variables in the inversion include the five elastic constants that determine the seismic velocities in a radially anisotropic medium. Synthetic seismograms are compared to data to evaluate the fit of the models. Differential synthetic seismograms determine the influence of each model variable on the resulting synthetics. The full waveform from the start of the first body wave through the surface waves is used in the evaluation. All three components of the data (vertical, radial and tangential) are used in order to provide coincident information for the horizontally and vertically polarized components of α and β.

This dissertation is divided into 3 sections. In chapter 2 we present the inversion procedure that was developed as part of this work. The inversion combines the simulated annealing and conjugate-gradient techniques and is designed to optimize the match between synthetic seismograms and seismic data. In chapter 3, we discuss the effects of anisotropy on seismic waves, demonstrate how the neglect of anisotropy affects the results of isotropic studies and present strategies for identifying and modeling radial anisotropy in the Earth. Finally, In chapter 4, we present models for the seismic structure of the upper mantle beneath the East European platform including an analysis of radial anisotropy.

References

Agee, C. B., Petrology of the Mantle Transition zone, *Annu. Rev. Earth Planet. Sci.*, 21, 19-41, 1993

Anderson, D. L., Theory of the Earth, Blackwell Sci. Publ., 1989

Anderson, D. L. and Bass, J. D., Mineralogy and composition of the upper mantle, *Geophys. Res. Letts.*, 11, 7, 637-640, 1984

Anderson, D. L., Lithosphere, asthenosphere and perisphere, *Reviews of Geophysics*, 33, 1, 125-149, 1995

Artyushkov, E. V., On the origin of the seismic anisotropy of the lithosphere, *Geophys. J. R. astr. Soc.*, 76, 173-178, 1984

Bass, J. D. and Anderson, D. L., Composition of the upper mantle: geophysical tests of two petrological models, *Geophys. Res. Letts.*, 11, 3, 237-240, 1984

Duffy, T. S. and Anderson, D. L., Seismic velocities in mantle minerals and the mineralogy of the upper mantle, *J. Geophys. Res.*, 94, B2, 1895-1912, 1989

Ekstrom, G. and Dziewonski, A. M., The unique anisotropy of the Pacific upper mantle, *Nature*, 168-172, 1998

Estabrook, C. H. and Kind, R., The nature of the 660-kilometer upper mantle seismic discontinuity from precursors to the PP phase, *Science*, 274, 1179-1182, 1996

Forsyth, D. W., The early structural evolution and anisotropy of the oceanic upper mantle, *Geophys. J. R. astr. Soc.*, 43, 103-162, 1975

Gaherty, J. B., and Jordan, T. H., Lehmann discontinuity as the base of an anisotropic layer beneath continents, Science, 268, 1468-1471, 1995

Gaherty, J. B., Kato, M., and Jordan, T. H., Seismological structure of the upper mantle: a regional comparison of seismic layering, *Phys. Earth Planet. Inter.*, 110, 21-41, 1999.

Gaherty, J. B., Wang, Y. B., Jordan, T. H., and Weidner, D. J., Testing plausible upper-mantle compositions using fine-scale models of the 410-km discontinuity, *Geophys. Res. Letts.*, 26, 11, 1641-1644, 1999

Given, J. W. and Helmberger, D. V., Upper mantle structure of northwestern Eurasia, *J. Geophys. Res.*, 85, 7183-7194, 1980.

Grand, S. P. and Helmberger, D. V., Upper mantle shear structure of North America, *Geophys. J. R. Astron. Soc.*, 76, 399-438, 1984a.

Grand, S. P. and Helmberger, D. V., Upper mantle shear structure beneath the nortwest Atlantic ocean, *J. Geophys. Res.*, 89, 11,465-11,475, 1984b.

Ita, J. and Stixrude, L., Petrology, elasticity, and composition of the mantle transition zone, *J. Geophys. Res.*, 97, B5, 6849-6866, 1992

Jordan, T. H., The continental tectosphere, *Reviews of Geophysics*, 13, 1-12, 1975

Kern, H., P and S wave anisotropy and shear wave splitting at pressure and temperature in possible mantle rocks and their relationship to the rock fabric, *Phys. Earth Planet. Inter.*, 87, 245-256, 1993

Knoche, R., Webb, S. L. and Rubie, D. C., Measurements of acoustic wave velocities at P-T conditions of the Earth's mantle, Properties of Earth and Planetary Materials at High Pressure and Temperature, Geophysical Monograph 101, AGU, 119-128, 1998

Leeds, A. R., Lithospheric thickness in the western Pacific, *Phys. Earth Planet. Inter.*, 11, 61-64, 1975

LeFevre, L. V. and Helmberger, D. V., Upper mantle P velocity structure of the Canadian shield, *J. Geophys. Res.*, 94, 17749-17765, 1989.

Li, B., Liebermann, R. C. and Weidner, D. J., Elastic Moduli of Wadsleyite (β-Mg_2SiO_4) to 7 Gigapascals and 873 Kelvin, *Science*, 281, 675-677, 1998b

Li, B., Chen, G., Gwanmesia, G. D., and Liebermann, R. C., Sound velocity measurements at mantle transition zone conditions of pressure and temperature using ultrasonic interferometry in a multianvil apparatus, Properties of Earth and Planetary Materials at High Pressure and Temperature, Geophysical Monograph 101, AGU, 41-59, 1998c

Mechie, J., Egorkin, A. V., Fuchs, K., Ryberg, T., Solodilov, L. and Wenzel, F., P-wave mantle velocity structure beneath northern Eurasia from long-range recordings along the profile QUARTZ, *Phys. Earth Planet. Inter.*, 79, 269-286, 1993

Ming, L. C., Madon, M. and Wang, L.-J., Phase transitions in a komatiite-rock at high pressures and high temperatures, High Pressure Research: Application to Earth and Planetary Sciences, AGU, 245-255, 1992

Montagner, J-P., and Tanimoto, T., Global upper mantle tomography of seismic velocities and anisotropies, *J. Geophys. Res.*, 96, B12, 20,337-20,351, 1991.

Morozova, E. A., Morozov, I. B., Smithson, S. B. and Solodilov, L. N., Heterogeneity of the uppermost mantle beneath Russian Eurasia from the ultra-long-range profile QUARTZ, *J. Geophys. Res.*, 104, B9, 20,329-20,348, 1999.

Paulssen, H., Lateral heterogeneity of Europe's upper mantle as inferred from modelling of broad-band body waves, *Geophys. J. R. astr. Soc.*, 91, 171-199, 1987

Pavlenkova, N. I. and Yegorkin, A. V., Upper mantle heterogeneity in the northern par of Eurasia, *Phys. Earth Planet. Inter.*, 33, 180-193, 1983

Priestley, K., Velocity structure of the continental upper mantle: evidence from southern Africa, *Lithos*, 48, 45-56, 1999

Regan, J. and D. J. Anderson, Anisotropic models of the upper mantle, *Phys. Earth Planet. Inter.*, 35, 227-263, 1984

Ringwood, A. E., <u>Composition and petrology of the Earth's mantle</u>, McGraw-Hill Inc., 1975

Rodgers, A. and Bhattacharyya, J., Upper mantle shear and compressional velocity structure of the Central US Craton: Shear wave low-velocity zone and anisotropy, *Geophys. Res. Letts.*, 28, 2, 383-386, 2001

Ryberg, T., Fuchs, K., Egorkin, A. V. and Solodilov, L., Observation of high-frequency teleseismic Pn on the long-range Quartz profile across norther Eurasia, *J. Geophys. Res.*, 100, B9, 18,151-18,163, 1995

Ryberg, T., Wenzel, F., Egorkin, A. V. and Solodilov, L., Properties of the mantle transition zone in northern Eurasia, *J. Geophys. Res.*, 103, B1, 811-822, 1998

Silver, P. G., Seismic anisotropy beneath the continents: probing the depths of geology, *Annu. Rev. Earth Planet. Sci.* 24, 385-432, 1996.

Vinnik, L. P., Green, R. W. E., Nicolaysen, L. O., Kosarev, G. L., Petersen, N. V., Deep seismic structure of the Kaapvaal craton, *Tectonophysics*, 262, 67-75, 1996

Vinnik, L. P., Ryaboy, V. Z., Deep structure of the East European platform according to seismic data, *Phys Earth Planet. Inter.*, 25, 27-37, 1981

Walck, M. C., The P-wave upper mantle structure beneath an active spreading center - the Gulf of California, *Geophys. J. R. astr. Soc.*, 76, 697-723, 1984

Weidner, D., and Ito, E., Mineral physics constraints on a uniform mantle composition, <u>High Pressure Research in Mineral Physics</u>, 439-446, 1987

Xu, Y. B., and Wiens, D. A., Upper mantle structure of the southwest Pacific from regional waveform inversion, *J. Geophys. Res.*, 102, B12, 27,439-27,451, 1997

Zhao, L. S. and Helmberger, D. V., Upper mantle compressional velocity structure beneath the northwest Atlantic ocean, *J. Geophys. Res.*, 98, B8, 14,185-14,196, 1993

Chapter 2
Inversion Method

We have developed a procedure for the efficient inversion of seismic waveforms to produce structural models of the Earth's mantle. This technique is an iterative, nonlinear method combining the advantages of simulated annealing and least-squares gradient techniques (Sen and Stoffa, 1995; Tarantola, 1984; Mora, 1988). The variables in the problem are the seismic velocities (α and β) and the density (ρ) as a function of depth. When transverse isotropy is required, this set is expanded to include the five variables that determine the seismic velocities in a transversely isotropic medium (α_h, α_v, β_h, β_v, η).

Several factors complicate the inversion of seismic data: The equations involved are non-linear, the size of the problem is large, and the solutions obtained are not unique. Addressing the non-linearity and uniqueness problems requires extracting as much information as possible from the data and also requires using information known independently of the data to place physically realistic bounds on the solution. Tarantola (1984) has shown that using the entire seismogram, including amplitude and timing information, increases the stability of the problem and dramatically reduces the uncertainty of the solution. In this study, we use the full waveform, from the start of the first body wave through the surface waves, in the evaluation. This takes advantage of converted, multiply reflected and transmitted arrivals that are often discarded or treated as noise. All 3 components of the data (vertical, radial and tangential) are used in order to provide coincident information for the horizontally and vertically polarized components of α and β.

To take advantage of the information in the full waveform, a method for calculating complete and accurate synthetic seismograms is required. In this study, synthetic waveforms for isotropic and transversely isotropic models were created using the reflectivity technique (Fuchs and Muller, 1971; Randall, 1994). This method provides synthetic seismograms for 1-dimensional Earth models with accurate frequency, timing and amplitude characteristics of all phases, including the surface waves, which can be compared directly to the recorded data. Radially anisotropic structures were created using the fine-layered equivalency equations of Backus (1962). The details of the equivalence are given in appendix A.

The size of the problem makes computation time a fundamental constraint on any seismic inversion procedure. To be useful, the inversion must be both accurate and efficient. The number of variables involved, the time required to calculate each iteration and the number of iterations required control the efficiency of the method. To address this problem we invert our data in several steps over a number of frequency windows. Frequency window techniques have been used successfully to obtain crustal models from seismic reflection data (Pica et al., 1990) and to obtain models of the upper mantle (Xu and Wiens, 1997). The procedure begins by filtering the data over a narrow band focused on low frequencies, inverting to get an initial model, then increasing the bandwidth and inverting again using the previous result as a starting model (figure 11). This process is repeated until the full bandwidth is used.

Frequency window techniques have two notable advantages for this study. The first is that the sensitivity of seismic data to the Earth's structure changes depending on the frequency band that is observed. The lower frequency portions of the data are most sensitive to the long-wavelength variations in velocity, while high frequency bands are most sensitive to sharp contrasts at layer interfaces. The low frequency result is therefore a good low-resolution model and the higher frequency steps can be regarded as more finely detailed perturbations of that model. The second advantage is that the speed of the reflectivity method is directly related to the range of frequencies used, so the initial narrow-band steps proceed relatively quickly.

In addition to using frequency windows, we also employ time windows in our inversion scheme. Time windows are the portions of each seismogram that the inversion tries to duplicate with synthetics. In the first steps, we select the entire seismogram from the first body wave arrival through the surface wave and the inversion attempts to match the entire waveform. At later steps, the time window is reduced to include less of the surface wave arrivals until finally only the body wave arrivals remain (figure 12). This procedure results in a top-down solution for the Earth model, fitting the data most sensitive to shallow structure first and progressively solving for deeper structure, and it prevents the larger surface wave arrivals from dominating the final inversion result.

Seismic inversion methods often involve minimizing a function that describes the misfit between the observed data and model synthetics. Various methods have been

Frequency Windows
Tangential Component Data (45.0°)
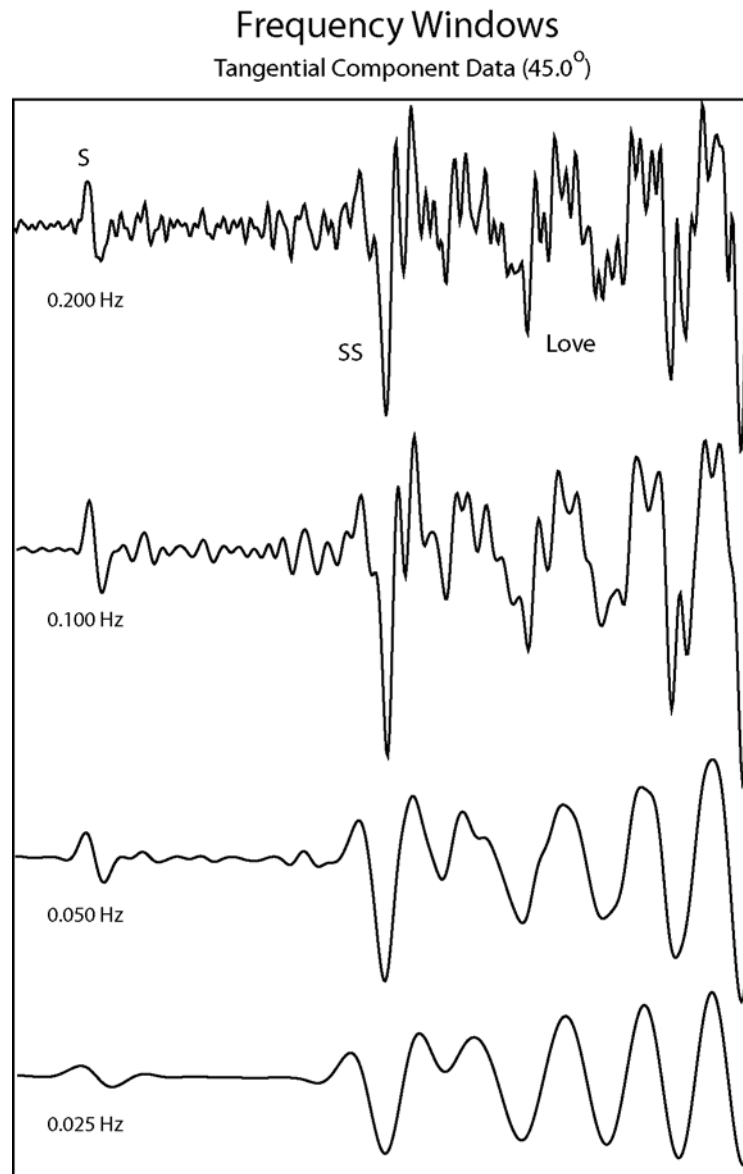
Figure 11. An example of the frequency windows used in the East European platform study is shown. The data are low-pass filtered with high corner frequencies at 25, 50, 100 and 200 mHz. Each of the four traces shown is the same seismogram filtered to varying degrees. The data are from a Russian shield path at a source-receiver offset of 45°.

Time Windows
Tangential Component Data (45.0°)
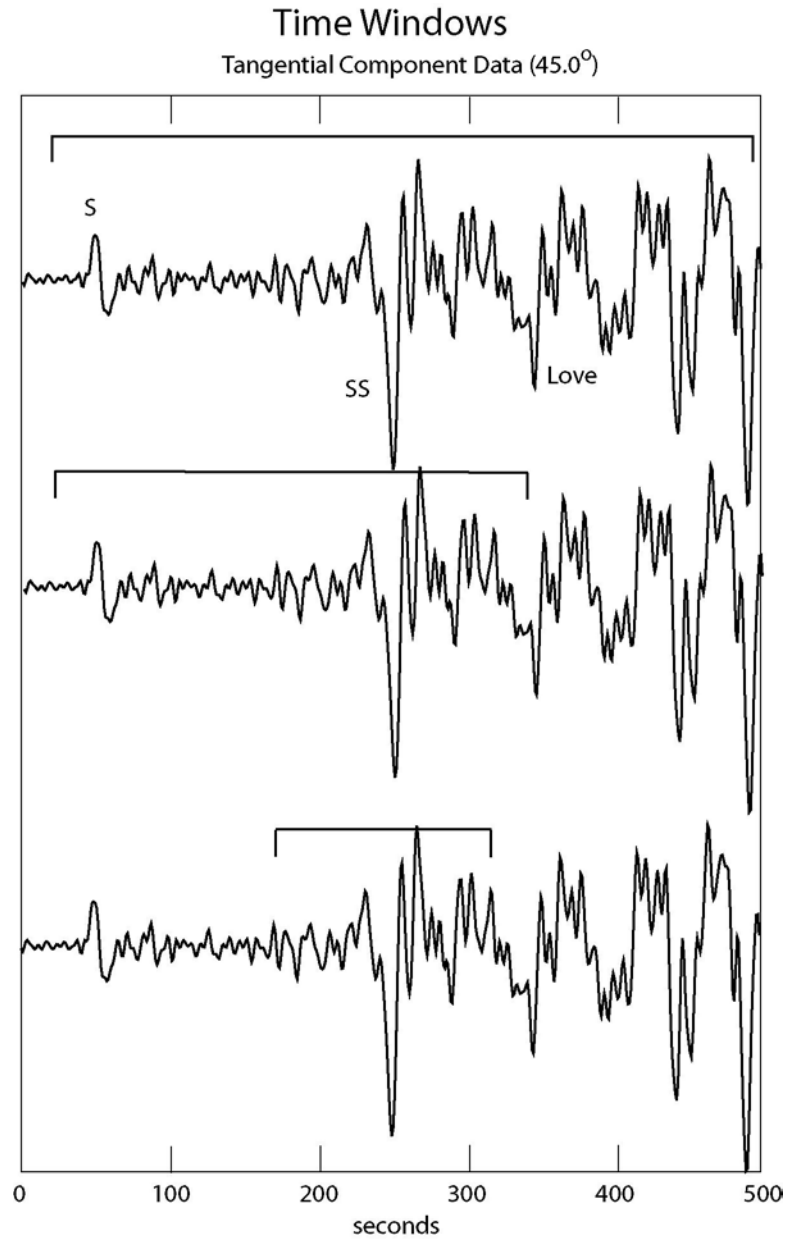
Figure 12. An example of time windows used in the inversion procedure. The traces are the tangential component data at 45°. The first arrival is the direct S phase. The black lines indicate the portion of the data that was inverted in 3 different runs. In the first run the entire seismogram was inverted, beginning with the direct S arrival through the surface wave arrivals (top). Inclusion of the surface waves provides good resolution of the shallowest structure. Subsequent runs were inverted starting from the that result, but focusing on narrower portions of the data and solving for finer scale structure at depth (middle, bottom)

developed to optimize the problem. Random walk methods are good at finding the global minimum, but require a prohibitive number of iterations to converge when a high resolution model is desired. Gradient methods achieve rapid convergence by calculating the best 'next step' in the inversion, but can get trapped in a local minimum. We have combined the advantages of these methods to achieve quick convergence to the global best-fit model.

The inversion employs a normalized cross-correlation misfit function (S). Data are directly compared to synthetics to establish a match. The initial data vectors (d_0) are the seismic waveforms recorded at each station. Synthetic seismograms make up the other data vectors (d_n). The cross correlation is performed over the time window specified at the start of the inversion. The fit of the model is established by the cross-correlation between the data and synthetics normalized by their autocorrelations.

$$xc = correlation(d_0, d_n)$$
$$ac = correlation(d_0, d_0)$$
$$sc = correlation(d_n, d_n)$$
$$S = 1 - (xc / \sqrt{(ac*sc)})$$

The specific procedures we use are the very fast simulated annealing (VFSA) method (Sen and Stoffa, 1995) and the conjugate-gradient (CG) method (Mora, 1988). These are discussed in more detail below.

The Very Fast Simulated Annealing Inversion Method (VFSA)

VFSA is a random walk procedure that has been optimized to speed convergence (Sen and Stoffa, 1995). The optimization is accomplished using a probability function (T) that governs both the step size and the acceptance criteria. T is referred to as the 'temperature' function due to the heat-bath analogy used in developing VFSA. After each iteration, the variables in the model are perturbed relative to the 'best fit' model. The step size is the change in each model variable from one iteration to the next. At high temperatures the average step size is large and the probability is high that the new model will be accepted as the 'best fit'. This allows the inversion to climb out of local minima and search throughout

model space, which enhances the likelihood that the global minimum will be found. After each iteration, the temperature is lowered and the inversion continues with more restrictive criteria. Given a sufficient number of iterations, the inversion will converge on a global best fit model.

The cooling schedule is:

$T_k = T_o *(-c^k)$

T_o is the initial temperature

T_k is the temperature at the kth iteration

c is a temperature control variable

The procedure starts at a random point in model space (m_o) and the misfit function (S_o) for this model is calculated. At each iteration a new model (m_{new}) is created by taking random steps relative to this initial model until a new 'best fit' model is found.

$m_{new} = m_o + y (m_{max} - m_{min})$

$m_{min} \leq m_{new} \leq m_{max}$

m_{max}, m_{min} are the minimum and maximum allowable values for each parameter

y is a random number between ± 1 based on the value of T and generated individually for each parameter:

$y = sgn(u - 0.5) T [(1 + T^{-1})^{|2u - 1|} - 1]$

u is a random number between 0 and 1

The function y(u) can be thought of as a probability function, with increased y representing larger step sizes from one model step to the next. As the temperature decreases, y(u) collapses and the likelihood that large steps will be taken is reduced. A plot of the function y(u) is shown in figure 13. Figure 14 shows how the collapse in y(u) affects the perturbation to a model between one step and the next. At high temperature (figure 14a) the model varies

dramatically from one step to the next. At low temperature (figure 14b) the models are very similar.

The misfit function is recalculated for each new model. The new model is accepted or rejected as an update for m_o based on the acceptance criteria. If the misfit is smaller than S_o the model is automatically accepted. VFSA also allows the possibility for poorer fits to be accepted, which allows the inversion to climb out of local minima and seek a global solution. The acceptance criteria are as follows:

$$\Delta S = S_o - S_{new}, \text{ the difference in misfit functions}$$

if $\Delta S < 0$ then m_{new} is accepted as the new m_o, otherwise,

$$P = \exp(\Delta S / T)$$

A random number, r, between 0 and 1 is selected and if $P > r$ then m_{new} is accepted.

Synthetic test case

We ran a number of synthetic cases to test the ability of the VFSA method to resolve mantle structure. Figure 15 illustrates the results of one of these tests for a model of the transition zone. Synthetic data were created for an isotropic S_H velocity model (thick solid line) and used as the data in an inversion test. A significantly different S_H model was used as a starting point in the inversion (dotted line). The geometry of the tests were designed to match that of the RISTRA PASSCAL experiment (Gao et al., 2001): 51 stations along a line with an average spacing of 20 km between stations. The source was selected to match a June 2, 2000 event recorded along the line, such that source-receiver offsets ranged between 1828 and 2678 km. The inversion was run for 400 iterations with a high corner cutoff frequency of 0.08 Hz, then continued for another 400 iterations with the high frequency cutoff increased to 0.25 Hz. In the first pass the data were inverted for 17 layers between 325 and 660 km. In the second pass, the time window over which the data were inverted was collapsed to focus on arrivals passing through the transition zone and solved for 13 layers between 414 and 660

31
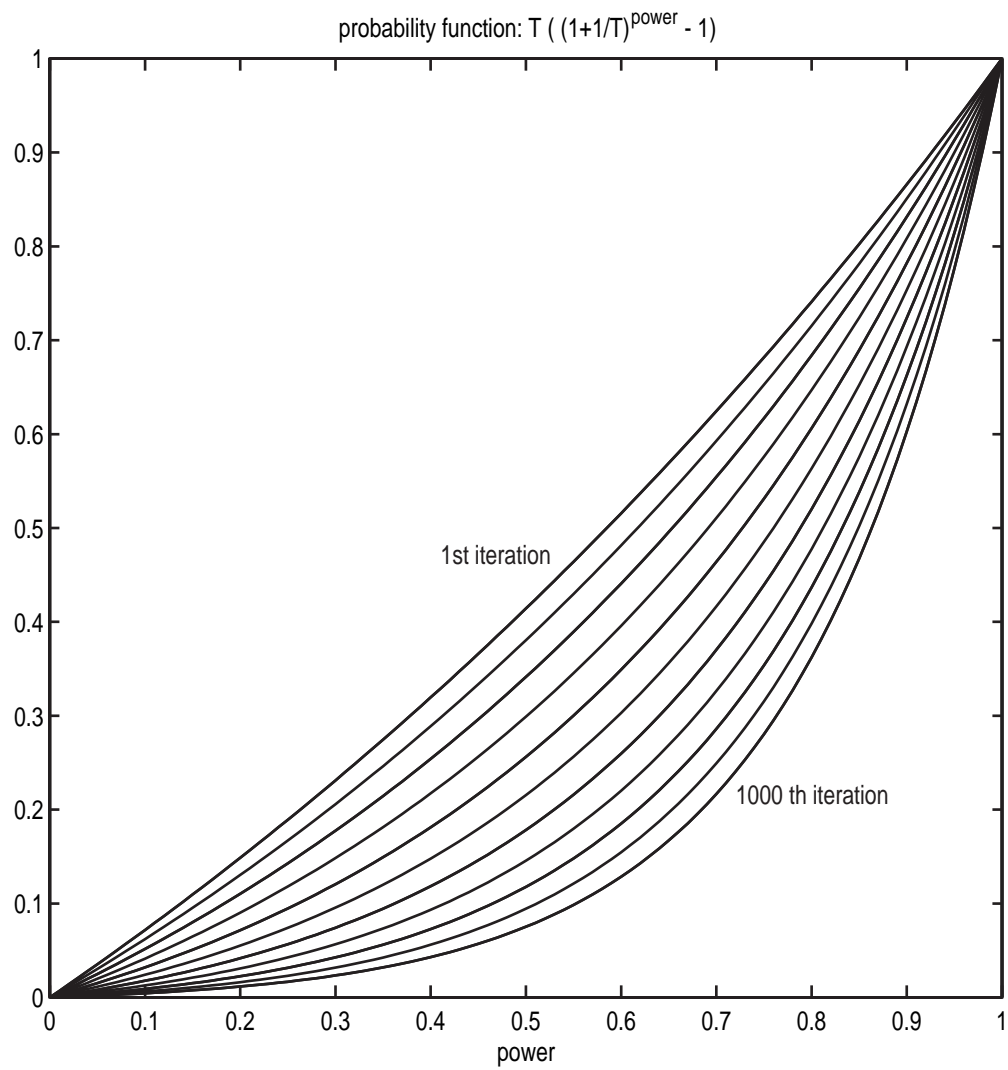
Figure 13. The probability function y(u). In this example the temperature variable T begins at a value of 1 and decreases with each iteration as $T_k = 0.995^k$. y(u) is plotted for every 100th iteration.
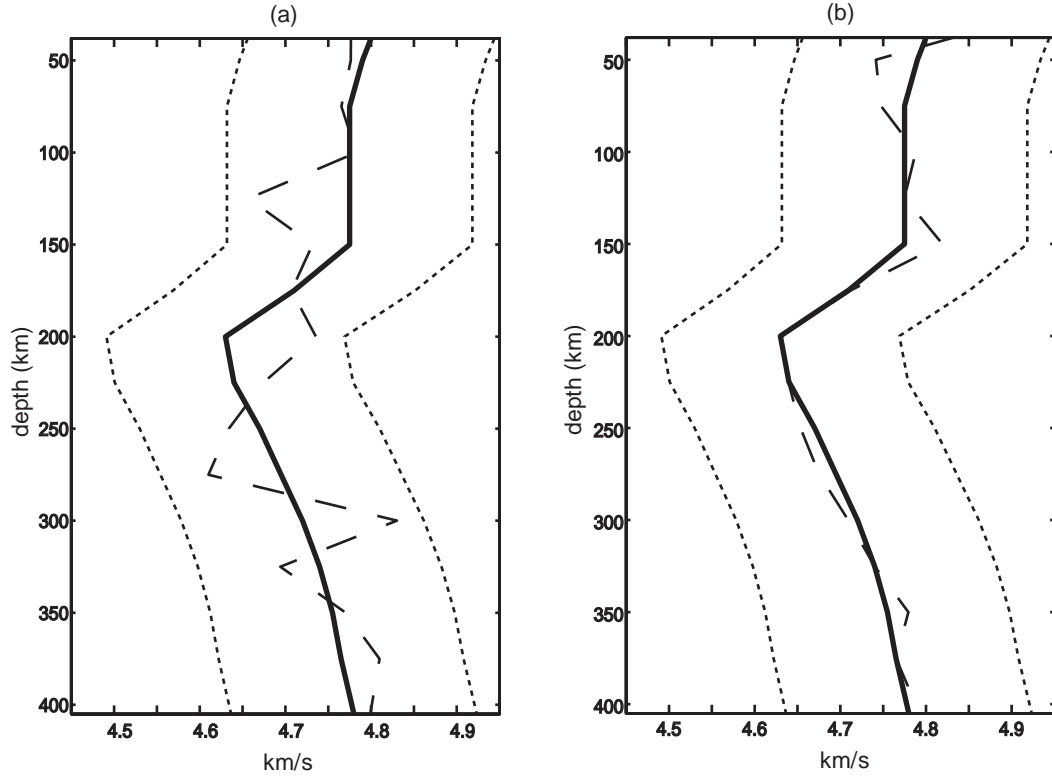
Figure 14. An example of how the temperature controls the step size. Reference model – SNA (bold line) is used as the starting model and perturbed by the equation ($m_{new} = m_o + y$ ($m_{max} - m_{min}$)). The model perturbation for each case is shown as a dashed line. The high and low limit boundaries are shown as dotted lines.

(a) Temperature = 0.03

(b) Temperature = $0.03 * 0.995^{1000}$ (value after 1000 iterations starting at T = 0.03)

VFSA Inversion Test Models
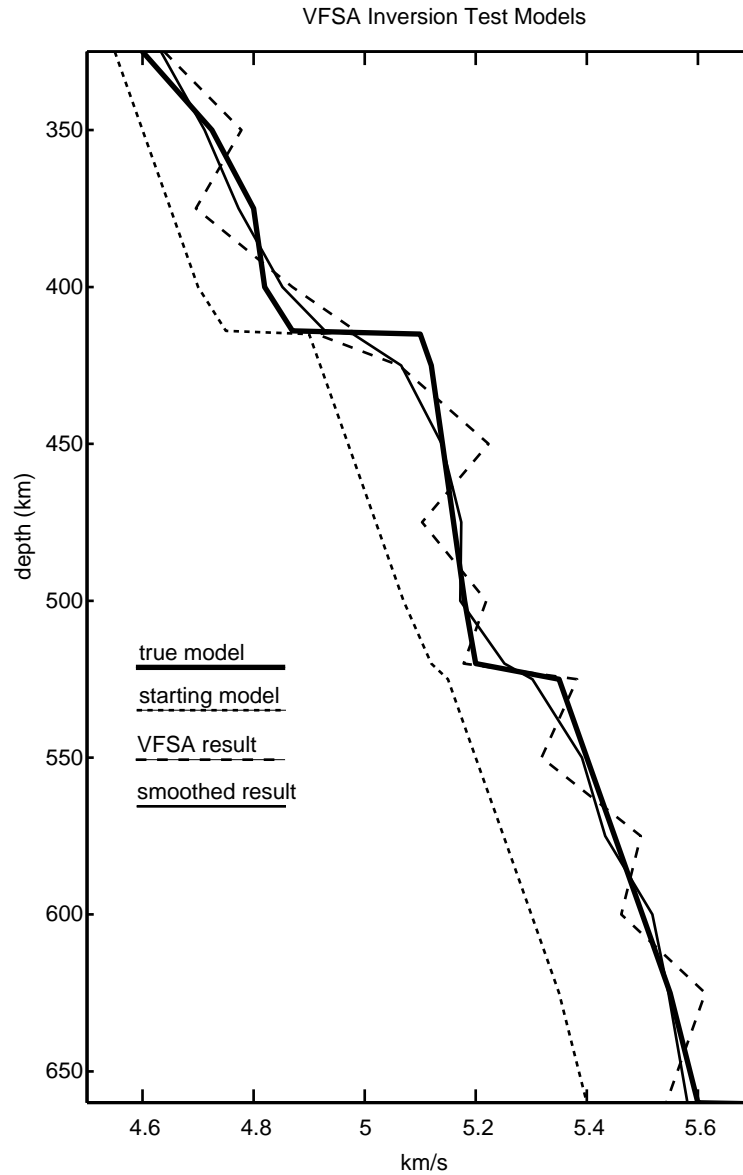
Figure 15. A test of the VFSA inversion procedure. Synthetic seismograms were created for an isotropic S_H velocity model (thick solid line) and used as the data in an inversion test. The inversion was begun using a simple starting model (dotted line) and inverted in two passes of 400 iterations each; first with a high corner frequency cutoff of 0.08 Hz and then with a high corner frequency cutoff of 0.25 Hz. The final, unsmoothed result (dashed line) is much more heterogeneous than the true model, however when smoothed with a simple triangle function the match improves (thin solid line).
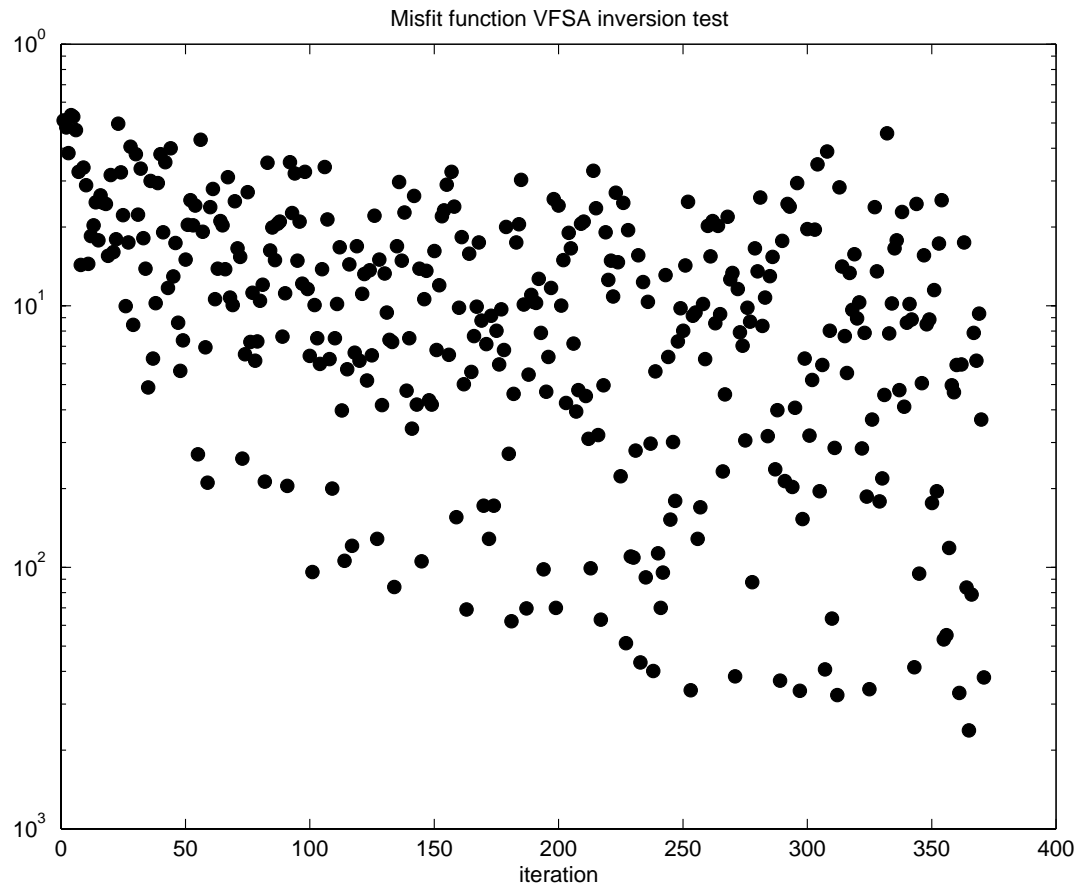
Figure 16. The evolution of the misfit function for the first pass of the synthetic test case described in figure 15. Note that the scatter from one iteration to the next is large, but the minimum value drops off exponentially over time.

Inversion Test Synthetics
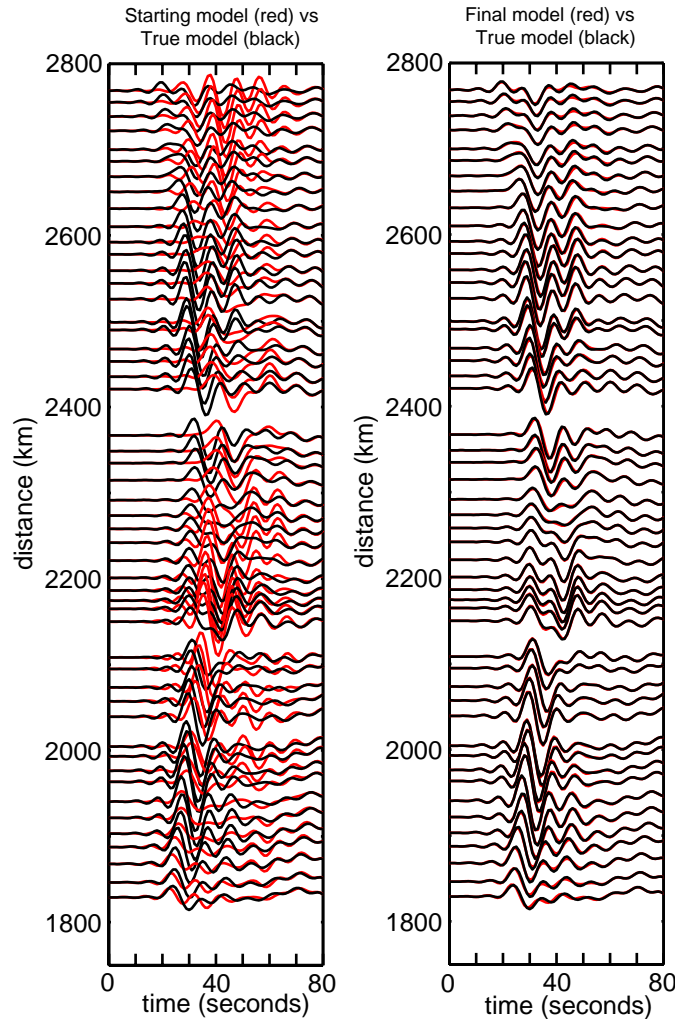
Figure 17. Tangential component data and synthetics used in the inversion test described in figure 15. On the left data are compared to the starting model synthetics. On the right the final model synthetics are compared to the data.

km. The final result (dashed line) is very close to the correct model, but shows more heterogeneity. When the final result is convolved with a simple triangle function (thin solid line) the anomalous heterogeneity disappears. Figure 16 shows the misfit function at each iteration for the first pass. Note that the minimum value drops exponentially, but that the scatter is large. The inversion spends most of its time testing very poor models, even after a very good solution has been found.

The data and synthetics for the initial and final models are compared in figure 17. This test case represents an ideal, because both the data and synthetics were created using the same reflectivity code and there was no noise included. The inversion could conceivably match the data exactly if run long enough.

The Conjugate Gradient Inversion Method (CG)

Conjugate gradient inversion (CG) is a local descent method that is very effective in large nonlinear inverse problems (Mora, 1988; Tarantola, 1984). Gradient methods work by establishing the best 'next step' for the inversion. This is determined by calculating differentials of the misfit function for each model parameter and combining them to establish the vector in model space that points to the smallest value of the misfit function (S). This is the steepest descent direction. Conjugate directions are combinations of the current and previous steepest descent directions and help to speed convergence in subsequent iterations.

The nonlinear conjugate-gradient inversion method will converge to the best fit solution as long as the starting model is within the valley of the global minimum (Gauthier et al. 1986). Otherwise the model will either converge to a local minimum, or convergence will be slow. Unlike the VFSA method, the inversion cannot start at a random point in model space. Typically this means that the very long wavelengths of the model parameters must be present in the initial model (Pica et. al., 1990). To address this problem, we begin by inverting the low frequency structure first using the VFSA method and use this as the initial model for the CG technique.

The model update is established by differentials between the data and the synthetic seismograms (produced by subtracting the data from the synthetic result). The variables in the equations are defined below, adopting the method and notation from Mora (1988):

d_0 : The seismic waveform data

d_n : The synthetic seismograms = $d(m_n)$

m_n : The models at various iterations (n)

C_d : Data covariance matrix

C_m : Model covariance matrix

$\Delta d_n = d_n - d_0$

$\Delta m_n = m_n - m_{n-1}$

The gradient will be calculated using differential seismograms (D) that represent the sensitivity of the seismogram to individual parameters in the model.

$D = \partial d / \partial m$ is a matrix of differential seismograms.

The gradient vector (g) is defined to be ½ the direction of steepest descent:

$$g_n = 0.5 \, \partial S / \partial m = D^T \, C_d^{-1} \, \Delta d_n + C_m^{-1} \, \Delta m_n$$

The preconditioned gradient, p, is

$$p_n \sim C_m \, g_n$$

n is the current step in the iteration

The conjugate direction is found using the Polak-Ribiere method:

$$c_n = p_n + c_{n-1} \, (p_n{}^* \, (g_n - g_{n-1}))/(p_{n-1}{}^* \, g_{n-1})$$

and the step length η is:

$$\eta_n = c_n{}^* \, g_n \, /(\, c_n{}^* \, D_n{}^* \, C_d^{-1} \, D_n \, c_n + c_n{}^* \, C_m^{-1} \, c_n)$$

the model update is:

$$m_{n+1} = m_n - \eta_n c_n$$

Synthetic seismograms are recalculated based on this model and the misfit function is recalculated. This procedure is repeated until the inversion converges.

We use a diagonal data covariance matrix, C_d, indicating that the inversion assumes the data are independent and all noise in the data is uncorrelated. The values within C_d are weighted so that the inversion focuses on the portions of the data most sensitive to the structure we are modeling. We typically use a diagonal model covariance matrix, C_m, as well (model parameters are independent), however C_m can also be used to define strict jumps at seismic discontinuities or to ensure that the velocity from one layer to the next varies by only a small amount.

Differential Synthetic Seismograms

The CG routine uses differential synthetic seismograms to guide the search through model space. A differential synthetic is a measure of how a small perturbation in a model affects the resulting synthetic seismogram. The simplest way to calculate the differentials is to create synthetics for an initial model, create synthetics for a small perturbation to that model and subtract one result from the other, although other numerical methods have been developed as well (Randall, 1994; Zeng and Anderson, 1995). Typically, a separate differential is created for each variable in the inversion. Differential synthetics are very powerful, because they allow the code to determine where the energy on the seismogram comes from, aid in the identification of specific arrivals and allow the inversion to focus in on those that are poorly fit by the current model. An example of differential synthetics is illustrated in figure 18. The top trace is a full synthetic seismogram for the starting model with major phases identified. The remaining traces are differentials produced by subtracting synthetics of perturbed models from the original synthetic. In each case the velocity of a single layer has been slightly changed from the original model. The main computational cost

Differential Synthetic Seismograms
2768 km
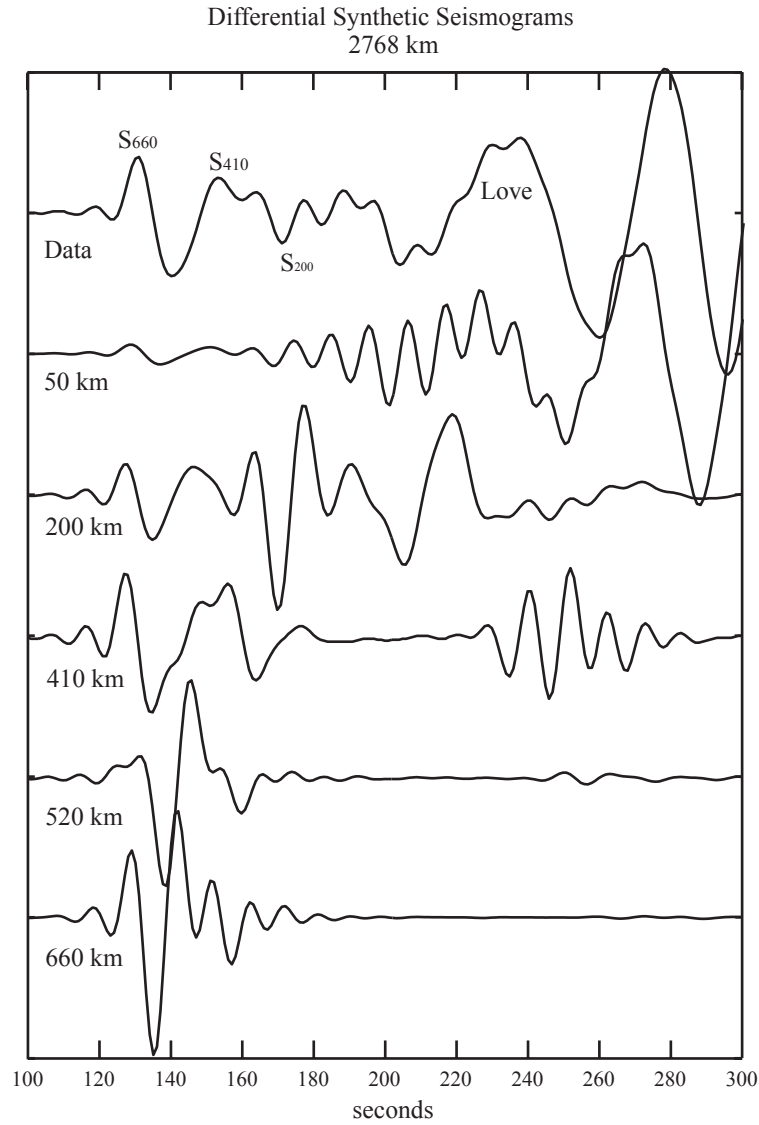
Figure 18. An example of the use of differential synthetic seismograms. The reference model is the one described in figure 15. The top trace is a full synthetic seismogram at 2768 km source-receiver distance with major phases identified. The remaining traces are differentials produced by subtracting synthetics of perturbed models from the original synthetic (the scales are normalized for the figure). In each case the S velocity of a single layer has been slightly perturbed (0.1 %) from the original model. The layers were located at 50, 200, 410, 520 and 660 km depth, respectively.

of the CG method is the calculation of the differential synthetics. Differential seismograms have been used to model crustal and mantle structure (Xu and Wiens, 1997; Swenson et al., 1999; Rodgers et al., 1999) and to invert seismic source parameters (Ghose et al., 1998).

Frequency Windowing

The sensitivity of seismic data to the Earth's structure changes depending on the frequency band that is observed. The very low frequency portions of the data are most sensitive to the long wavelength variations of the Earth parameters, while high frequency bands are most sensitive to sharp contrasts at layer interfaces. The broadband seismic data used in this study can be filtered at different frequency bands to focus on different scales of heterogeneity. We take advantage of this to improve the model solution by using a frequency windowing technique.

The frequency windowing technique takes several steps, starting with a narrow frequency range and progressively increasing the bandwidth until the full signal is used. In the first step, the data are low-pass filtered and inverted for the large scale radial structure of the model. Since the low frequency data can be inverted using large step sizes and thick model layers, the number of variables required is reduced, dramatically increasing the rate of convergence. The solution at each step will be used as an a priori model for the following step.

Frequency window techniques using the CG method have been used successfully to obtain crustal models from seismic reflection data (Pica et. al., 1990) and to obtain models of the upper mantle from regional data (Xu and Wiens, 1997).

Synthetic test case

We used synthetic data sets to test the CG method in the same way that we tested the VFSA method. Figure 19 shows the results of the transition zone test case that was described above. The inversion was run for 20 iterations with a high corner cutoff frequency of 0.08 Hz, then continued for another 20 iterations with the high frequency cutoff increased to 0.25 Hz. In the first pass the data were inverted for 7 layers (5 layers from 325 to 414, and a simple gradient between 415 and 660 km). Note the difference between this first pass and that taken
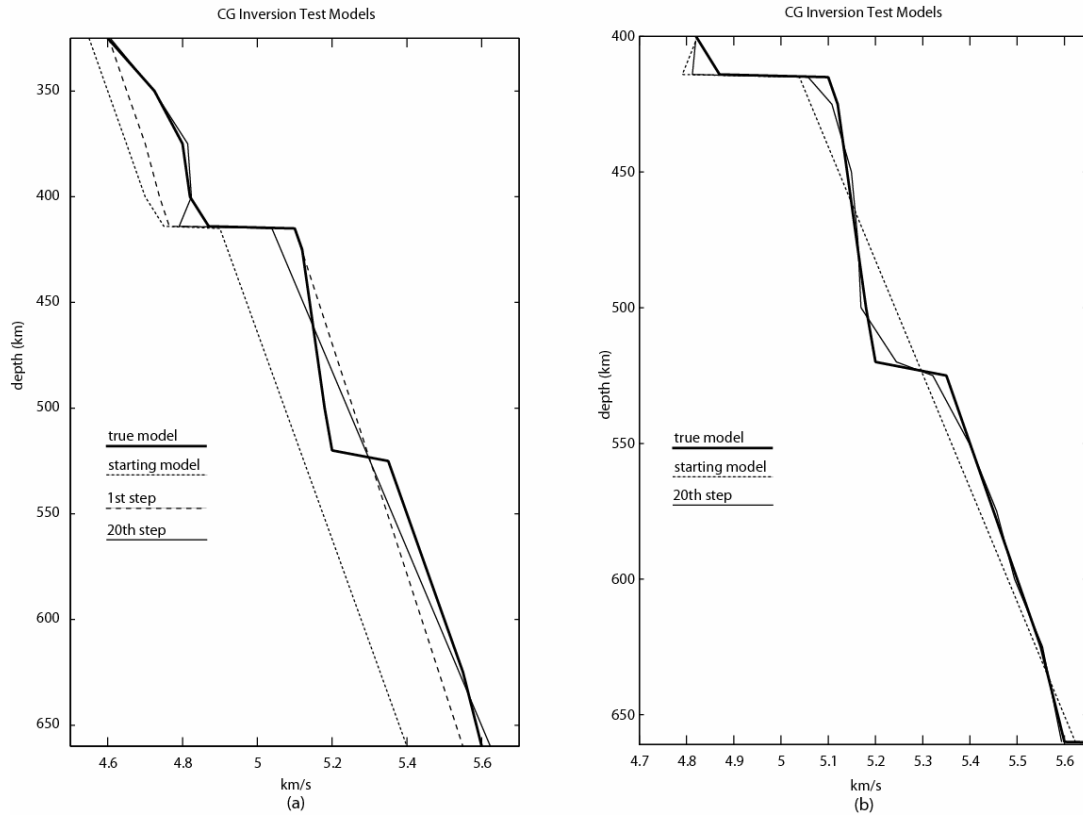
Figure 19. A test of the CG inversion procedure. Synthetic seismograms were created for the isotropic S_H velocity model discussed in figure 15 (thick solid line) and used as the data in the inversion test. The inversion was begun using a simple starting model (dotted line) and inverted in two passes of 20 iterations each. The 20th step result in each case is marked by the thin solid line.

(a) first pass: high corner frequency cutoff of 0.08 Hz. 7 layers total (5 layers from 325 to 414, and a simple gradient between 415 and 660 km).

(b) second pass: high corner frequency cutoff increased to 0.25 Hz. 13 layers between 414 and 660 km.
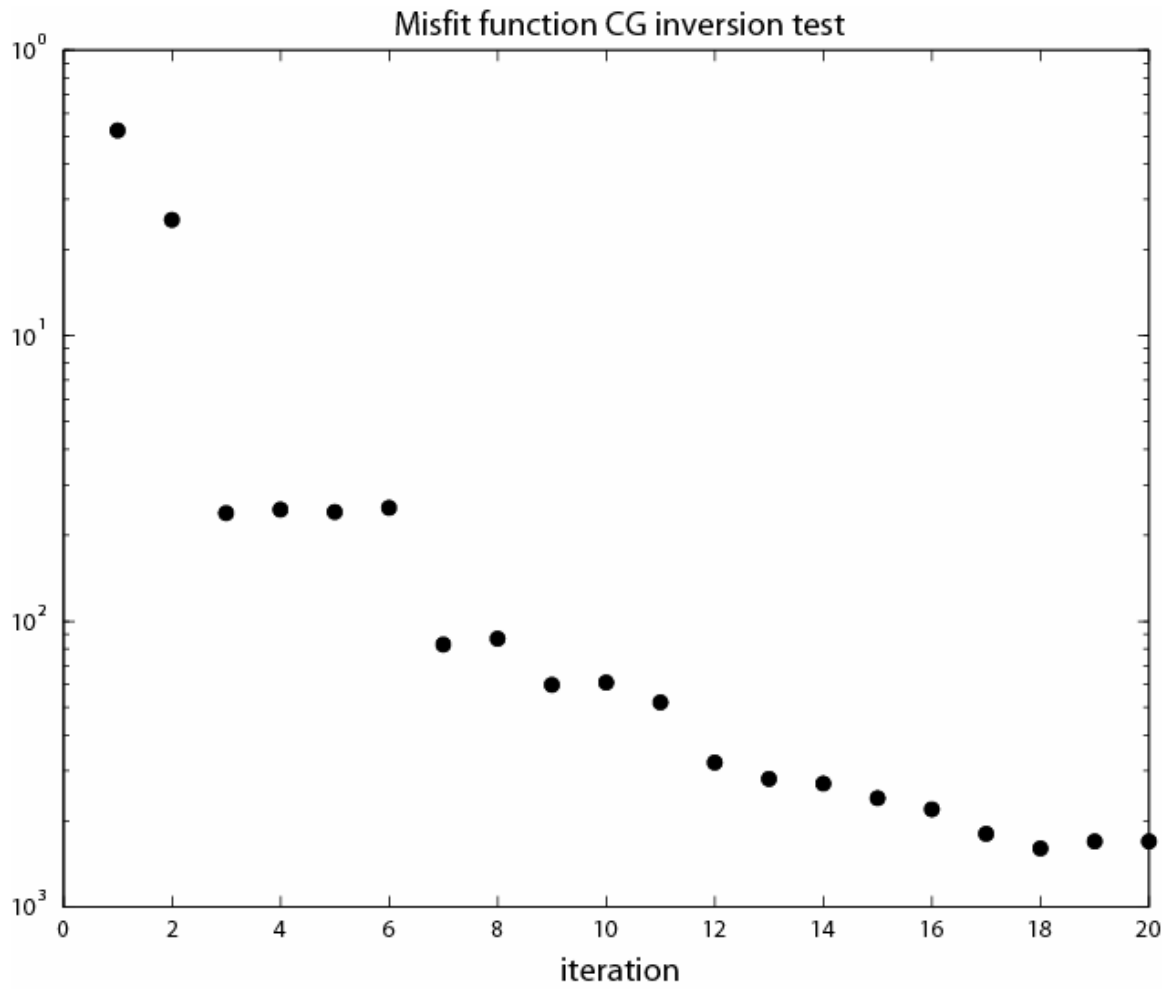
Figure 20. The evolution of the misfit function for the first pass of the synthetic test case described in figure 19.

in the VFSA test. The CG inversion focuses on the shallower portion of the model initially, because errors in these layers dominate the misfit function. Attempting to solve for finer scale structure in the transition zone at this point will only force the code to calculate additional differentials, significantly slowing the procedure, without any corresponding improvement in convergence. VFSA doesn't share the same cost in calculating additional layers. The CG first pass results are shown in figure 19a. Note the considerable improvement in the model after the first iteration. This first step often results in a large improvement in the fit of the model, because CG rapidly corrects for any discrepancies in the mean travel time of the seismic phases. In the second pass, the time window over which the data were inverted was collapsed to focus on arrivals passing through the transition zone and solved for 13 layers between 414 and 660 km. Note the match between the final model (thin solid line) and the true model (thick solid line) including the location of the 520 km discontinuity. Figure 20 shows the misfit function at each iteration for the first pass of the CG test. The exponential dropoff is a characteristic of this inversion procedure.

Again, this synthetic test is an ideal case. Inversion of real data typically involves more passes for convergence on a best fit model.

Identification of discontinuities and collapse into local minima

Preliminary results from an inversion of a data set for the deep mantle illustrate some of the key advantages and disadvantages to the use of the CG method. The data are 46 tangential component seismograms in the $70^o – 79^o$ range obtained from the RISTRA array. The inversion is focused on the time window containing the direct S and core reflected ScS arrival as well as phases which appear in between the two (figure 21). These data are highly sensitive to the structure of the bottom several hundred kilometers of the mantle beneath Central America. Figure 22 presents the initial steps of the CG inversion of the data set. The starting model is AK135 (Kennett et al., 1995). Note that the inversion immediately identifies a discontinuity at ~2650 km. This corresponds to the location of the Lay discontinuity, which is widely observed and generally regarded as identifying the top of the D" layer at the base of the mantle (Lay and Helmberger, 1983). This example demonstrates one of the strengths of the CG inversion method: it is very good at rapidly identifying discontinuities and gradients in the Earth.
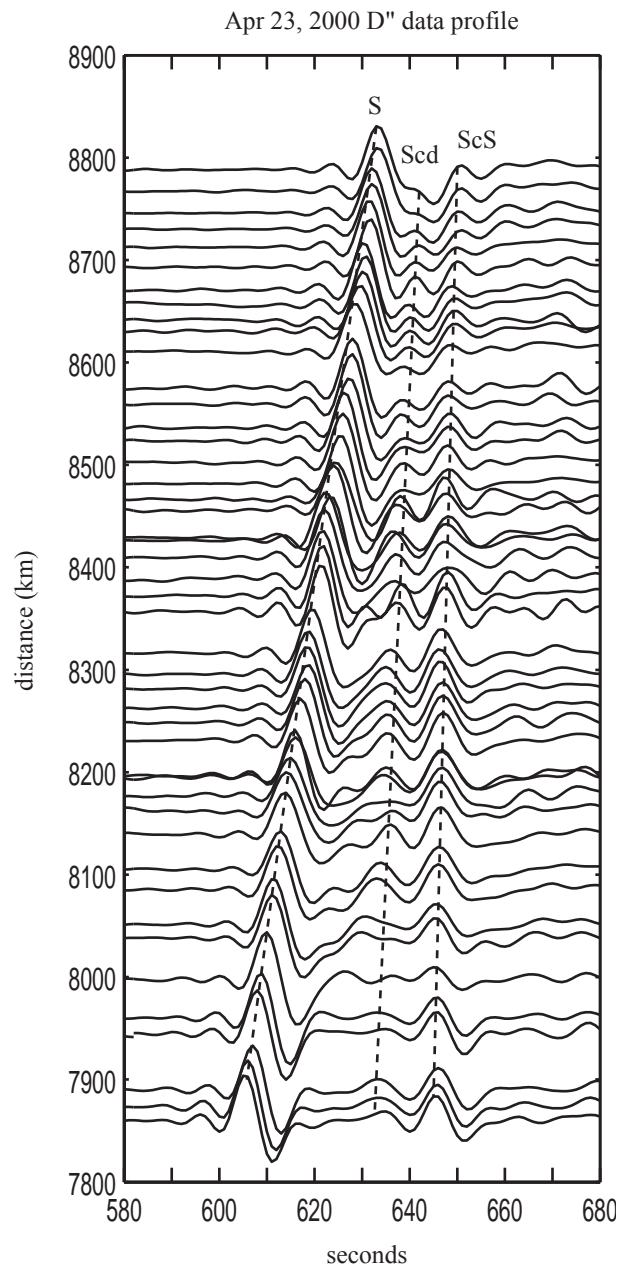
Figure 21. A profile of data from the RISTRA array used to invert structure of the deep mantle. Direct and reflected phases are identified. The Scd arrival is thought to be caused by a discontinuity near 2650 km depth (the Lay discontinuity).
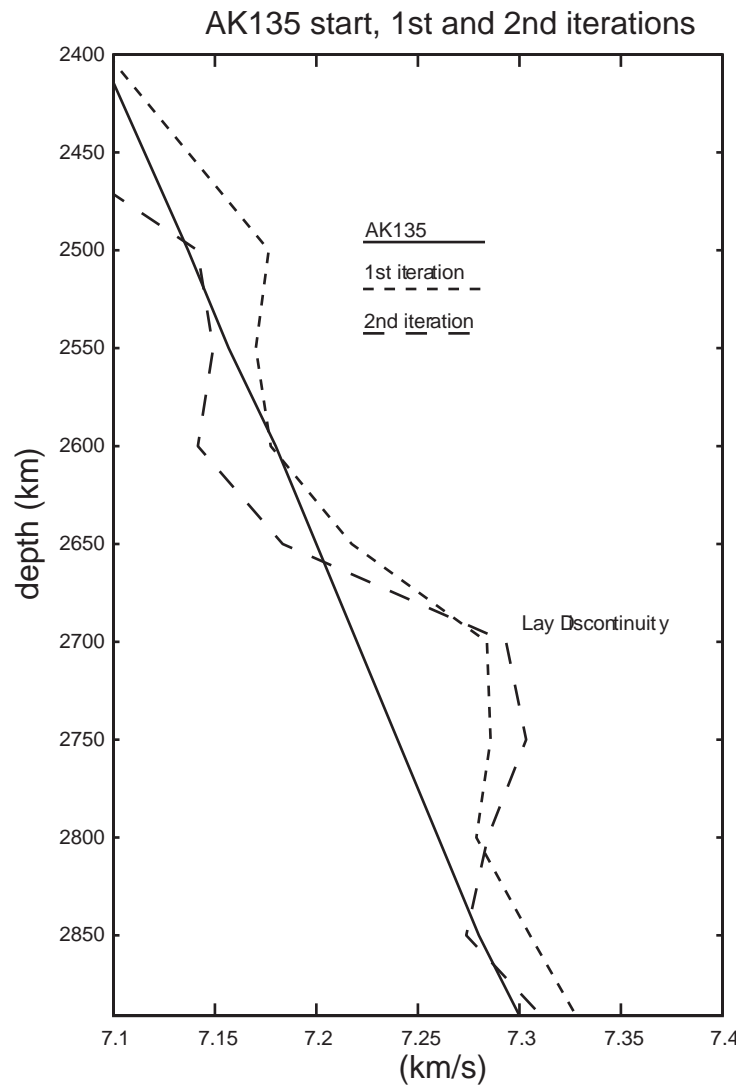
Figure 22. Initial step results for data from the RISTRA array sampling the bottom of the mantle. The AK135 reference Earth model (Kennett et al., 1995) is used as the initial model (solid line). The 1st and 2nd CG iteration results (dashed) are plotted.
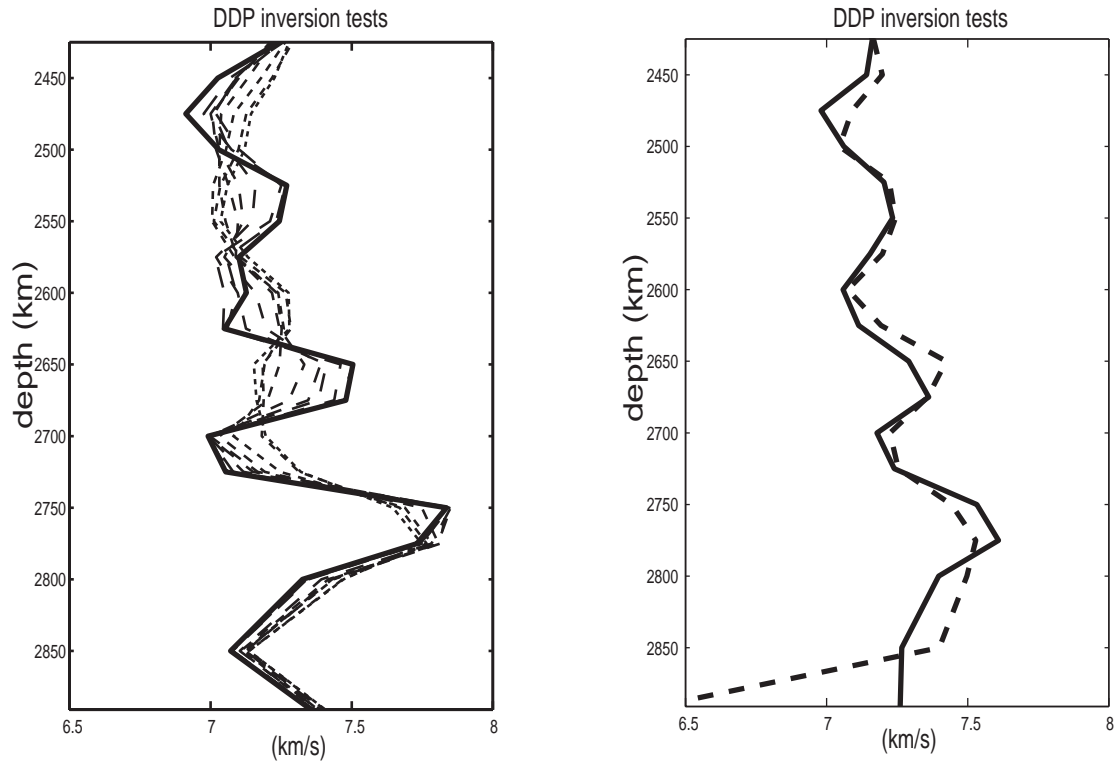
Figure 23. Continuation of the inversion in figure 22.

(a) illustrates the identification of discontinuities and collapse into a local minimum. The result after every 2nd iteration is plotted (dashed) converging on the final result (solid).

(b) The CG result of figure 23a smoothed using a simple, three point triangle function [0.2, 0.6, 0.2] (solid) is compared to the VFSA result (dashed) obtained independently.

Figure 23 shows the result after a series of passes alternating between the CG and VFSA method. At this stage the inversion has identified several discontinuities between 2500 and 2891 km depth. In the CG step shown, the inversion has gotten trapped in a local minimum. Large increases in the size of the discontinuities are compensated by equivalent decreases in the layers directly below. This preserves relative times of the seismic arrivals by preserving the mean velocity through the structure. Allowed to continue the inversion will create a series of layers with large vertical heterogeneity that is not strictly required by the data set. This illustrates one of the disadvantages of the CG method: it may concentrate all its effort on a few variables that dominate the seismic energy, focusing heterogeneity into specific layers. These anomalies can be checked by smoothing the result. In figure 23b, the final CG result (solid line) is convolved with a simple triangle function (dashed line), which removes the large anomalies, but preserves the mean travel time through the structure. The misfit function for both models is nearly identical. Finally, we compare the smoothed CG result (solid line) with the result of a VFSA inversion (dashed line). Note that the major structures including depth and amplitudes of the discontinuities are seen in both models.

Combining the methods

The VFSA and CG inversion methods use very different strategies to obtain a final solution. VFSA searches model space for the best fitting model and slowly collapses the model space around the better fits. CG works by identifying phases and focusing on only those model parameters that affect the arrivals of interest. VFSA will typically return a more heterogeneous structure than is required to fit the data, while CG will return the simplest perturbation to the starting model. CG is particularly useful when phases are simple and readily identifiable, while VFSA becomes more useful when the data are very complicated. For simple data (particularly synthetic data) either method is quite capable of obtaining a good solution. However, because of the large number of unknowns involved, several inversion passes are usually required for each frequency window when inverting real data. Our objective is to combine the two methods to optimize the inversion. Each method has significant advantages and disadvantages relative to the other. These tend to be complimentary: the strengths of one method are generally the weaknesses of the other. The

major strengths of the CG method are its speed and its ability to identify and focus in on the most important model variables. Once it is able to accurately identify the individual phases in a seismogram it proceeds rapidly to a final solution. The first step in a CG inversion typically results in a substantial improvement in the misfit function and can be a good predictor of the final result. The major weakness of the CG method is its susceptibility to being trapped in local minima, which typically occurs when the arrivals are misidentified. On the other hand, the major advantage of the VFSA method is its ability to escape local minima and proceed forward towards a global minimum. The main disadvantage of the VFSA method is the number of steps required to converge on a final model. Several thousand iterations are typically required to obtain a solution. As mentioned at the beginning of this chapter, computation time is a constraint on the utility of the inversion. The VFSA method converges at a rate proportional to the number of free variables, the width of model space (maximum and minimum allowable values for each variable) and the rate of collapse of the temperature function. The CG method converges at a rate proportional to the number of free variables only, but each CG iteration takes longer than each VFSA iteration, because of the need to calculate the differentials.

One strategy for combining the procedures is to alternate between the two in successive inversion passes, using the result from each pass as the starting model for the next. Chunduru et al. (1997) evaluated several hybrid techniques of this type, applying CG within a VFSA procedure every time certain criteria were met (such as when the misfit function drops by a certain amount). Here, we use a different strategy: we calculate a series of VFSA synthetics over a restricted model space and use them to create differentials for the CG calculation. This allows both procedures to proceed simultaneously, without any additional computational cost. The model space is defined normally for the CG steps, with maximum and minimum values for the free variables established at the start of the program. A smaller model space is created for the VFSA steps, defined by a perturbation around the model result after each CG iteration (figure 24). This allows the VFSA code to sweep through the whole model space as the model result evolves, but prevents it from spending most of its time testing very poor models.

The mixed procedure is as follows:

- Create synthetics for an initial model (m_o) and calculate the misfit (S_o).

  Initialize: $m_{best} = m_o$, $S_{best} = S_o$

- Define a restricted modelspace based on m_o.

  $m_{max} = 1.01*m_o$, $m_{min} = 0.99*m_o$

- Take a series of VFSA steps within this modelspace, calculating the misfit (S_i) for each step. (The number of VFSA steps should be proportional to the number of free variables).

- After each step, apply the VFSA acceptance criteria to the result:

  If $S_i < S_{best}$ then $m_{best} = m_i$

  Otherwise: calculate $P = exp (\Delta S / T)$ and r = a random number between 0 and 1

  If $P > r$ then $m_{best} = m_i$

- Create the differentials (D_i) by subtracting each VFSA synthetic from the initial model synthetic.

  $D_i = d(m_o) - d(m_i)$

- Combine the results linearly to approximate the differential for each model variable.

- Calculate a CG model update (m_{cg}) and its misfit function (S_{cg}) based on those differentials.

  If $S_{cg} < S_{best}$ then $m_{result} = m_{cg}$

  Otherwise, $m_{result} = m_{best}$

- Use the resulting model (m_{result}) as a new starting point and repeat the procedure until the inversion converges.

Each differential step can be thought of as a vector in model space. Typically, the choice of vectors is defined by the set of free variables being inverted, with a unique differential calculated for each free variable at every iteration, but this is not strictly required. All that is necessary is that all the free variables are sufficiently sampled over time. Our method explores a random set of vectors with the same direction never taken twice. Model updates for the free variables are created by taking a linear combination of the vectors, based on the differential results. Using a series of random vectors helps prevent specific model variables from dominating the inversion and allows us to take fewer differentials per step,

speeding up the CG procedure. We obtained good results using half as many differentials as free variables, which doubles the speed of the mixed method relative to a standard CG.

The primary advantage of the mixed procedure is that each method dominates under the same conditions where its strengths dominate. As long as the CG method can find a significantly better model, the inversion proceeds using the CG solution. VFSA becomes more important when the inversion settles into a minimum. The temperature function (T), described above, can be used to adjust how the inversion proceeds and whether the CG or VFSA procedures dominate. At high temperatures, each VFSA model differential samples most of the free variables and the procedure focuses on the broader features of the model. As the temperature drops, the VFSA differentials focus on specific variables, and the procedure becomes more like a standard CG inversion (figure 25). The temperature function governing the acceptance criteria is also important: at high temperatures the VFSA model updates will search through a larger portion of model space.

Synthetic test case

We revisit the synthetic case discussed above (figures 15, 16, 19, 20) to test the mixed inversion method. The model results are shown in figure 26. The inversion was run for 20 iterations with a high corner cutoff frequency of 0.08 Hz, then continued for another 20 iterations with the high frequency cutoff increased to 0.25 Hz. As in the VFSA test, the data were inverted for 17 layers between 325 and 660 km in the first pass and for 13 layers between 414 and 660 km in the second. 8 differential steps were taken for each CG iteration. Note that the result is more heterogeneous than the CG result, but not as heterogeneous as the VFSA result. Figure 27 shows the evolution of the misfit function for the first pass. Circles indicate the misfit for the model update after each CG iteration. Points indicate the result at each step, including for the VFSA differential models. Note that the VFSA steps are clustered around the previous CG update, since they are confined to a model space surrounding that model. For the first several iterations, the misfit function shows the rapid dropoff characteristic of a CG style inversion. As the function settles into a minimum the VFSA results become more important and the inversion occasionally jumps out of the minimum in an attempt to seek a global solution (7th, 17th and 18th iterations).

51
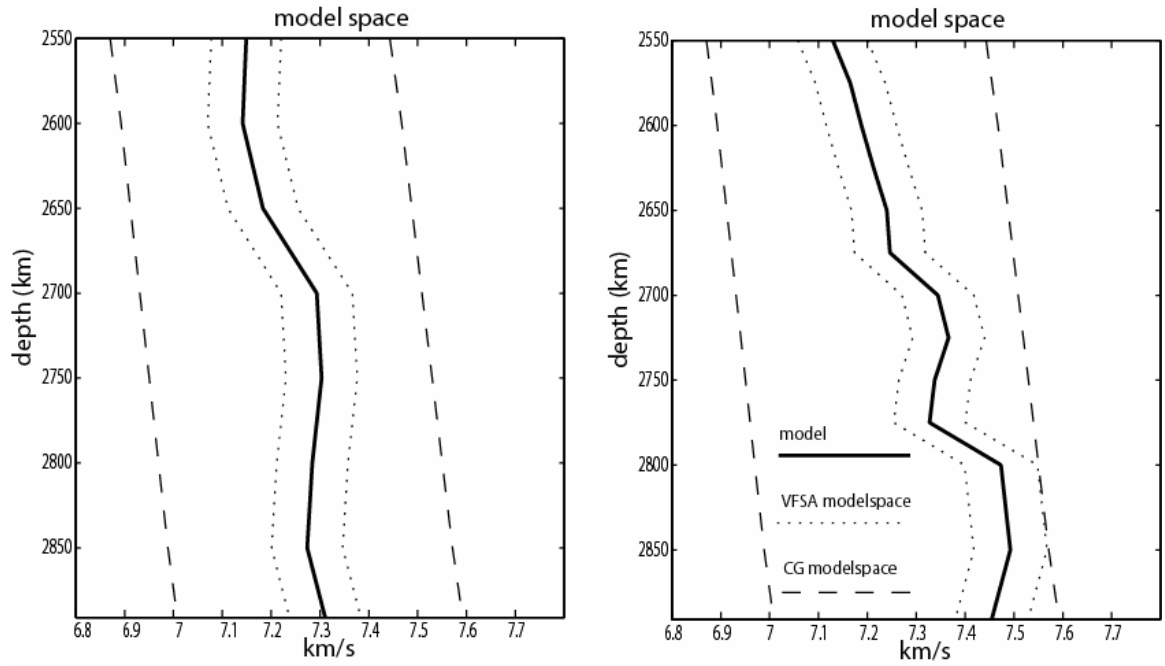
Figure 24. A comparison of the different model spaces used by the CG and VFSA components of the mixed inversion procedure at two different iterations. The CG model result for each iteration (solid lines) is required to fall within the CG model space (dashed lines). The CG model space is the same at all times, but the VFSA model space (dotted line) varies from one iteration to the next and is defined by a variation around the last CG model result.
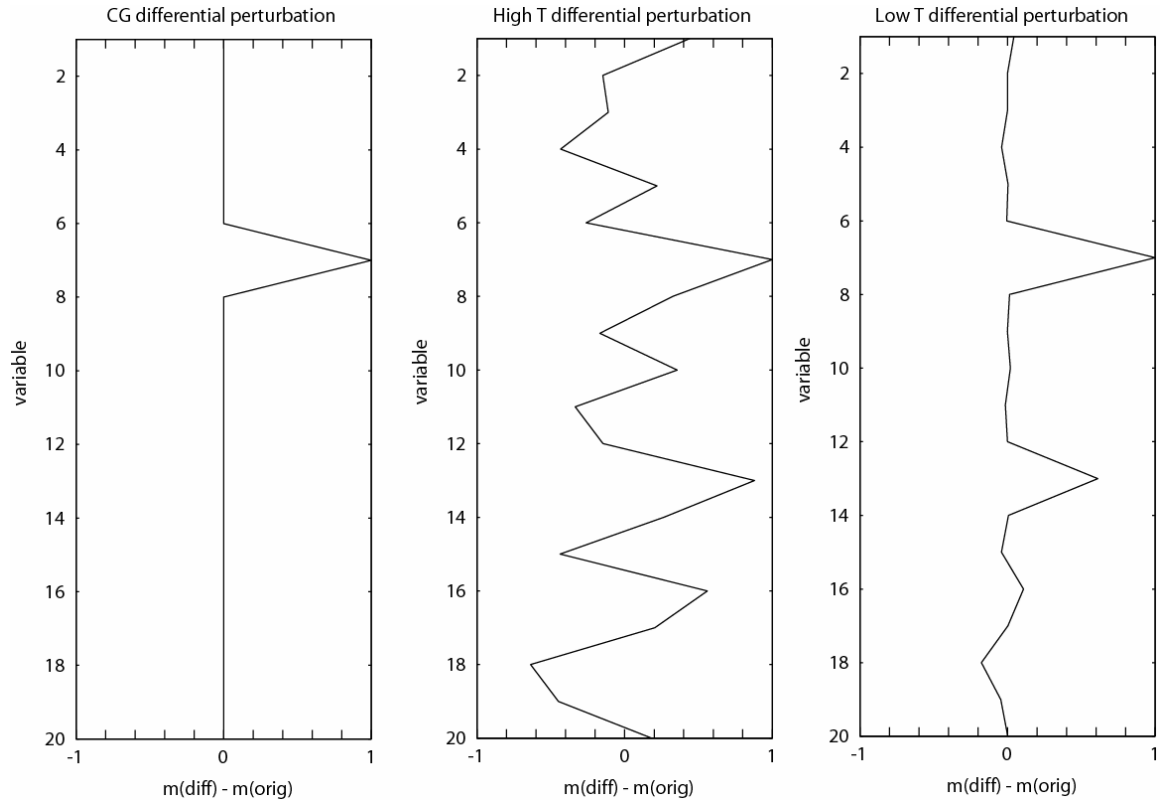
Figure 25. A comparison of differential model perturbations for 3 cases: Each plot represents the difference between the original model and the model used to create the differential synthetics.

(a) The standard CG differential – a single variable is perturbed for each differential.
(b) A VFSA style differential for the mixed procedure at high temperature
(c) A VFSA style differential for the mixed procedure at low temperature
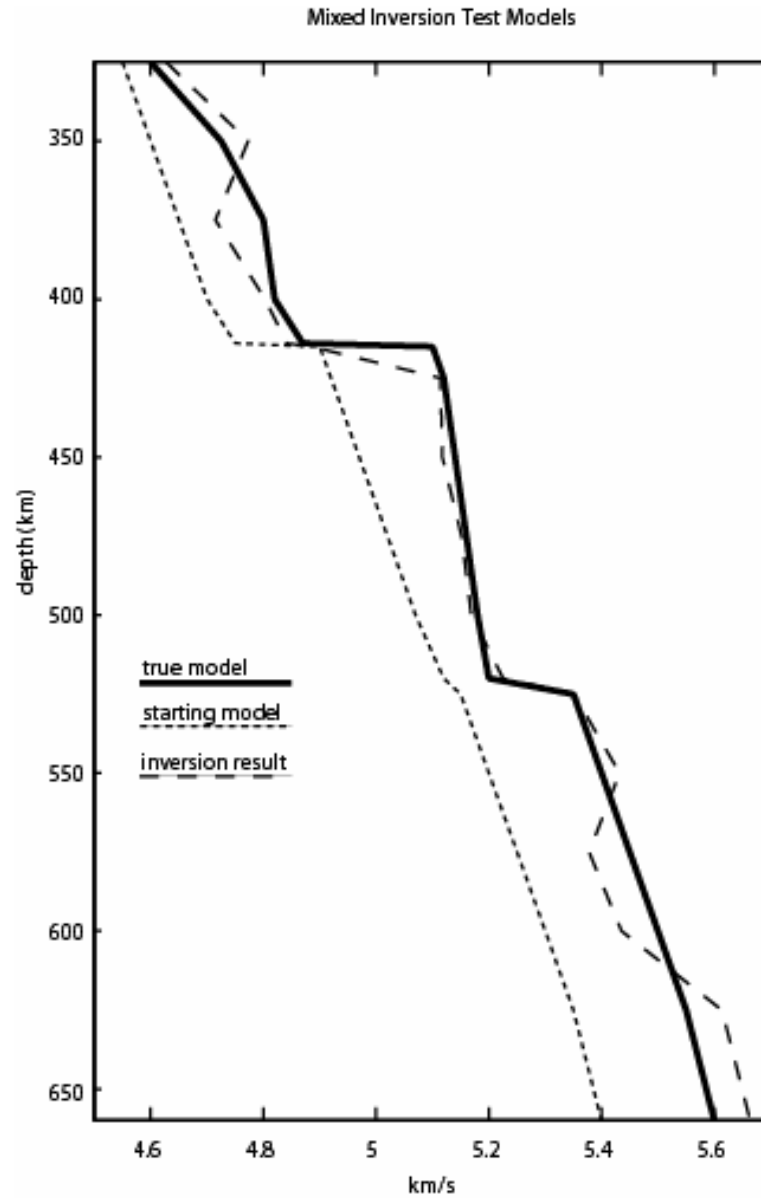
Figure 26. A test of the mixed CG-VFSA inversion procedure. Synthetic seismograms were created for the isotropic S_H velocity model discussed in figure 15 (thick solid line) and used as the data in the inversion test. The inversion was begun using a simple starting model (dotted line) and inverted in two passes of 20 iterations each; first with a high corner frequency cutoff of 0.08 Hz and then with a high corner frequency cutoff of 0.25 Hz.
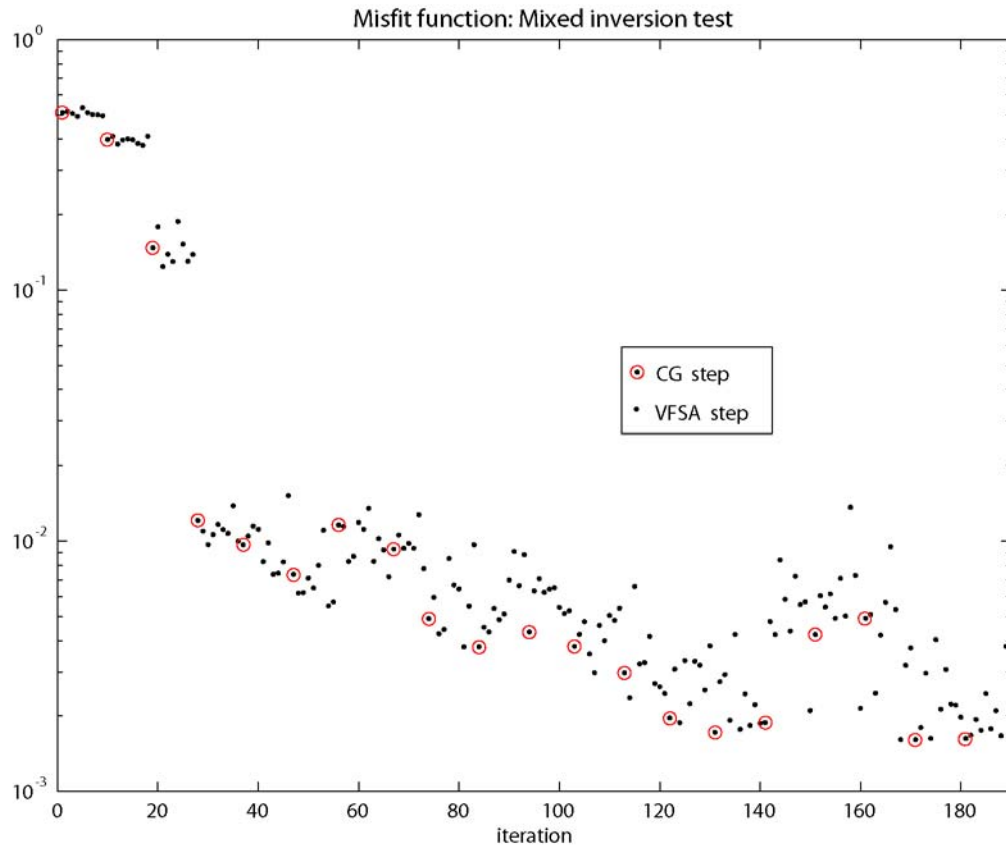
Figure 27. The evolution of the misfit function for the first pass of the synthetic test case described in figure 26. The result for each CG update is denoted by a circle. The result for each VFSA step is marked by a point.

References

Backus, G. E., Long-wave elastic anisotropy produced by horizontal layering, *J. Geophys. Res.*,67, 4427-4440, 1962.

Chunduru R. K., Sen M. K. and Stoffa P. L., Hybrid optimization methods for geophysical inversion, *Geophysics*, 62, 4, 1196-1207, 1997

Fuchs, K. and G. Muller, Computation of synthetic seismograms with the reflectivity method and comparison with observations, *Geophys. J. R. Astron. Soc.*, 23, 417-433, 1971.

Gao, W., Grand, S. P.,Ni, J., Aster, R., Wilson, D., Schlue, J., Baldridge, S., Semken, S., Matzel, E., Mantle seismic structure beneath the Colorado Plateau, Rio Grande Rift and Great Plains from seismic tomography, Eos Trans. AGU, 82(47), Fall Meet. Suppl., Abstract S21F-07, 2001

Gauthier, O., Virieux, J., Tarantola, A., Two-dimensional nonlinear inversion of seismic waveforms: Numerical results, *Geophysics*, 51, 7, 1387-1403, 1986.

Ghose S., Hamburger M. W., Ammon C. J., Source parameters of moderate-sized earthquakes in the Tien Shan, central Asia from regional moment tensor inversion, *Geophys. Res. Letts.*, 25 (16), 3181-3184, 1998

Kennett B.L.N., Engdahl E.R. and Buland R., Constraints on seismic velocities in the earth from travel times *Geophys. J. Int*, 122, 108-124, 1995

Lay, T. and Helmberger, D. V., A lower mantle S-wave triplication and the shear velocity structure of D", *Geophys. J. R. Astron. Soc.*, 75, 799-837, 1983.

Mora, P. Elastic wave-field inversion of reflection and transmission data, *Geophysics*, 53, 6, 750-759, 1988.

Pica, A., Diet, J. P., Tarantola, A., Nonlinear inversion of seismic reflection data in a laterally invariant medium, *Geophysics*, 55, 3, 284-292, 1990.

Randall, G. E., Efficient calculation of complete differential seismograms for laterally homogeneous earth models, *Geophys. J. Int.*, 118, 245-254, 1994.

Rodgers A. J., Walter W. R., Mellors R. J., Al-Amri A. M. S. and Zhang Y. S., Lithospheric structure of the Arabian Shield and Platform from complete regional waveform modelling and surface wave group velocities, *Geophys. J. Int.*, 38 (3), 871-878, 1999

Sen, M. and Stoffa, P. L., *Global optimization methods in geophysical inversion*, Elsevier, 1995.

Swenson J. L., Beck S. L. and Zandt G., Regional distance shear-coupled PL propagation within the northern Altiplano, central Andes, *Geophys. J. Int.*, 139, 3, 743-753, 1999

Tarantola, A., The seismic reflection inverse problem, Inverse problems of acoustic and elastic waves, Soc. Industr. Appl. Mech.,104-181, 1984

Xu, Y. and Wiens, D., Upper mantle structure of the southwest Pacific from regional waveform inversion, *J. Geophys. Res.*, 102, 27,439-27,451, 1997.

Zeng, Y. H. and Anderson, J. G., A method for direct computation of the differential seismogram with respect to the velocity change in a layered elastic solid, *Bull. Seism. Soc. Am.*, 85(1), 300-307, 1995

Chapter 3

The effects of radial anisotropy on body and surface waves: implications for isotropic models of the Earth

Introduction

Radial anisotropy has been widely observed in the Earth, particularly in the top and bottom several hundred kilometers of the mantle, where differences of several percent between the velocities of horizontally and vertically polarized components is typically required to match the seismic data. A mismatch in the travel times of Love and Rayleigh surface waves is often used to identify anisotropy in the upper mantle. Body waves are required to identify anisotropy at greater depths. Typically 2-6% anisotropy is observed in the lithospheric mantle (down to roughly 220 km) (Ekstrom and Dziewonski, 1998, Montagner and Tanimoto, 1991; Gaherty and Jordan, 1995) and in D'' (Kendall and Silver, 1997, Matzel et. al. 1997). Measurements of seismic anisotropy in ophiolite and xenolith samples fall in the same range (Christensen and Salisbury, 1979; Estey and Douglas, 1986; Mainprice and Silver, 1993; Long and Christensen, 2000). Montagner and Kennett (1996) also report a global average 1-2% anisotropy in the transition zone (410-660 km). The mantle outside these depths is generally believed to be isotropic.

Despite the widespread evidence for anisotropy, many studies still model seismic data assuming isotropic structure, often focusing on a single component of the data and solving exclusively for P, S_H or S_V structure. If the mantle is anisotropic, anomalous velocity gradients will appear in the results assuming isotropy and this may affect the final interpretation. Results using different portions of the data (e.g. surface waves vs. body wave arrivals) may be noticeably different and comparisons between different studies may lead to erroneous conclusions about Earth structure.

In this paper, we consider wave propagation through a radially anisotropic medium, and address several questions relating to anisotropy and its implications for seismic studies of the Earth.

- How are P, S_H and S_V phases each affected when they pass through an anisotropic layer?
- What elements of anisotropy (α_h, α_v, β_h, β_v, η) are well resolved for a given data set?
- How does the neglect of anisotropy affect the results of studies assuming isotropy?
- Can we use results of isotropic models to identify the presence, location and magnitude of mantle anisotropy?

Finally, we hope to use our understanding of anisotropy to develop strategies for identifying and modeling radial anisotropy in the Earth.

Anisotropy

In an anisotropic medium physical properties vary as a function of direction. Seismic waves travel through such a medium at velocities which vary as functions of polarization and direction of propagation. Anisotropy in the mantle can have several causes. Most typically, it is attributed to the alignment of anisotropic minerals by tectonic forces and the presence of anisotropy is interpreted in terms of mantle deformation. However, even an inherently isotropic medium can appear anisotropic if there is a preferred structural fabric. For instance, small scale scatterers or a series of thin layers with sharp velocity contrasts can result in anisotropic propagation of seismic waves as long as the heterogeneity is on a scale smaller than the observed seismic wavelength. Backus (1962) illustrated this point by demonstrating that anisotropy with a vertical symmetry axis is equivalent to fine horizontal stratification in terms of seismic wave propagation. Below I summarize the basic equations involved in anisotropic theory. A more thorough discussion can be found in Babuska and Cara (1991).

Seismic anisotropy results from the relationship between stress (σ) and strain (e) from elasticity theory. In the general case, there are 6 independent stresses, 3 normal:

$$\sigma_1 = \lim_{(\Delta A \to 0)} \Delta F_1 / \Delta A_1$$
$$\sigma_2 = \lim_{(\Delta A \to 0)} \Delta F_2 / \Delta A_2$$
$$\sigma_3 = \lim_{(\Delta A \to 0)} \Delta F_3 / \Delta A_3$$

and 3 shear:

$$\sigma_4 = \lim_{(\Delta A \to 0)} \Delta F_2/\Delta A_3 + \lim_{(\Delta A \to 0)} \Delta F_3/\Delta A_2$$

$$\sigma_5 = \lim_{(\Delta A \to 0)} \Delta F_1/\Delta A_3 + \lim_{(\Delta A \to 0)} \Delta F_3/\Delta A_1$$

$$\sigma_6 = \lim_{(\Delta A \to 0)} \Delta F_1/\Delta A_2 + \lim_{(\Delta A \to 0)} \Delta F_2/\Delta A_1$$

(in this notation F_i is the force acting in the direction i, and A_j is the area normal to the vector j)

There are also 6 independent strains, 3 normal:

$$e_1 = du_1/dx_1$$

$$e_2 = du_2/dx_2$$

$$e_3 = du_3/dx_3$$

and 3 shear:

$$e_4 = du_2/dx_3 + du_3/dx_2$$

$$e_5 = du_1/dx_3 + du_3/dx_1$$

$$e_6 = du_1/dx_2 + du_2/dx_1$$

where u_i is the displacement in the direction i, x_j is the original orientation of the line segment being strained and x_1, x_2, x_3 are orthogonal directions.

Hooke's law relates these stresses and strains with the elastic constants C_{ij}.

$$\sigma_i = C_{ij} e_j$$

Since σ_i and e_j each have 6 components, C_{ij} can be represented by a square matrix of 36 elements. Symmetry about the diagonal of this matrix, $C_{ij} = C_{ji}$, means that a maximum of 21 of these elements are independent.

The symmetry of C_{ij} determines the anisotropy of the medium. Increasing symmetry reduces the number of independent elastic parameters. In the isotropic limit (complete

directional independence) only 2 independent parameters remain. Other symmetry systems (about an axis, about a plane, etc.) intermediate between the isotropic and triclinic extremes can be invoked which allow investigations into seismic anisotropy without creating prohibitive demands for data coverage and computing power.

Including anisotropy in the inversion greatly increases the number of elastic coefficients to be resolved. This is the major reason anisotropy is often ignored in seismic investigations. In the most general case, triclinic anisotropy, 21 independent parameters must be resolved at each point in a model.

Radial Anisotropy

A medium that is symmetric about a single axis is transversely isotropic (TI). A medium can appear transversely isotropic if it is finely stratified or if the fast axes of minerals are preferentially aligned within a plane. Seismic waves travel through such a medium at speeds that vary as a function of incidence angle to the symmetry axis. Five independent elastic constants are required to define such a medium. Measurements of seismic velocities within the symmetry plane and along the symmetry axis determine 4 of these constants, while the fifth is determined by the variation of velocity with incidence angle.

We consider the case of radial anisotropy (RA), in which the symmetry axis is vertical (x_3). This is appropriate for horizontally stratified media or for media in which heterogeneities are aligned horizontally. All further discussion will be based on the assumption of radial anisotropy.

Non-zero components of the C_{ij} matrix for a radially anisotropic medium are:

$C_{11} = C_{22} = A$ $C_{33} = C$ $C_{44} = C_{55} = L$

$C_{13} = C_{23} = F$ $C_{66} = N$ $C_{12} = C_{11} - 2C_{66}$

This allows us to write the elastic constant matrix as:

A	A-2N	F	0	0	0
A-2N	A	F	0	0	0
F	F	C	0	0	0
0	0	0	L	0	0
0	0	0	0	L	0
0	0	0	0	0	N

4 of the elastic constants are determined by the density (ρ) and the velocities of horizontally and vertically traveling shear (β_h, β_v) and compressional (α_h, α_v) waves:

$$A = C_{11} = \rho\, \alpha_h{}^2$$
$$C = C_{33} = \rho\, \alpha_v{}^2$$
$$L = C_{44} = \rho\, \beta_v{}^2$$
$$N = C_{66} = \rho\, \beta_h{}^2$$

Anisotropy is often characterized in terms of percent-anisotropy, which relates the vertical and horizontal components ($\alpha\%$ for P anisotropy, $\beta\%$ for S anisotropy). In this paper, we define $\alpha\%$ and $\beta\%$ as:

$$\alpha\% = 100\,(1 - (\alpha_h - \alpha_v)/\alpha_h)$$
$$\beta\% = 100\,(1 - (\beta_h - \beta_v)/\beta_h)$$

The fifth parameter (η) is a measure of velocity as a function of incidence angle with respect to the symmetry axis and can be related to Hooke's law elastic parameters by:

$$C_{13} = \eta(C_{11} - 2C_{44})$$

In the isotropic limit $\eta = 1$, $\alpha_h = \alpha_v$ and $\beta_h = \beta_v$.

Montagner and Nataf (1986) showed that the TI equivalent to a generally anisotropic medium can be determined by averaging over all azimuths. Given the material elastic constants, C_{ij}, the equivalent values of A, C, L, N and F are:

$A = 3/8 \, (\, C_{11} + C_{22} \,) + \frac{1}{4} \, C_{12} + \frac{1}{2} \, C_{66}$

$C = C_{33}$

$L = \frac{1}{2} \, (\, C_{44} + C_{55} \,)$

$N = 1/8 \, (\, C_{11} + C_{22} \,) - \frac{1}{4} \, C_{12} - \frac{1}{2} \, C_{66}$

$F = \frac{1}{2} \, (\, C_{13} + C_{23} \,)$

Estimates of η for the upper mantle range between 0.68 and 1.25 for an olivine model, and between 0.8 and 1.1 based on data from xenoliths and mineral assemblages (Nataf et al, 1986; Kumazawa and Anderson, 1969; Peselnik and Nicolas, 1978; Estey and Douglas, 1986; Ismail and Mainprice, 1998). $\alpha\%$ and $\beta\%$ are as high as 23% and 11%, respectively for the olivine model, and range between 0% and 8 % for various ophiolite and xenolith samples.

The five elastic constants completely define the velocity structure of a homogeneous radially anisotropic medium. Provided with them, the velocities of shear and compressional waves can be calculated as functions of incidence angle θ.

The apparent S_H velocity (β_{SH}) equation involves a simple relationship between the elastic constants associated with the horizontal and vertical shear velocities.

$\beta_{SH}(\theta) = (\, (C_{66} \sin^2\theta + C_{44} \cos^2\theta)/\rho \,)^{\,0.5}$

Note that the velocity function β_{SH} is a sinusoid with a maximum of β_h for horizontally propagating S_H phases and a minimum of β_v for vertically propagating ones.

The equations for the apparent S_V and P velocities ($\beta_{SV}(\theta)$, $\alpha(\theta)$) are more complicated:

$a = (C_{13} + C_{44})^2 \sin^2(2\theta)$

$b = ((C_{11} - C_{44}) \sin^2\theta + (C_{44} - C_{33}) \cos^2\theta)^2$

$c = (a + b)^{0.5}$

$\alpha(\theta) = ((C_{11} \sin^2\theta + C_{33} \cos^2\theta + C_{44} + c)/2\rho)^{0.5}$

$\beta_{SV}(\theta) = ((C_{11} \sin^2\theta + C_{33} \cos^2\theta + C_{44} - c)/2\rho)^{0.5}$

Note that determining β_{SV} and α requires knowledge of 4 of the elastic constants α_h, α_v, β_v and η. Note also that they are independent of β_h.

   These equations for $\beta_{SH}(\theta)$, $\beta_{SV}(\theta)$ and $\alpha(\theta)$ are the key to understanding which elements of anisotropy are resolvable with seismic data and to designing strategies for identifying the presence, location and magnitude of anisotropy in the mantle. It is important to recognize that this dependence of velocity on incidence angle means that different seismic phases (e.g. S, SS, ScS etc.) will travel through an anisotropic layer at different speeds, and corrections relative to isotropic models need to be made even for a single component of the data (S_H, S_V, or P).

   Figure 28 illustrates the relationships of these seismic velocities to the various elastic constants. β_{SH} has a simple, $\sin(\theta)$ relationship to β_h and β_v, and is independent of α_h, α_v and η. Vertically incident S_H phases travel at β_v, horizontally incident phases travel at β_h and intermediate phases travel at speeds in between. This is the simplest of the 3 velocity relationships and the easiest to interpret and correct for. β_{SV} has a $\sin(2\theta)$ relationship to both $\alpha\%$ and η. Vertically and horizontally incident phases both travel at β_v. Phases incident at 45° will travel at either a maximum or a minimum, depending on the combination of $\alpha\%$ and η. For values of θ between 0° and 90°, β_{SV} becomes smaller as $\alpha\%$ becomes larger. Variations in the parameter η have the same effect, β_{SV} decreases as η increases. Since both $\alpha\%$ and η have the same effect on β_{SV}, neither is separately resolvable from S_V data alone, and typically cannot be uniquely determined. α has a complicated relationship to the elastic constants. If $\alpha\%$ is comparable to $\beta\%$ then α has a predominantly $\sin(\theta)$ relationship and the effect of anisotropy on P phases is similar to its effect on S_H phases. If $\alpha\%$ is small, α has a $-\sin(2\theta)$ relationship, the opposite of β_{SV}. This last point implies that isotropic P models are better compared to S_H models, than to S_V models.
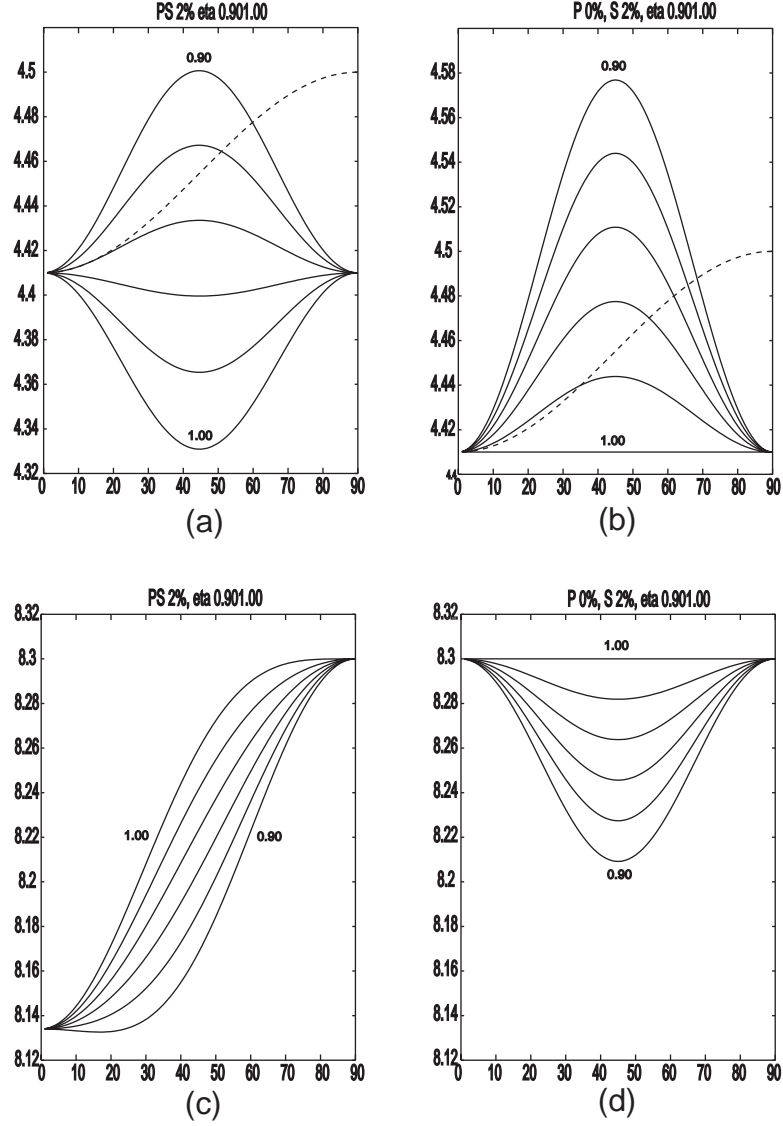
Figure 28. Variations in α, β_{SV} and β_{SH} velocities as functions of incidence angle θ. Two cases are shown: (a) S velocities for a model with $\alpha\%$ and $\beta\% = 2\%$. (b) S velocities for a model with $\alpha\% = 0\%$, $\beta\% = 2\%$. Each solid line is a solution for β_{SV} with a different value of η ranging from 0.90 to 1.00. β_{SH} (dashed line) is independent of both η and $\alpha\%$, but varies with incidence angle. β_{SV} is highly dependent on both η and $\alpha\%$. (c) P velocities for case (a). (d) P velocities for case (b).
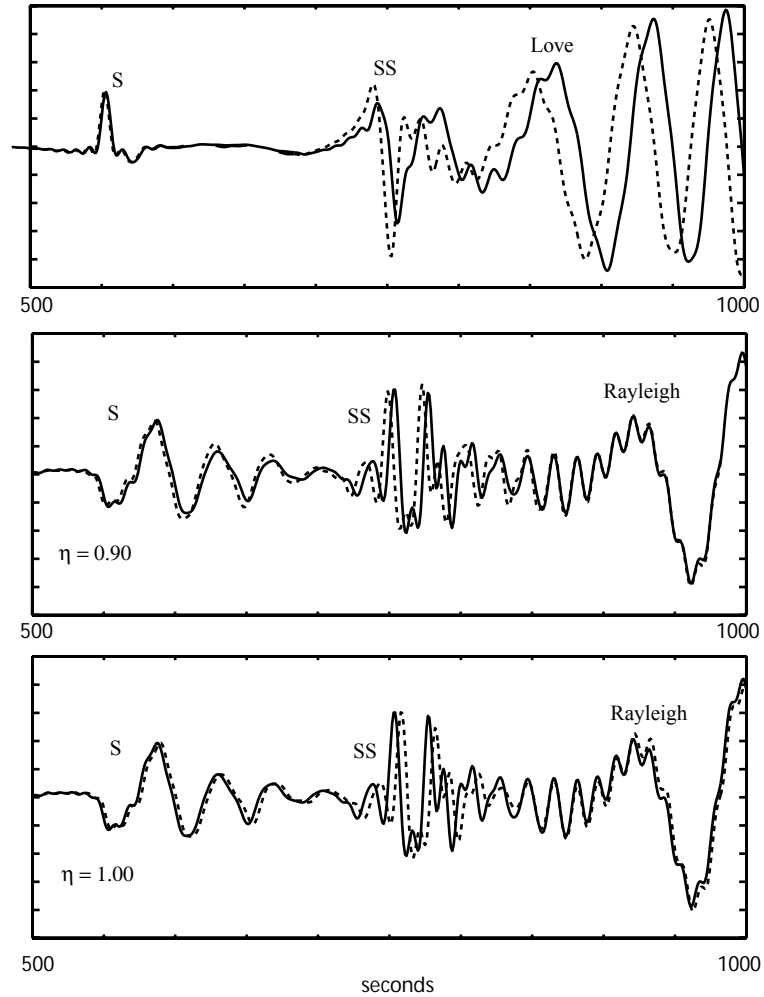
Figure 29. Sensitivity of data to anisotropic structure. Tangential and vertical component synthetics are plotted for an isotropic model (solid line) and a radially anisotropic model (dashed line). The source-receiver offset is 44°. Major arrivals are identified for reference. Each model (isotropic and anisotropic) has the same β_v structure. In the anisotropic model, β_h is 2% faster than β_v from the Moho to 220 km depth. The direct S phase is incident on the anisotropic layer at an angle of about 45°. The SS arrivals are incident at about 60°.
(a) Tangential component synthetics (b) vertical component synthetics, $\eta = 0.90$ (c) vertical component synthetics, $\eta = 1.00$.

Synthetics for isotropic and anisotropic models are compared in figure 29. Each model has the same value of β_v ($\beta_h = \beta_v$ in the isotropic case, β_h is 2% faster than β_v from the Moho to 220 km in the anisotropic case). The figure focuses on shear wave arrivals. The isotropic tangential component arrivals are significantly delayed relative to the anisotropic synthetics, except for the most steeply incident, direct S phase. This implies that S-SS differential times can be noticeably affected by the presence of anisotropy in the upper mantle. The effect on the S_V synthetics is much smaller. Notice that the Rayleigh wave is not very sensitive to η and the contrast between the Love and Rayleigh arrival times is most sensitive to β%. The biggest variation in the S_V synthetics are seen in the SS arrivals, which may be shifted forward or backwards depending on the value of η and α%.

Shear anisotropy (β%) is the best resolved characteristic of radial anisotropy. Notably, for the upper mantle, a good estimate of β%(z) can be obtained from a single multicomponent seismogram, provided it includes good surface wave arrivals and the source location and mechanism are well known. Resolving β% deeper in the mantle requires body waves and more seismograms are needed for depth resolution, but it is possible to resolve β_h and β_v precisely.

P anisotropy (α%) is difficult to resolve. Unlike shear anisotropy (β%), a large number of paths, covering a wide range of incidence angles, is required to discriminate between α_h and α_v. These paths will necessarily sample different structure and a different range of depths and there will always be a tradeoff between anisotropic structure and radial structure in the final model. Furthermore, since the effect of α% on the S_V arrivals is identical to that of parameter η, neither are individually resolvable.

When considering radial anisotropy, several points should be remembered:

- Horizontally propagating phases provide resolution of β_h, β_v, α_h but no resolution of α_v or η

- Vertically propagating phases provide resolution of α_v and β_v, but no resolution of α_h, β_h, or η

- Intermediate angles are sensitive to all 5 components including η and establishing η requires data covering a range of incidence angles

- Radial and vertical component data are insensitive to β_h

Figure 30. Inversion of anisotropic data using an isotropic assumption. 3 component synthetic seismograms were created for a model with $\alpha\%$ and $\beta\% = 2\%$ ($\beta_V < \beta_H$; $\alpha_V < \alpha_H$) from the Moho to 220 km (solid lines). These were used as data in separate inversions of β_{SH} and β_{SV} and α using an isotropic assumption. The results of the inversions are shown (dashed lines).

(a) S structure, $\eta = 0.90$, (b) S structure, $\eta = 1.00$, (c) P structure, $\eta = 0.90$
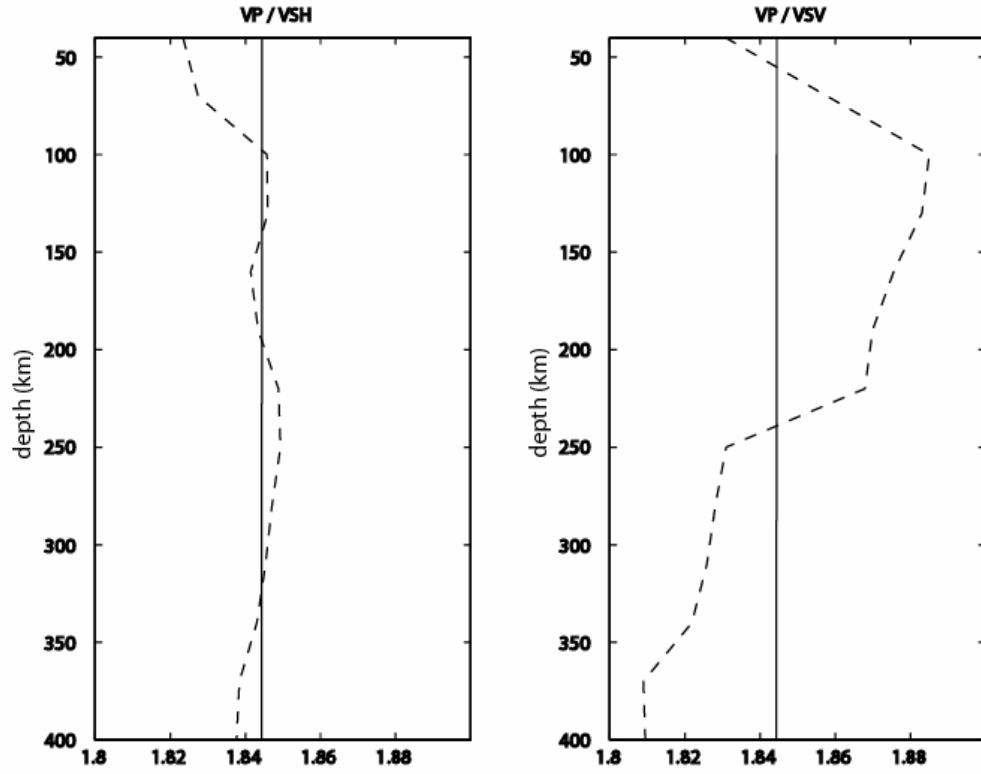
Figure 31. α/β as a function of depth for the models in figure 21. The true ratio (solid line) is 1.844 ($\alpha_h/\beta_h = \alpha_v/\beta_v$).

(a) The isotropic P model result compared to the isotropic S_H model result

(b) The isotropic P model result compared to the isotropic S_V model result, $\eta = 0.90$

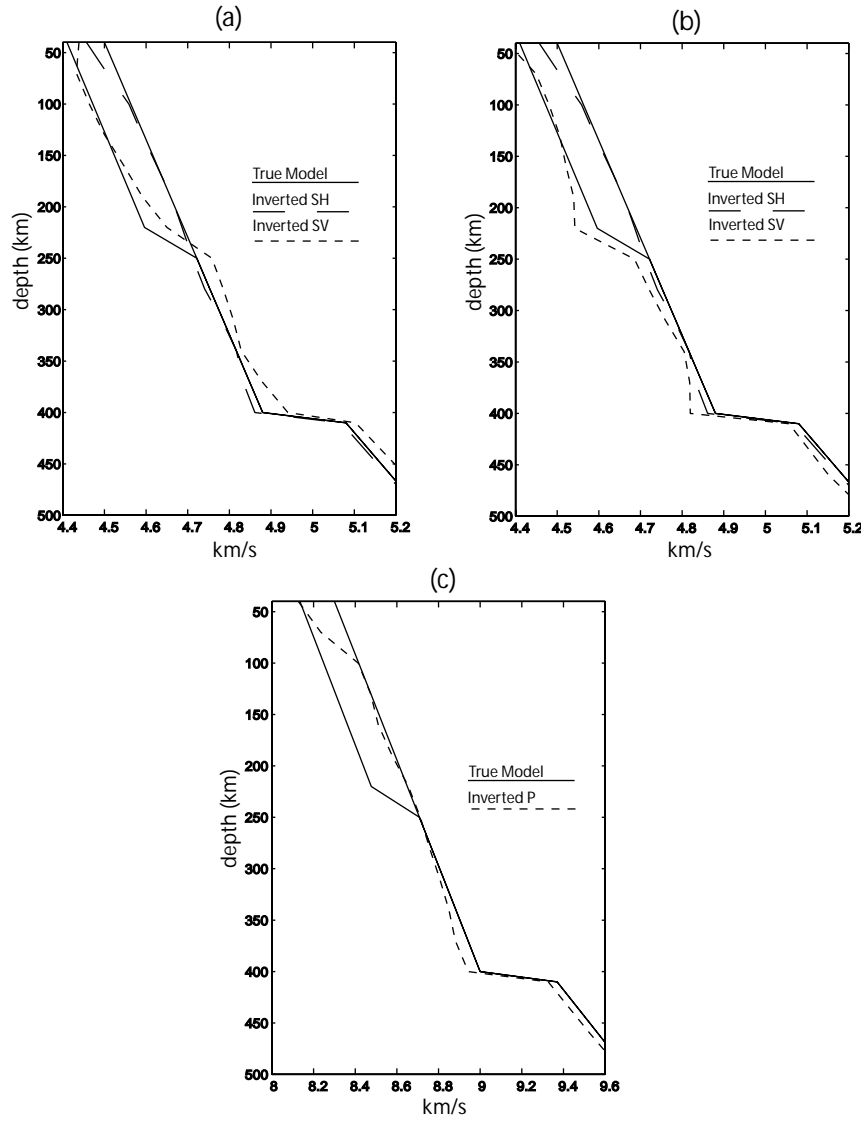Figure 32. Inversion of anisotropic data using an isotropic assumption. 3 component synthetic seismograms were created for a model with $\alpha\%$ and $\beta\% = 2\%$ ($\eta = 0.90$) within the transition zone (solid lines). These were used as data in separate inversions of β_{SH} and β_{SV} and α using an isotropic assumption. The results of the inversions are shown (dashed lines). (a) S structure (b) P structure
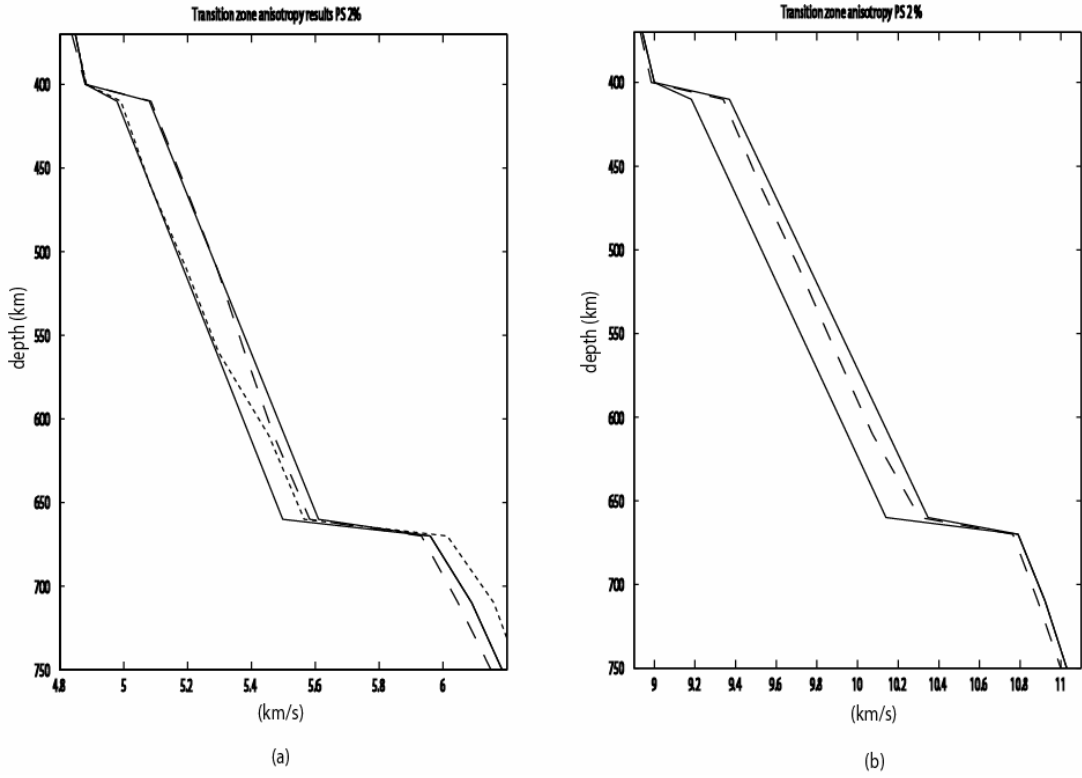
The first point indicates that $\beta\%$ and α_h can be well resolved, provided we select data with phases that are close to grazing incidence at the depth we're interested in. This type of geometry has been used to detect anisotropy in D" and in the transition zone where surface waves have little sensitivity. The second point implies that studies focusing on more vertically incident phases have little sensitivity to radial anisotropy and are best related to models of S_V.

Implications for isotropic Earth models

Among the questions we wish to address in this study are how the neglect of anisotropy affects the results of isotropic studies and how we can correct and interpret those results in terms of Earth structure. Since S_H, S_V, and P arrivals are all affected when they pass through a radially anisotropic layer, single component models developed with an isotropic assumption will mistakenly map anisotropic wave propagation into structural heterogeneity where none exists. Furthermore, since anisotropy affects these components in different ways, the results of different studies may not be readily comparable. Finally, because of the dependence of velocity on incidence angle, the same data set will result in different Earth models depending on whether a study focuses exclusively on surface waves, on body waves, or uses the full waveform.

To understand how the neglect of anisotropy affects the results of studies assuming isotropy, we performed a series of synthetic tests. We imagined a hypothetical seismic array of 36 stations arranged along a line with 1° spacing between the stations. Synthetics for an anisotropic model were used as the data in separate isotropic inversions for β_{SH}, β_{SV} and α. A single source was used at an offset ranging from 15° to 50° from the receivers. At these distances, several direct and multiple S and P phases appear in the data along with Love and Rayleigh surface waves. The inversion method was designed to match the timing and amplitude of the full waveform including both body and surface waves. We tested a number of cases, varying the size and location of anisotropy in the model and comparing the isotropic inversion results to the horizontal and vertical components of α and β. It is typically possible to match the data perfectly with isotropic models when focusing on a single component (radial, vertical or tangential). When focusing on all components it is not. Figure 30 shows

the results of a simple case with $\alpha\%$ and $\beta\% = 2\%$ down to 220 km. The S_H result is very close to the value of β_h, although it becomes relatively slower with depth since the phases that travel more deeply are more vertically incident on the anisotropic layer (and thus travel through it more slowly than the shallow phases). The P result is very similar, tracking close to the value of α_h. The apparent S_V models can differ significantly from β_v. The size of the difference is completely dependant on the combination of $\alpha\%$ and η. Notice that by comparing the isotropic S_V and S_H model results we can get a rough estimate of the location and magnitude of anisotropy, although the specifics are not correct. Comparing these models, we also see an apparent anisotropy extending down into the transition zone.

One of the measures that is often used to characterize mantle petrology is the ratio of P to S velocities (α/β). A change in α/β may be interpreted as a change in partial melt content, or in composition. Significantly different interpretations may result if anisotropy is neglected, depending on whether a P model is compared to an S_V model, or to an S_H model. It may seem intuitive to compare the S_V and P models since these phases are coupled and appear on the same components of the seismogram. However, anisotropy has a different effect on S_V and P arrivals and large anomalies can result if they are compared. Figure 31 compares the P and S results for the simple model shown in figure 30. The true ratio is 1.844 throughout the model. Even for this model, with a relatively small amount of anisotropy (2% down to 220 km), we see a 4% variation in α/β when comparing the isotropic S_V result to the isotropic P result. The S_H and P models provide a much better estimate of the true ratio.

Figure 32 presents the results for a model with 2% anisotropy exclusively in the transition zone. The S_H and S_V results track β_h and β_v through the top 150 km of the transition zone. This is due to the large number of SS arrivals turning in that depth range. The results diverge from β_h and β_v below that depth as the more steeply incident direct arrivals begin to dominate the sensitivity matrix.

While the result for an isotropic inversion of anisotropic data is far from the true Earth structure, it can be used as rough guide to evaluate the presence and magnitude of anisotropy in the data. For an isotropic Earth the S_V and S_H models should be identical. When the S_H and S_V results are different, anisotropy is indicated. The isotropic result provides a good estimate of the magnitude and depth extent of anisotropy in the subsurface. This

72

observation can then be used to create an initial model for an anisotropic inversion simultaneously using all 3 components of the data.

Strategies for identifying radial anisotropy in the mantle

We can use the results discussed above to design strategies for identifying and modeling anisotropy in the Earth. The key is to isolate data that are sensitive to specific elastic parameters, solve for them independently and progressively combine them to get a maximum resolution of the anisotropic components. The first requirement is to obtain multicomponent data with good P, S_H, and S_V arrivals. To begin, these data can be modeled separately, using an isotropic assumption. The results can then be compared to evaluate whether corrections need to be made. If the S_H and S_V results are identical, an isotropic assumption may be justified. If they are significantly different, it will not be. We've already illustrated that comparing separate isotropic models can provide a rough estimate of the location and magnitude of anisotropy. These results can then be used as a starting point in an anisotropic modeling procedure, solving simultaneously for all components.

Anisotropy in the shallow mantle is easiest to resolve, since its effect on Love and Rayleigh surface waves is very easy to see. Surface waves provide a good estimate of the mean anisotropy as a function of depth, although the resolution becomes progressively poorer with depth so that the gradient of anisotropy as well as the base of the anisotropic layer are often difficult to accurately resolve. Body wave arrivals are much more sensitive to sharp changes in velocity and by including them along with the surface waves we can obtain good resolution of upper mantle anisotropic structures. In particular, if a data set includes body waves that are at grazing incidence in the upper mantle, differences in the S_H and S_V arrival times are very sensitive to $\beta\%$ near the grazing depth.

Body waves are required to resolve anisotropy deeper in the mantle. When concentrating exclusively on body wave arrivals, the best way to determine anisotropy is to first identify grazing phases, which provide good resolution of β_h, β_v, and α_h and gradually include phases that pass more vertically through the zone of interest, giving some resolution of α_v and η. For the transition zone this typically means finding triplicated direct and multiple arrivals produced by the 410 and 660 km discontinuities. A number of these appear in

seismograms at offsets between 20° and 50°. For D", data in the $70^{o} - 100^{o}$ range contain the necessary arrivals. Grazing phases are the direct (S, P), and the diffracted (Scd) arrivals, while constraints on η and $\alpha\%$ come from the more steeply incident core reflected (ScS, PcP) or core traversing (SKS, PKP) phases. However, if anisotropy is also present at shallower depths it needs to be accounted for before it is attributed to anisotropy in the transition zone or in D". Note the results of the test presented in figure 30. In that case, differences in SS_H and SS_V arrival times seem to be due to structure in the transition zone, but are actually entirely due to the anisotropy in the top 200 km of the mantle.

Conclusions

The presence of anisotropy in the Earth affects the propagation of both surface and body waves. If anisotropy is neglected, timing and waveform anomalies will be incorrectly understood and may result in false tectonic, structural or compositional interpretations of the data. This affects the use of differential travel times to isolate structure, the use of α/β ratios to make petrological interpretations and the comparison of models developed using different data types to characterize regional heterogeneity. We believe the results discussed above provide a solid argument for using multicomponent data to solve simultaneously for P, S_H and S_V earth structure. This approach should identify complications due to anisotropy that can be corrected to provide a better image of the subsurface. To summarize the most important conclusions:

- Surface waves provide a good measure of the mean anisotropy as a function of depth for the shallow mantle
- Body wave arrivals provide resolution of anisotropy at greater depths as well as a sharper image of the cutoff depth of the anisotropic layer and a better estimate of the gradient of anisotropy within the anisotropic layer.
- $\beta\%$ and α_h are typically well resolved by multicomponent seismic data.
- $\alpha\%$ and η are poorly resolved and trade off with one another in terms of their effect on S_V arrivals.

74

- Erroneous heterogeneity will be mapped into models if anisotropy is neglected. The size of the heterogeneity will be proportional to the magnitude of anisotropy present and extend well below the anisotropic zone.
- The effects of anisotropy on P models produced with an isotropic assumption are most similar to the effects on isotropic S_H models. When comparing isotropic models, α/β_{sh} is therefore a better measure than α/β_{sv} for characterizing mantle petrology.
- Isotropic S_H, S_V and P models developed separately using the same data set can provide a good initial estimate of the presence, location and magnitude of anisotropy.

References

Babuska, V. and M. Cara., <u>Seismic Anisotropy in the Earth</u>, Kluwer Academic Publ., Boston, 1991

Backus, G. E., Long-wave elastic anisotropy produced by horizontal layering, *J. Geophys. Res.*,67 (11), 4427-4440, 1962.

Christensen, N. I., and Salisbury, M. H., Seismic anisotropy in the oceanic upper mantle: evidence from the Bay of Islands ophiolite complex, *J. Geophys. Res.*, 84, 4601 – 4610, 1979

Ekstrom, G. and Dziewonski, A. M., The unique anisotropy of the Pacific upper mantle, *Nature*, 168-172, 1998.

Estey, L. H., and Douglas, B. J., Upper mantle anisotropy: a preliminary model, *J. Geophys. Res.*, 91 (11), 11,393-11406, 1986.

Gaherty, J. B., and Jordan, T. H., Lehmann discontinuity as the base of an anisotropic layer beneath continents, *Science*, 268, 1468-1471, 1995.

Ismail, W. B. and Mainprice, D., An olivine fabric database: an overview of upper mantle fabrics and seismic anisotropy, *Tectonophysics*, 296, 145-157, 1998

Kendall, J. M., and Silver, P. G., Constraints from seismic anisotropy on the nature of the lowermost mantle, *Nature*, 381, 409-412, 1996.

Kumazawa, M. and Anderson, O. L., Elastic moduli, pressure derivatives and temperature derivatives of single crystal olivine and single crystal forsterite, *J. Geophys. Res.*, 74, 5961-5971, 1969

Long, C. and Christensen, N. I., Seismic anisotropy of South African upper mantle xenoliths, *EPSL*, 179, 551-565, 2000

Mainprice, D. and Silver, P. G., Interpretation of SKS-waves using smaples from the sub continental lithosphere, *Phys. Earth Planet. Inter.,* 78, 257 – 280, 1993

Matzel, E., Sen, M. K. and Grand, S. P., Evidence for anisotropy in the deep mantle beneath Alaska, *Geophys. Res. Lett.,* 23, 18, 2417-2420, 1996

Montagner, J.-P., and Kennett, B. L. N., How to reconcile body wave and normal mode reference earth models, *Geophys. J. Int.*, 125, 229-248, 1996

Montagner, J.-P., Nataf, H. C., A simple method for inverting the azimuthal anisotropy of surface waves, *J. Geophys. Res.*, 91, 511-520, 1986.

Montagner, J.-P., Tanimoto, T., Global upper mantle tomography of anisotropy of seismic velocities and anisotropies, *J. Geophys. Res.*, 96, 337-20,351, 1991.

Nataf, H.-C., Nakanishi, I. and Anderson, D. L., Measurements of mantle wave velocities and inversion for lateral heterogeneities and anisotropy: 3. Inversion, *J. Geophys. Res.*, 91, 7261-7307, 1986

Peselnik, L. and Nicolas, A., Seismic anisotropy in an ophiolite peridotite: application to oceanic upper mantle, *J. Geophys. Res.*, 83, 1227-1235

Chapter 4

The Anisotropic Seismic Structure of the East European Platform

Introduction

Continental cratons are large regions of the Earth's crust that have remained relatively undeformed since the Precambrian. These ancient continental platforms are observed to be seismically distinct from younger provinces with higher seismic velocities well into the mantle. How deeply the differences extend remains an open question. Mantle xenoliths from kimberlite magmas provide direct evidence for the petrology and stratigraphy of the cratonic mantle to a depth of about 200 km and can be used to interpret seismic results (Kopylova et al, 1998; O'Reilly and Griffin, 1996). These observations have significant implications for the style of convection in the mantle and the evolution of continental lithosphere over time.

Seismic velocities beneath cratons are significantly higher than average and may represent differences in both temperature and composition. Estimates for the lower boundary of continental cratons range between 150 and 410 km depth (Gaherty et al., 1999; Li et al., 1998; Jordan, 1988). Low velocity zones beneath a seismic lid at about 150 - 200 km are common in several models (Pavlenkova et al., 1996; Lefevre and Helmberger, 1989; Grand and Helmberger, 1984; Given and Helmberger, 1980), but absent or very deep in others (Gaherty et al., 1999; Zhao et al., 1997; Vinnik et al., 1996). This may be a fundamental difference between cratons or a consequence of the different methods used to determine the seismic structure.

This study focuses on the seismic structure of the East European platform, a Precambrian age structure that comprises most of Russia west of the Urals (figure 33) that has remained relatively undeformed since 1.6 Ga. (Glebovitsky, 1997; Zonenshain et al., 1990). The objectives are to simultaneously model the P and S velocity structure of the upper mantle, place constraints on the depth extent and magnitude of anisotropy throughout the upper mantle and compare these results to models for other cratonic regions.

The data are 3-component broadband seismograms from strike-slip earthquakes located near the edge of the platform and recorded in Russia and Europe. The timing,

amplitude and interference characteristics of direct arrivals (S, P), multiply reflected arrivals (SS, PP), converted phases and surface waves provide very good radial resolution throughout the upper 400 km of the mantle. We tested 1-dimensional isotropic and radially anisotropic Earth models. The data are best matched by a model that includes a radially anisotropic lid (5% S anisotropy) extending to a depth of 200 km. Anisotropy drops to 2% from 200 - 250 km and below that the mantle is isotropic.

Seismic Phases

Seismic data provide a tremendous amount of information about the Earth's interior. Each seismogram includes direct and multiply reflected arrivals, converted phases and surface waves. The data are complicated by the large number of arrivals present, and this complexity makes extracting most information difficult. In addition, the 3 components of each seismogram (vertical, radial and tangential) are sensitive to different phases. The tangential component isolates purely S_H motion and contains only S body phases and Love waves and has been used extensively to obtain S wave structure in the Earth. The radial and vertical components contain both P and S_V components including the Rayleigh waves. Love and Rayleigh surface waves provide some of the best constraints on the shallow part of the mantle (less than about 200 km depth). Body wave arrivals are more sensitive to deeper structure. Many studies use only a small portion of the data available, focusing for instance on travel times or specific phases, discarding the rest or treating it as noise. As computation speeds have increased and methods for generating full response synthetics have been developed, more of the data have become accessible to interpretation. In this study, we use the full waveform, from the start of the first body wave through the surface waves, to determine velocity as a function of depth.

We use data in the distance range $10^o - 50^o$. At these distances, the direct S and P and multiple phases SS and PP traveling above the 410 km and 660 km discontinuity can all be readily observed on seismograms (figure 34). The timing, amplitude, and interference characteristics of these phases provide excellent constraints on the seismic structure of the upper mantle.

79
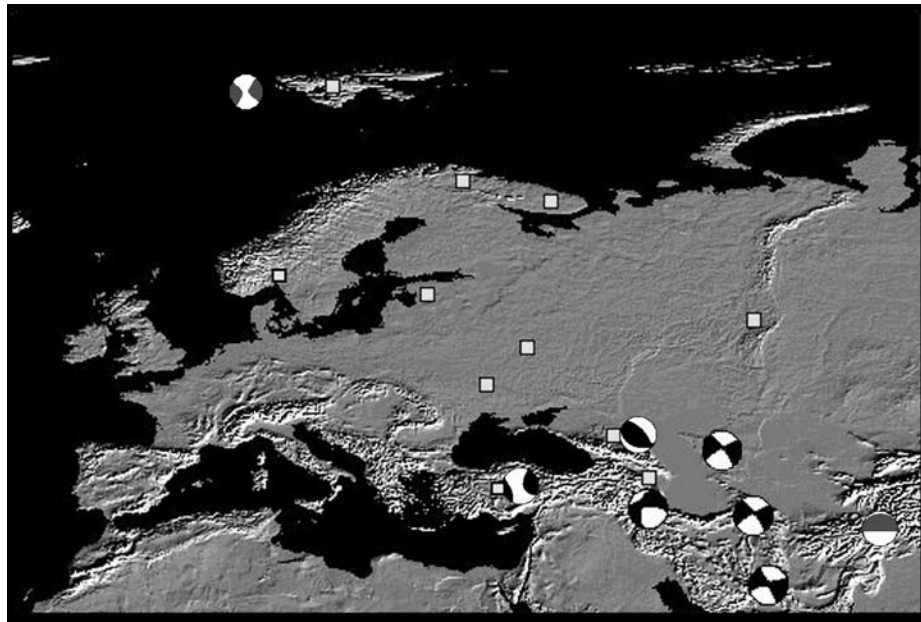
Figure 33. A map of the study area including the earthquake sources (beachball figures) and seismic stations (white squares) used. The East European Platform includes most of Russia west of the Urals.
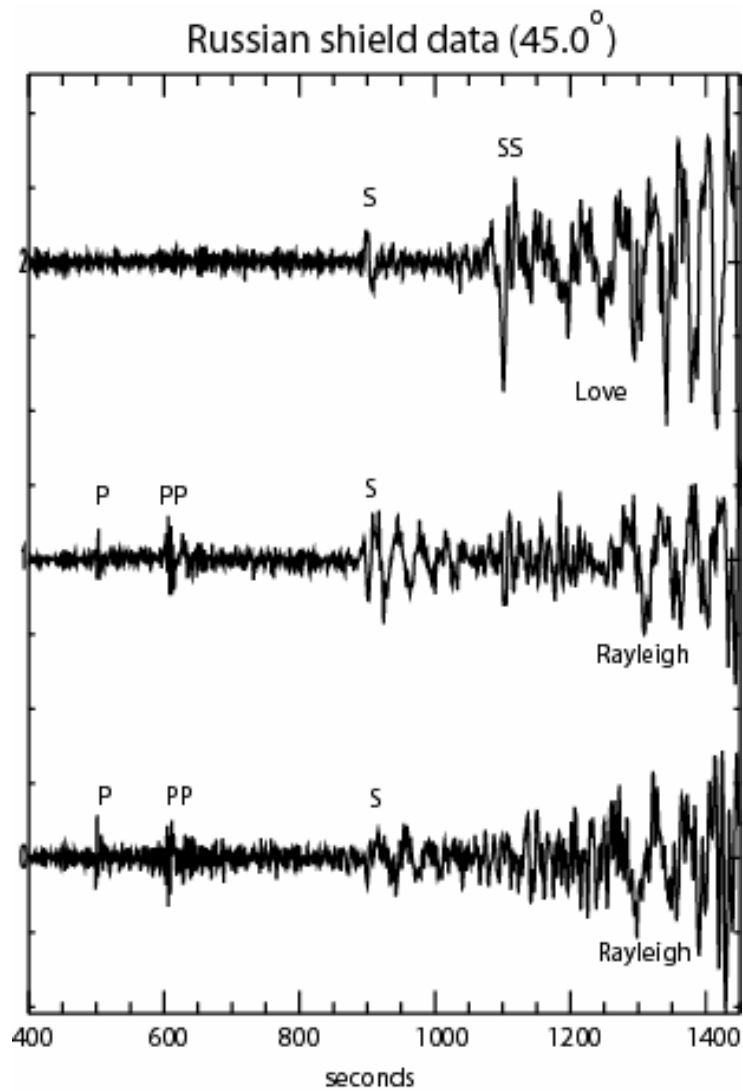
Figure 34. Unfiltered tangential, radial and vertical component data for a shield path at 45°
distance. Major arrivals are identified for reference including the Love and Rayleigh surface
waves.

Seismic Anisotropy in the Earth's Mantle

Anisotropy is an inherent feature in most minerals and mineral assemblages found in the upper mantle (Kern, 1993; Nicolas and Christensen, 1987). These anisotropies tend to average out over the large scale if individual crystals are oriented randomly. However, if some force tends to align them, the medium as a whole can become anisotropic.

Seismic studies generally have concluded that the upper mantle is highly anisotropic, but the location, extent and magnitude of this anisotropy are uncertain (Ekstrom and Dziewonski, 1998, Montagner and Tanimoto, 1991; Gaherty and Jordan, 1995). Anisotropy is often represented as a radially anisotropic layer with several percent differences between the vertical and horizontal seismic speeds. It is typically observed by measuring the mismatch of Love and Rayleigh surface waves, or by a mismatch in the arrival times of body wave phases such as S_H and S_V (Gaherty et al., 1999). Figure 35 illustrates the effect of anisotropy on the tangential (S_H) and radial (S_V) components of teleseismic data. Surface wave measurements have poor resolution below about 200 km depth, and measurements of anisotropy from body wave phases integrate the effects of anisotropy along the path length. Travel paths that pass through different tectonic regions of the mantle also often complicate the data.

It should be noted that anisotropy and small scale heterogeneity are indistinguishable to long wavelength seismic waves. An inherently isotropic medium with heterogeneity on scales smaller than a seismic wavelength can generate anisotropic effects. For instance, small scale scatterers or a series of thin layers with sharp velocity contrasts can result in anisotropic propagation of seismic waves. Backus (1962) illustrated this point by proving that radial anisotropy is equivalent to fine horizontal stratification. Ryberg et al. (1995) proposed an earth model containing small scale horizontally elongated scatterers extending to 100 km depth beneath northern Eurasia to explain the P_n coda on short period seismograms and such a structure could also produce anisotropic phenomena. Additionally, a stack of azimuthally anisotropic layers, with different fast axis orientations may average out the azimuthal component of anisotropy, but the radially anisotropic component could be preserved (Saltzer et al., 2000; Jordan et al., 1999; Gaherty and Jordan, 1995). Such interpretations should not be excluded from our conclusions, since in either case, the result is produced by a preferential orientation of rocks in the subsurface.

Seismic anisotropy in the upper mantle is typically attributed to the alignment of olivine due to tectonic forces (Artyushkov, 1984; Anderson, 1989). This implies that measurements of anisotropy are directly related to mantle flow and deformation. A critical element desired in analyses of seismic anisotropy is an explicit demonstration of the location and depth extent of the anisotropy. This is important because anisotropy can be a result of relict flow frozen into the lithosphere or active deformation in the asthenosphere. In the first case it represents an historical record of tectonism, in the second it is a picture of present day convection.

It is also important to consider anisotropy when comparing different seismic models. S models, for instance, often focus on either the radial component (S_V) or tangential component (S_H) of the data. When comparisons are made between such data sets, variations may be interpreted as fundamental differences in Earth structure. If the subsurface is isotropic this is unimportant, if anisotropic it is not. Neglecting anisotropy can also bias isotropic models because the velocity of a ray through an anisotropic medium is a function of incidence angle (Regan and Anderson, 1984) as discussed in detail in chapter 3.

Data

The data used in this study are 3-component broadband seismograms from 8 moderate magnitude (5.5 - 6.5 Mb) earthquakes located near the East European platform and recorded in Russia and Europe (figure 33). The data were selected based on several criteria: First, the majority of the source-receiver path had to fall within the EEP. This required selecting sources and receivers within the platform or as close to it as possible. Second, we wanted moderate magnitude events, with simple source-time functions and good signal-to-noise ratios.

Small magnitude earthquakes are numerous, but attenuation makes them poor candidates for teleseismic studies, especially when looking for subtle details such as small arrivals and timing mismatches. Large magnitude earthquakes, on the other hand, are rare and often have complicated source time functions that can complicate interpretation. The moderate magnitude sources used here provide good signal, relatively simple source time functions, and consistency of data.

We chose source-receiver combinations at offsets between 10° and 50° because they include identifiable direct arrivals, multiple arrivals and surface waves that can be used to isolate structure at various depths in the upper mantle. A total of 45 seismograms from 8 sources make up the data set (table 1). Direct (S,P) and multiply reflected (SS, PP) arrivals, converted phases and surface waves are all readily identifiable on the seismograms and provide very good resolution of the upper mantle radial structure.

A significant problem for our study of the EEP is the limited number of available seismic stations. This coupled with our requirement that the source-receiver paths predominantly sample the platform results in a NW-SE bias in the path coverage. Most of the seismicity falls to the south of the platform and most of the available stations fall to the north and west of those sources. ARU is the only station near the eastern edge of the platform and source-receiver offsets to ARU fall between 18°-28°. Our only northern event (3/21/1998) is located within 216 km of our northernmost station, KBS, and the source-receiver paths sampling the platform also fall along a NW-SE arc. This bias in path coverage means that azimuthal anisotropy is poorly resolved and that our results might best be interpreted as valid for a corridor within the platform rather than the platform as a whole. Because of the limited data set, we proceeded with two assumptions: first, that the platform can be generally described by a 1-D radially anisotropic structure and second, that azimuthal anisotropy in the platform is small or averages out over the path lengths involved. The assumption of lateral homogeneity is supported by the results of Marquering and Snieder (1996) and 2D profiles of Paulssen et al. (1999). Vinnik and Ryaboy (1981) found that the average upper mantle azimuthal anisotropy in the platform does not exceed 0.5%.

Inversion Method

We have developed a procedure for the efficient inversion of seismic waveforms to produce structural models of the Earth's mantle. Our technique is an iterative, nonlinear method combining the advantages of simulated annealing and least-squares gradient techniques (Sen and Stoffa, 1995; Tarantola, 1984; Mora, 1988). The variables in the problem are the seismic velocities (α and β) and the density (ρ) as a function of depth. When inverting for radial anisotropy this set is expanded to include the five variables that determine the
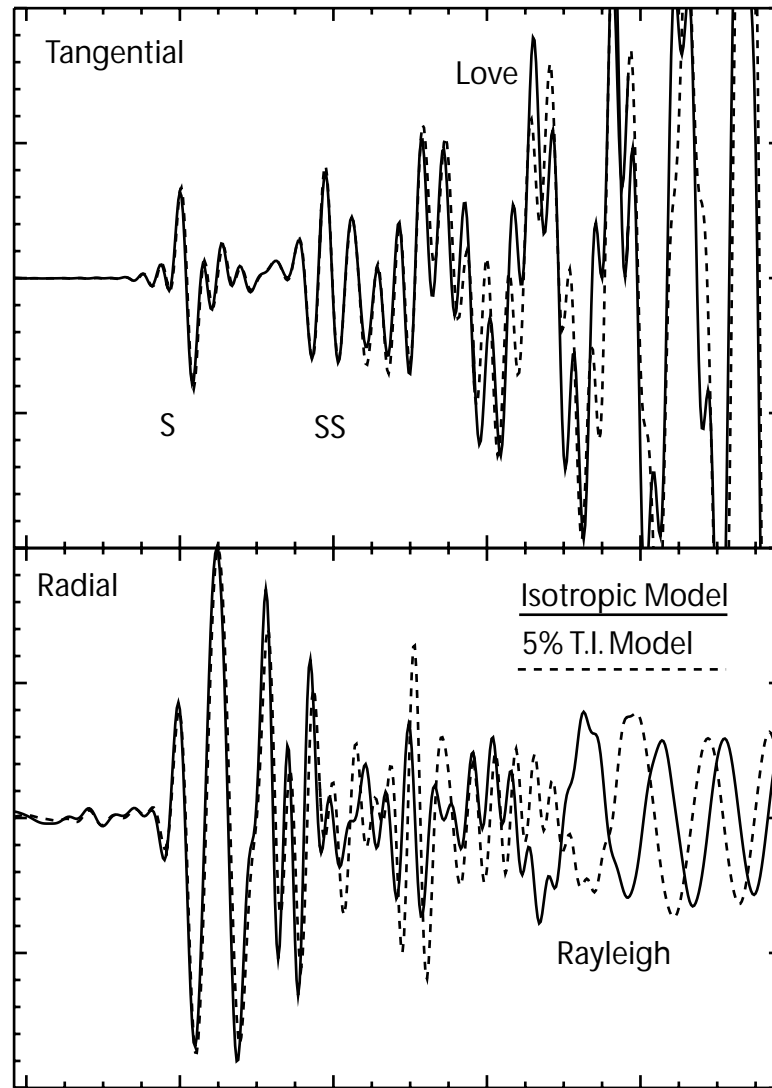
Figure 35. Sensitivity of data to anisotropic structure. Tangential and radial component synthetics are plotted for an isotropic model (solid line) and a radially anisotropic model (dashed line). Major arrivals are identified for reference. Both models (isotropic and anisotropic) have the same S_H structure. In the anisotropic model, β_V is 5% slower than β_H from the Moho to 200 km depth. The anisotropic radial component arrivals (both body and surface waves) are significantly delayed relative to the isotropic synthetics. The tangential component synthetics show little sensitivity to anisotropy, except for the most steeply incident body wave arrivals

seismic velocities in a radially anisotropic medium (α_H, α_V, β_H, β_V, η). The technique is discussed in detail in chapter 2.

Synthetic Test Case

We ran a synthetic test case in order to estimate how well upper mantle structure was resolved by this data set (figure 36). Synthetic data were created for an isotropic S_H velocity model (solid line) and used as the data in an inversion test. The combination of source-receiver offsets and source mechanisms used were identical to those in the real data set. A significantly different S_H model was used as a starting point in the inversion (dashed line) which was run using the conjugate-gradient procedure. The dotted line shows the results of the 5th iteration in the inversion test. Notice how the model most rapidly solves for the shallowest part of the mantle structure. This is because of the inclusion of surface waves in the inversion. They dominate the mismatch between synthetics and data because of their large amplitude and long period. As the fit to the top of the model improves, the mismatch of the body wave arrivals makes up a more significant percentage of the error function and deeper structure is resolved. After 25 iterations (dashed-dotted line) the inversion has matched all the major features in the true model. This illustrates both the ability of the inversion code to model seismic waveform data and that this data set contains sufficient information to constrain the radial upper mantle structure beneath the East European platform.

One of the consequences of the presence of anisotropy in the lid is that isotropic models of the upper mantle will incorrectly map anisotropic phenomena into variations in seismic velocity structure. An example of this is presented in figure 37. Synthetics for an anisotropic model were used as the data in an isotropic inversion of shear velocity. β_H and β_V were inverted separately in the test. Notably, the inversion provides a match for both β_H and β_V at the top of the mantle but low velocity structure is mapped into the S_H model at the base of the lid and high velocity structure is mapped into the S_V model. We compare the synthetic result to two isotropic models for the Canadian shield. SNA (Grand and Helmberger, 1984) was modeled using S_H waveform data, NA95 (van der Lee and Nolet, 1997) was modeled

86

using Rayleigh wave (S_V) data. SNA and NA95 should be identical for an isotropic Earth, but we see significant variations in the β_H/β_V ratio throughout the lid. This suggests that the Canadian shield model should be revisited with a consideration of radial anisotropy applied.

While the result for an isotropic inversion of anisotropic data is far from the true Earth structure, it can be used as rough guide to evaluate the presence and magnitude of anisotropy in the data. For an isotropic Earth the S_V and S_H models should be identical. When the S_H and S_V results are different, anisotropy is indicated. The isotropic result provides a good estimate of the magnitude and depth extent of anisotropy in the subsurface. This observation can then be used to create an initial model for an anisotropic inversion simultaneously solving for all 3 components of the data.

The Procedure

We began by separately inverting each of the 3 components of the data, using an isotropic assumption. Radial and vertical components were inverted for P and S_V structure. The tangential component was inverted for S_H structure. This was done from low frequency at low radial resolution (~ 100 km layers) to high frequencies with higher resolution (~ 25 km layers). The resulting models were compared and evaluated for the need for anisotropy. Once the need for anisotropy was apparent we inverted the 3-component data using an anisotropic assumption. This was again done starting at low frequency and ending at high frequency. In the anisotropic inversion, both seismic velocity and seismic anisotropy were inverted as a function of depth.

Since seismic models are not unique, we repeated the inversion several times at different starting points to get a series of 'best fit' model results. Figure 38 illustrates the results for the tangential component (S_H) data inversion. The synthetic seismograms for each of these models are virtually indistinguishable at the frequencies used, and each is an equally good fit to the data. The variations between the models provide a sense of the resolution of the data set. The solid line in the figure is the final result. It is a smoothed version of the series of inversion runs produced by averaging. The synthetics from the final result are also an equally good match to the data. Note that the model variations are in the range of <1% for any individual layer and much less overall, and that the basic structure, such as the location of
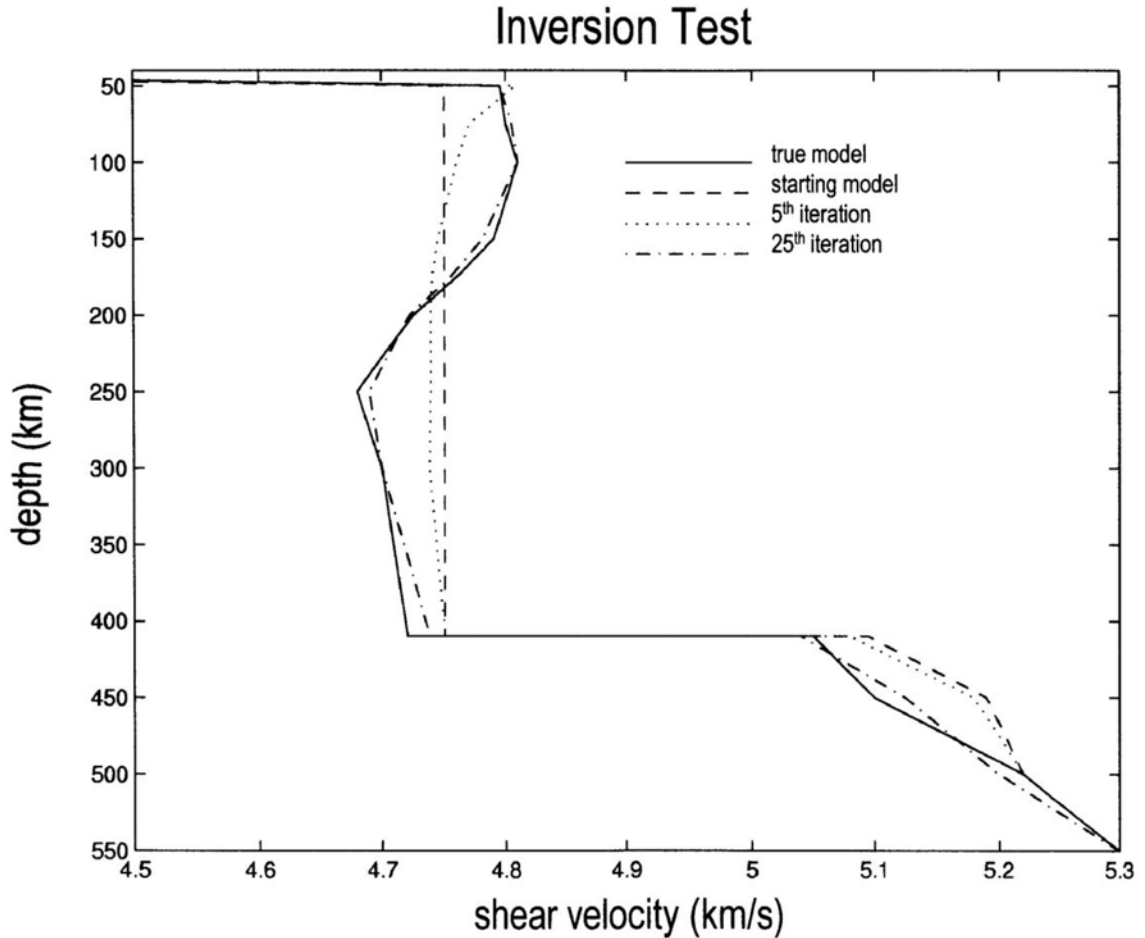
Inversion Test

Figure 36. A test of the waveform inversion procedure. Synthetic seismograms were created for an isotropic S_H velocity model (solid line) and used as the data in an inversion test. The inversion was begun using a simple starting model with uniform velocity from the Moho down to the 410 km discontinuity (dashed line). Surface waves dominate the misfit function until the shallowest structure is matched and after 5 iterations the inversion has matched only the top of the model (dotted line). Once the surface waves are fit, body wave arrivals dominate the misfit function and deeper structure is progressively better resolved. After 25 iterations (dashed -dotted line) the inversion has matched most of the structure in the model space.
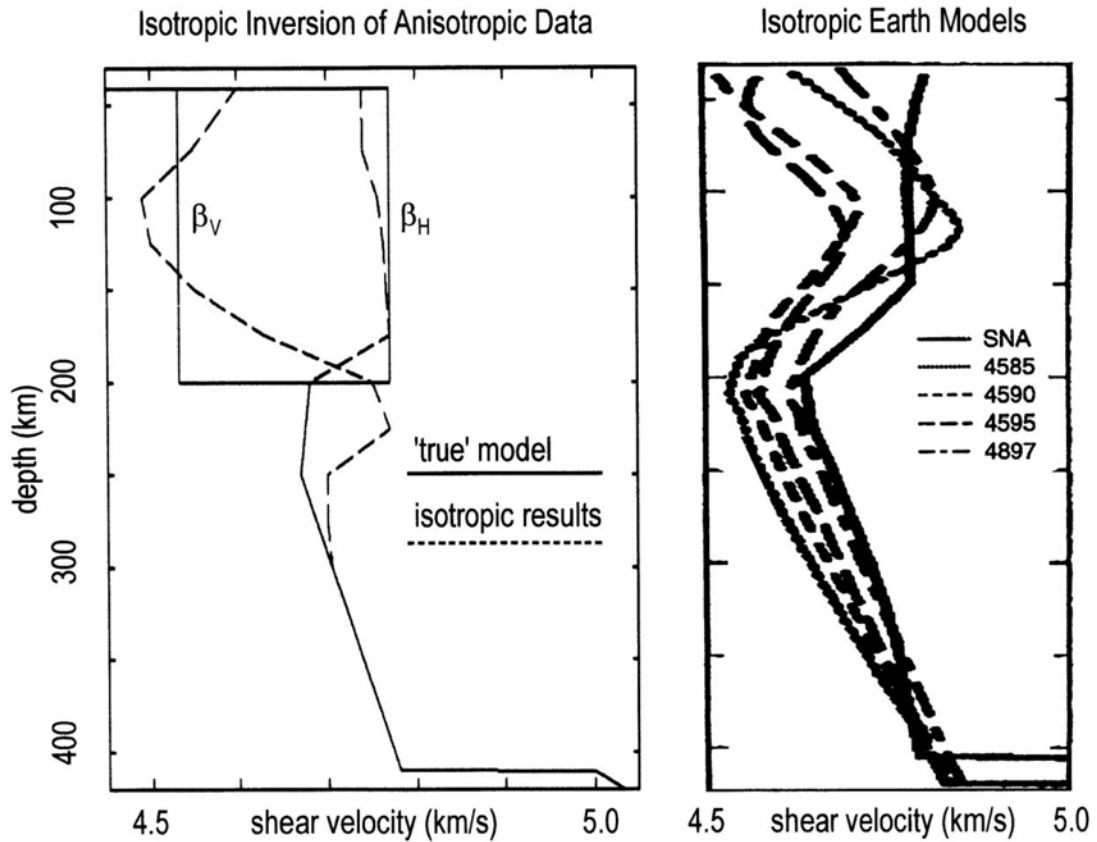
Figure 37. (Left) Inversion of anisotropic data using an isotropic assumption. 3 component synthetic seismograms were created for a 5% radially anisotropic model ($\beta_V < \beta_H$) (solid lines). These were used as data in separate inversions of β_H and β_V using an isotropic assumption. The results of the inversion are shown (dashed line). (Right) Isotropic earth models for the North American shield (from van der Lee and Nolet, 1997). SNA (Grand and Helmberger, 1984) was derived from tangential component body wave data. The other models were derived from Rayleigh wave data.

89

inversion results

depth (km) — shear velocity (km/s)
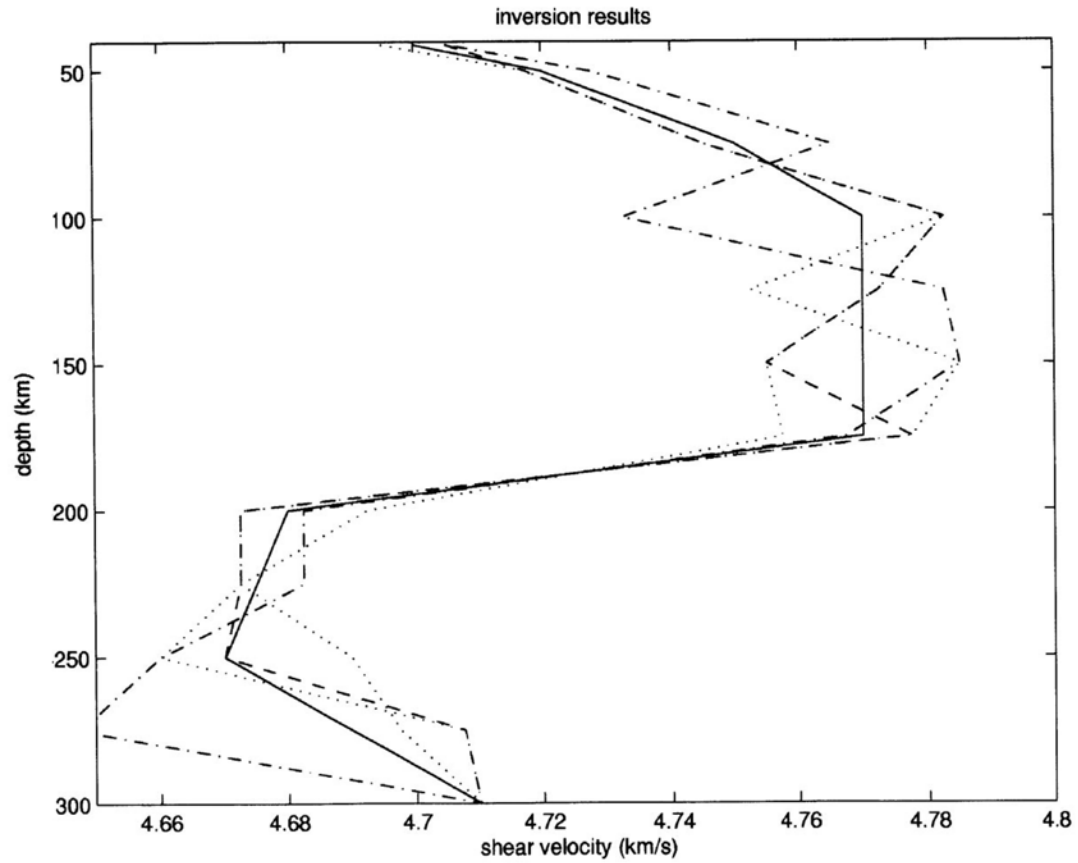
Figure 38. A series of inversion results for the East European platform data set (dashed lines). The inversion was run several times using different starting models. The final result (solid line) is a smoothed version produced by averaging the inversion runs. Synthetic seismograms for all of these models are virtually indistinguishable at the frequencies used in the study.

the low velocity zone, is consistent in all the results.

The Model

The crustal structure for the East European platform is taken as a multiple layer structure based on the CRUST5.1 model (Mooney 1998) extending to a depth of 41 km. The seismic structure below the crust down to 410 km depth was determined using three-component waveforms of body and surface wave arrivals from events located on the southern border of the craton. While the sources were located outside the platform, most of the source-receiver path length of each seismogram is within it and the final model should be a good estimate of the average upper mantle seismic structure for the craton. The fundamental mode surface wave data provide excellent resolution of the seismic structure down to about 150 km and body wave arrivals were used to constrain the velocity model below that. Our data is very sensitive to shear structure including shear anisotropy and to the horizontal component of P velocity (α_H). η and α_V are less well resolved by this data set.

The starting and final models are shown in figure 39. The initial model was a simple isotropic model with uniform P and S velocity from the Moho to 100 km depth. The final model is a radially anisotropic model with a distinct upper mantle lid over a LVZ (table 2). A dramatic improvement in the S_H, S_V and P data-synthetic match is seen along virtually all the source-receiver paths. This is illustrated by comparing the cross-correlation for the full waveform data of each seismogram for both the initial and final models (figure 40). Synthetics are compared to data profiles in figure 41. The model is characterized by a radially anisotropic seismic lid extending to a depth of 200 km with a largely isotropic mantle below. P structure mimics the S_H velocity structure with a high velocity lid extending to 200 km, a drop in seismic velocity followed by a positive velocity gradient down to 410 km. Our model has a positive velocity gradient from 41 km to 100 km depth, and a relatively uniform velocity structure from 100 km to 200 km depth with high S_H and P_H velocities (4.77 km /s, 8.45 km/s). β_H from 41 km to 200 km is uniformly 5% faster than β_V. From 200 to 250 km β_H drops to 4.70 km/s combined with a reduction in the shear anisotropy to 2%. Note that the mean shear velocity ($(\beta_H+\beta_V)/2$), is uniform (4.65 km/s) from 100 to 250 km depth and that the structure at the base of the lid is due to a reduction in the shear anisotropy below 200 km.
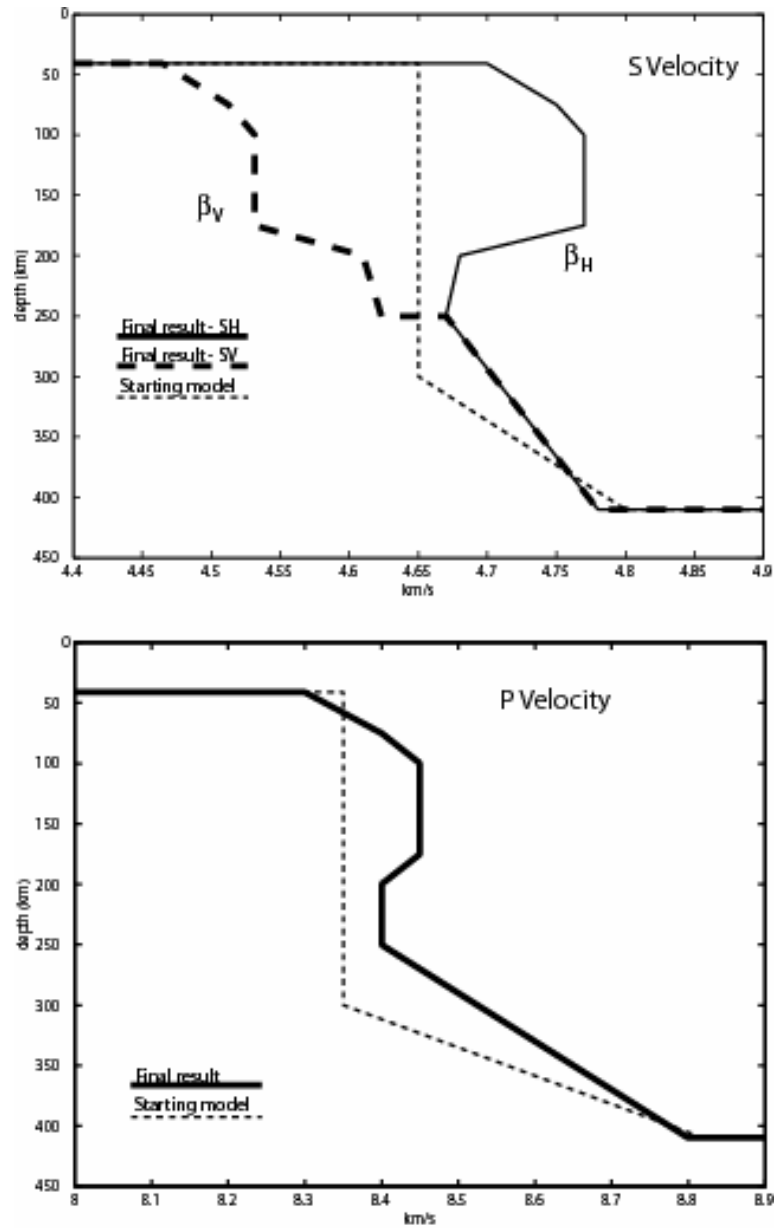
Figure 39. The starting and final models for the East European platform data set. The inversion was begun with an isotropic earth model with a homogeneous velocity structure from the Moho to 300 km. Shear wave radial anisotropy ($\beta_V < \beta_H$) is required to match the data. P anisotropy is unresolved.
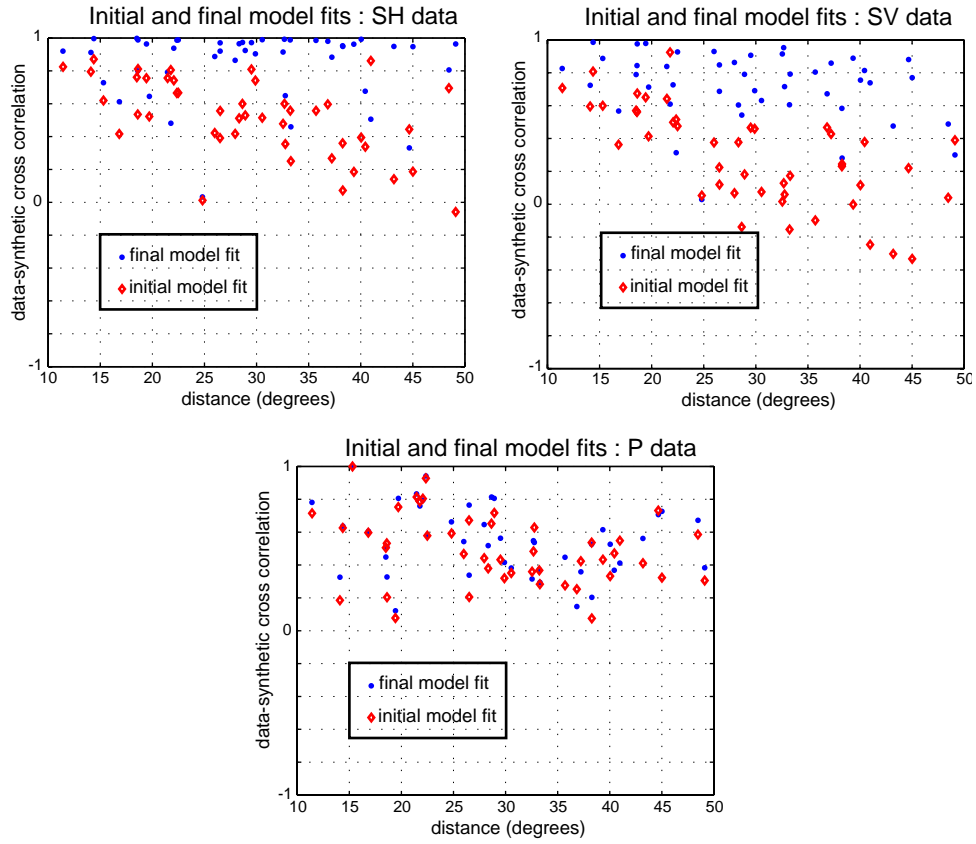
Figure 40. The cross-correlation between data and model synthetics for the initial (diamonds) and final (circles) models. The tangential component, S_H (top), and radial component, S_V (middle) correlation windows included phases from the first S arrival through the fundamental mode surface waves. The vertical component, P (bottom) correlation window included only phases between the direct and multiple P arrivals. The frequency band was between $0.01 - 0.05$ Hz.
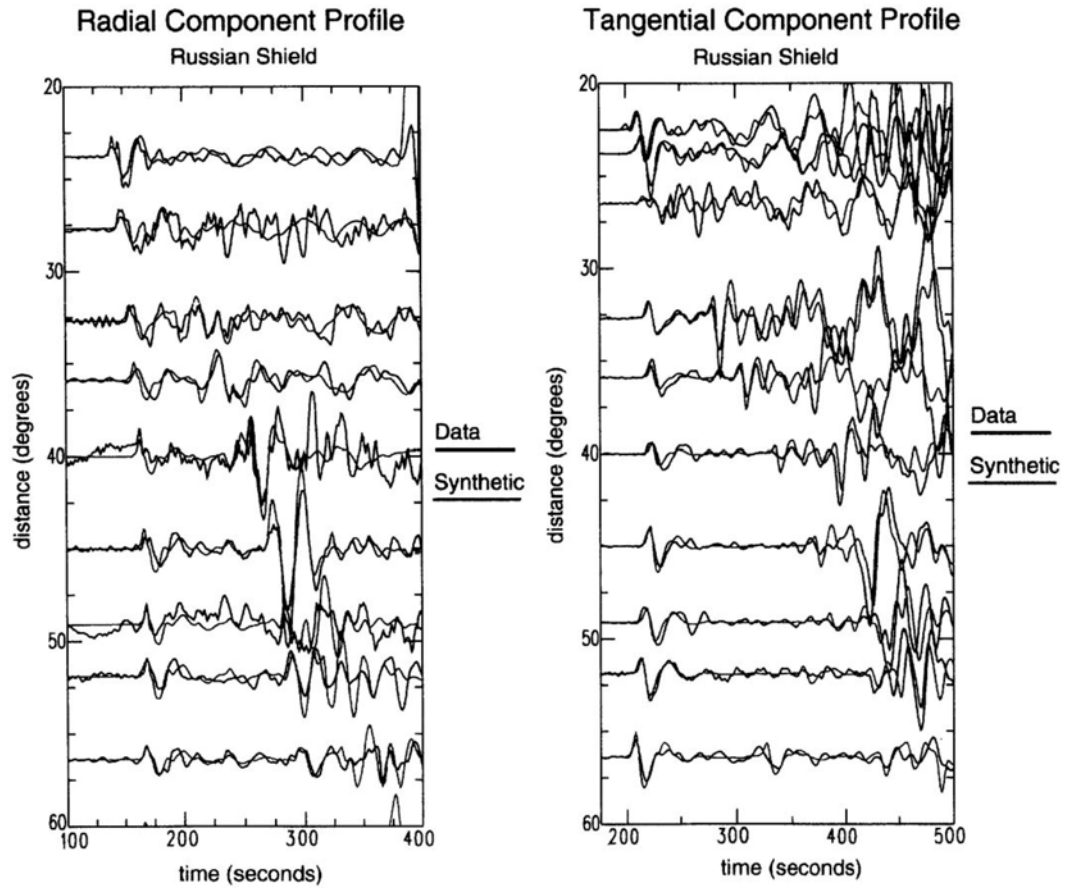
Figure 41. The radial and tangential component data profiles compared to the final model synthetics for a corridor that passes through the Russian shield (low-pass filtered with a corner frequency at 100 mHz). The direct P phase is the first arrival on the radial component, aligned just after the 150 second mark. The direct S phase is the first arrival on the tangential component aligned just after the 200 second mark.

Below 250 km the mantle is largely isotropic (less than 1% shear anisotropy) with a positive velocity gradient down to 410 km.

Resolution Tests

In order to properly interpret our model we wish to determine how well resolved our final model is. In particular, how well constrained is the location and magnitude of anisotropy? Is there definite evidence for a LVZ underlying a fast mantle lid and how well constrained is the lid thickness? To answer these questions we performed a series of resolution tests on our final model, comparing the individual cross-correlation fits for each of our seismograms to determine whether different perturbations to the model might improve the fit along certain paths. Figures 42 and 43 illustrate the sensitivity of the data to the shear velocity in the lid. We tested models in which the high velocity S_H lid extends between 100 and 300 km deep. As shown in figure 42, The fundamental mode Love waves provide excellent resolution down to ~200 km and indicate that the lid must extend at least that deeply in order to match the majority of the data. A few traces, particularly at source-receiver offsets under 15° show marginally better fits for thinner lids, probably because they incorporate proportionately more of the younger tectonic structures along their path lengths. In order to resolve the deeper structure we focus in on the body wave arrivals (S, SS) (figure 43). Here we've plotted correlations for models with a 4.77 km/s lid extending to 200, 250, and 300 km. Paths greater than 25° have the best resolution because the SS arrivals begin to be emerge and can be used as a tighter constraint on the model structure. Again, a model with a 200 km thick lid overlying a LVZ gives the best overall results, and models with lids extending below 250 km become conspicuously poorer.

Shear anisotropy was evaluated by comparing the data to radial and vertical component synthetics for the final model and perturbations from it. We tested both the depth extent and the magnitude of radial anisotropy in the platform. For these tests we kept the S_H velocity fixed and varied S_V with respect to that. Figure 44 compares Rayleigh waveform data to synthetics for models with an isotropic, 3%, 5% and 7% uniform anisotropy extending throughout the lid to 200 km. Notice the dramatic differences in the fit of the fundamental mode Rayleigh waves. The Love wave synthetics for each of these models (not shown) are

nearly identical to one another so the difference between the isotropic Rayleigh wave synthetic and the data (top of the figure) is equivalent to the Love-Rayleigh mismatch. Note that the higher mode body wave arrivals are also affected by the presence of anisotropy. We determined that models with a uniform 5% radial anisotropy provide the best data-synthetic matches, although models with anisotropic structures varying between 4% and 6% could not be excluded.

In addition to the magnitude of the anisotropy present, we also wanted to determine the location and extent of the anisotropic layer. The observed delays in the fundamental mode Rayleigh wave dictate that anisotropy must be present down to 100 km and perhaps deeper. In figure 45, we compare the radial component data-synthetic cross-correlation for 3 models: an isotropic model, a model with anisotropy extending to 100 km depth and our best fit model with anisotropy extending to 200 km depth. The full waveform from the direct S arrival through the fundamental mode Rayleigh wave were included in the correlation window. The results show strong evidence that radial anisotropy extends to at least 200 km depth – equivalent to depth of our high S_H velocity mantle lid. We focus on the body wave arrivals to determine whether anisotropy extends deeper than that. In figure 46, two radial component seismic traces are compared to synthetics for models with 0% and 5% anisotropy below 200 km. Notice that a delay of several seconds can occur if significant anisotropy is present. By comparing the results for all of the data (figure 47), we conclude that there is little anisotropy (<1%) below the seismic lid. Note in that in the figure there is significant scatter in the correlations from trace to trace. This is in part due to the amount of noise present in the data as well as the fact that the arrivals we are looking at are relatively small. Some individual traces appear to be better fit by models with significant anisotropy down to 400 km, but this is often caused by the delay time matching up with trailing phases. Overall the model with anisotropy confined to the mantle lid gives the best fit result.

In contrast to our resolution of S anisotropy, P anisotropy is difficult to resolve. Unlike shear anisotropy, a large number of paths, covering a wide range of incidence angles, is typically required to discriminate between α_h and α_v. These paths will necessarily sample different structure and a different range of depths and there will always be a tradeoff between anisotropic structure and radial structure in the final model. Anderson and Dziewonski (1982) showed that Rayleigh waves are sensitive to P anisotropy and η, however they are both much

less sensitive than S anisotropy and any errors in that measurement could be mapped into the P result. Furthermore, the effect of an increase in P anisotropy on the S_V arrivals is identical to that of a decrease in parameter η, and neither are individually resolvable.

We tested the sensitivity of our data to P anisotropy by calculating differential synthetic seismograms for the final P model (Figure 48). A large signal is seen in the α_H differentials, while very little signal is seen on the α_V differentials, indicating that variations in α_V have very little effect on the seismograms. The synthetics for an isotropic P model are virtually identical to the synthetics for an anisotropic P model if α_H equals α in the isotropic model. The similarity of these seismograms together with the results of the differential tests indicates that our P data are most sensitive to the horizontal component of P anisotropy.

Comparison with other cratonic models

One of our objectives is to compare our results for the East European platform to seismic models of other cratons to evaluate features common to all of them. Our results for the East European platform agree very closely with studies of the Australian (Gaherty et al., 1999; Simons et al., 1999), Kaapvaal (Jordan et al., 1999; Priestley, 1999; Qiu et al 1996), Tanzanian (Ritsema et al., 1998), Antarctic (Roult et al., 1994) and Canadian (Bostock, 1997; Grand and Helmberger, 1984) cratons and with the average seismic structure of Precambrian cratons (Ekstrom and Dziewonski, 1998). Each of these models is characterized by a high velocity seismic lid extending down to between 200 and 250 km depth, coincident with the location of maximum lateral heterogeneity seen in global models of the mantle. This depth also appears to be the base of the petrological lithosphere based on studies of mantle xenoliths. Kopylova et al. (1998), for example, identified a depth of 190 km as the base of the petrological lithosphere beneath the Slave craton in Canada based on the apparent source region for both porphyroclastic peridotite and other texturally unequilibrated magmatic rocks. This is consistent with a major seismic discontinuity beneath the Slave craton identified at 195 km depth by Bostock (1997).
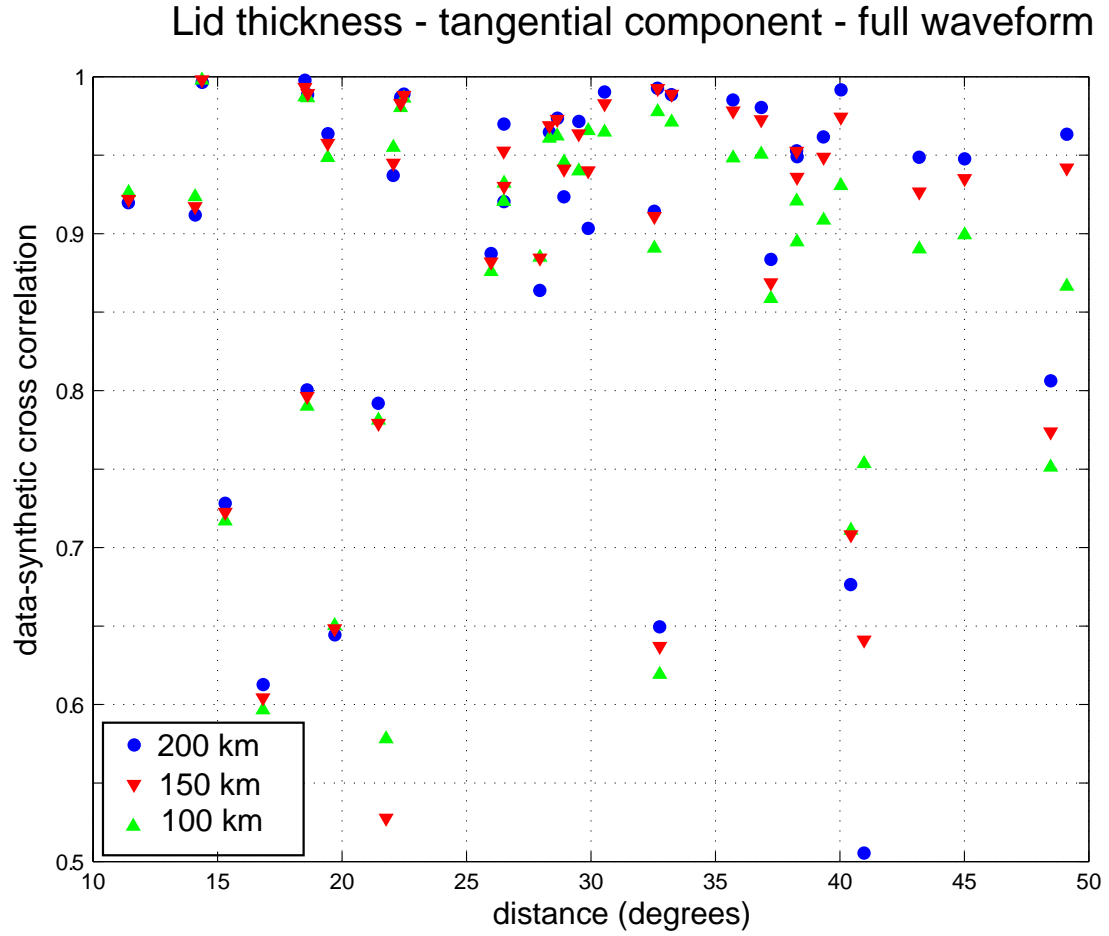
Figure 42. A test of the thickness of the seismic lid, focusing on surface waves. The cross correlations between tangential component data and synthetic seismograms for models with lids extending to 100 (open triangles), 150 (filled triangles), and 200 km depth (circles), respectively.
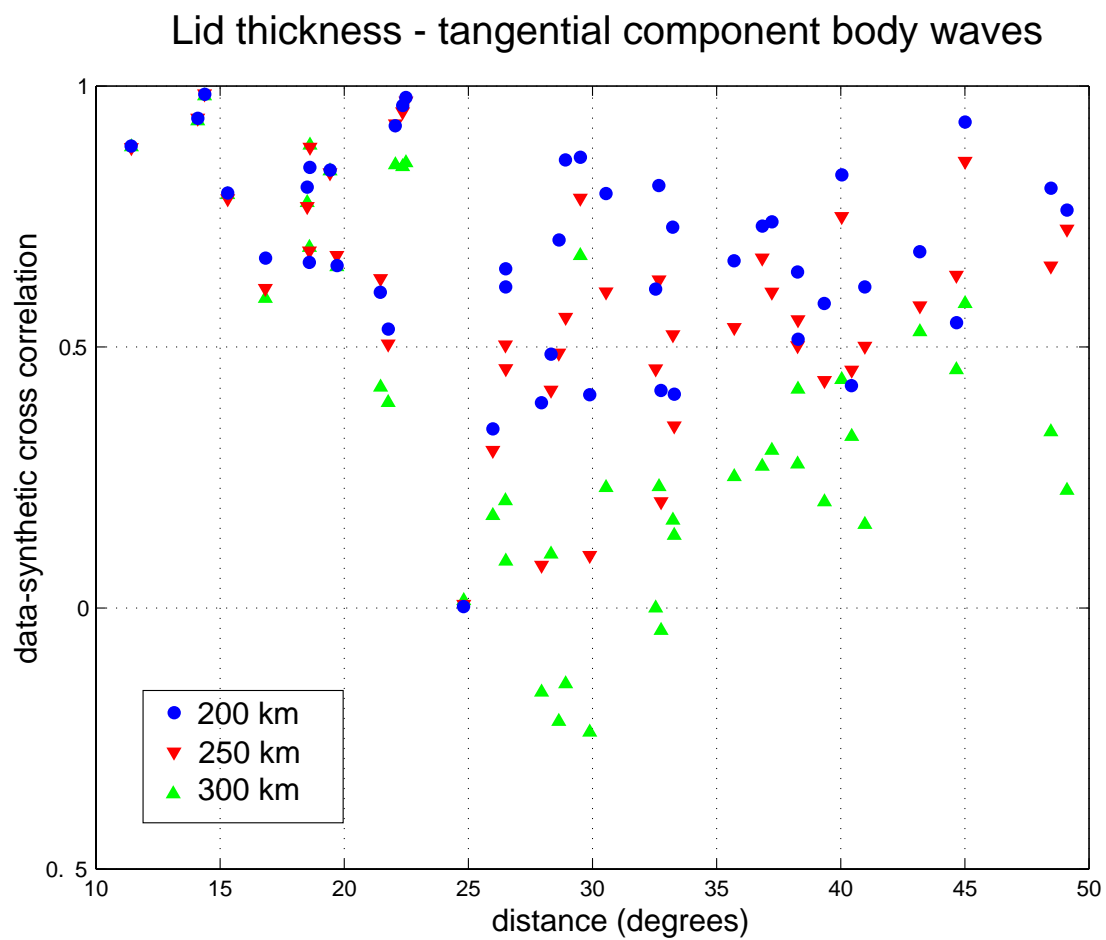
Figure 43. A test of the thickness of the seismic lid, focusing on body waves. The cross correlations between tangential component data and synthetic seismograms for models with lids extending to 200 (circles), 250 (filled triangles) and 300 km (open triangles), respectively.
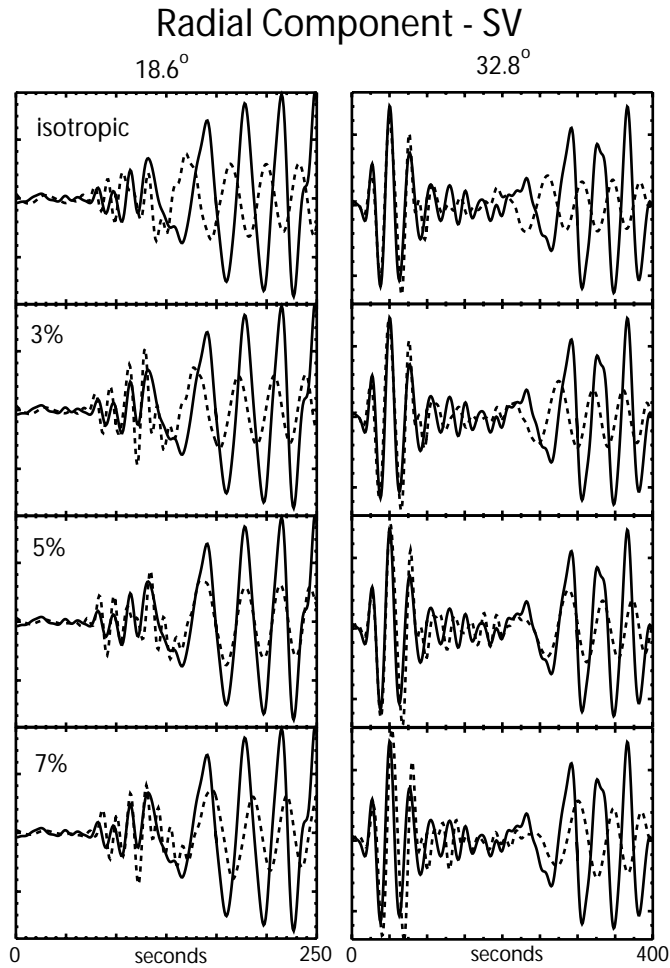
Figure 44. Evidence for anisotropy in the mantle lid: radial component synthetics for isotropic and radially anisotropic models (dashed) are compared with data (black) for two of the stations used in this study. The first arrival is the direct S wave, SS and Rayleigh waves are also evident. Synthetics were calculated using a constant S_H model and anisotropy was calculated relative to that. The top traces are for isotropic models, below that are traces for models with 3%, 5% and 7% radial anisotropy ($\beta_V < \beta_H$). In these models the anisotropy is uniform throughout the lid. Below the lid the models are isotropic.
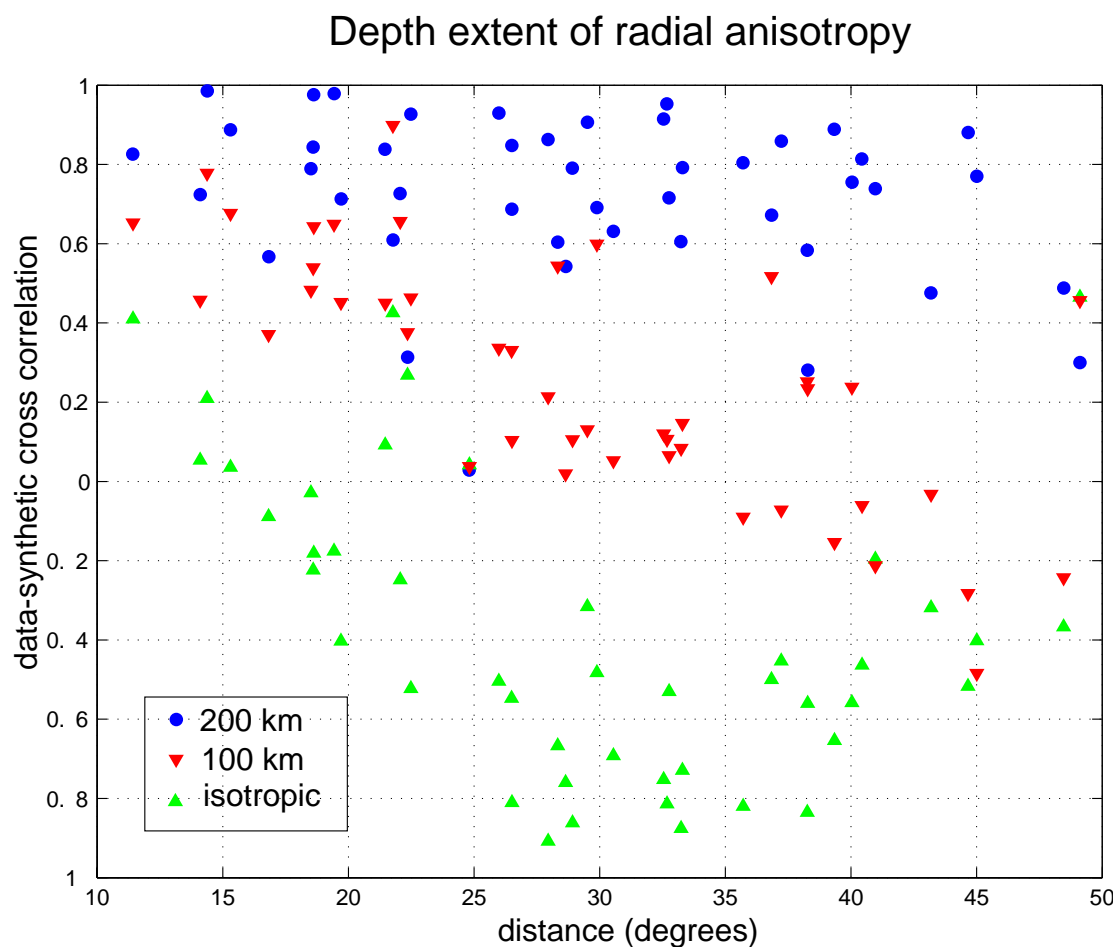
Figure 45. A test of the depth extent of radial anisotropy, focusing on Rayleigh waves. The cross correlations between radial component data and synthetic seismograms for an isotropic model (open triangles) and models with 5% anisotropy extending to 100 (filled triangles), and 200 km (circles).

.
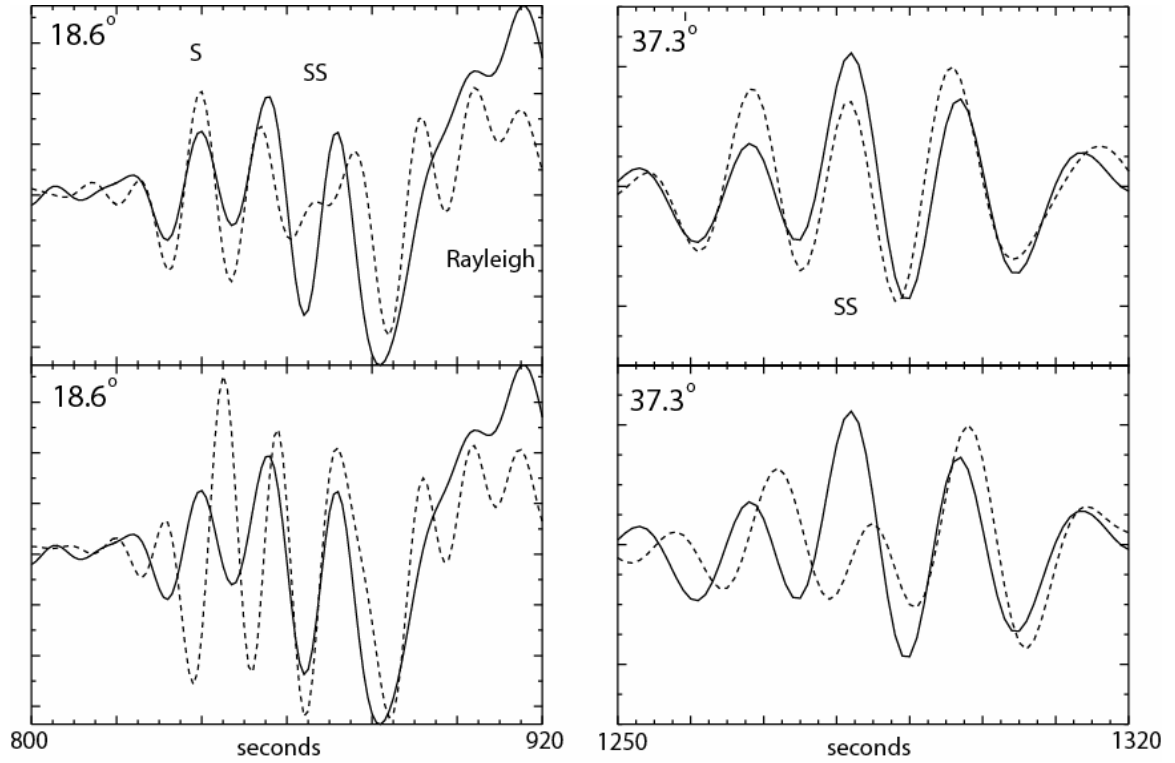
Figure 46. Radial component synthetics for anisotropic models (dashed) are compared to data (black) focusing on body wave arrivals. Synthetics were calculated using a constant S_H model and anisotropy was calculated relative to that. In the top panels, 5% radial anisotropy is included from the Moho to 200 km depth, with isotropic structure below. In the bottom panels, the anisotropy extends to 410 km.
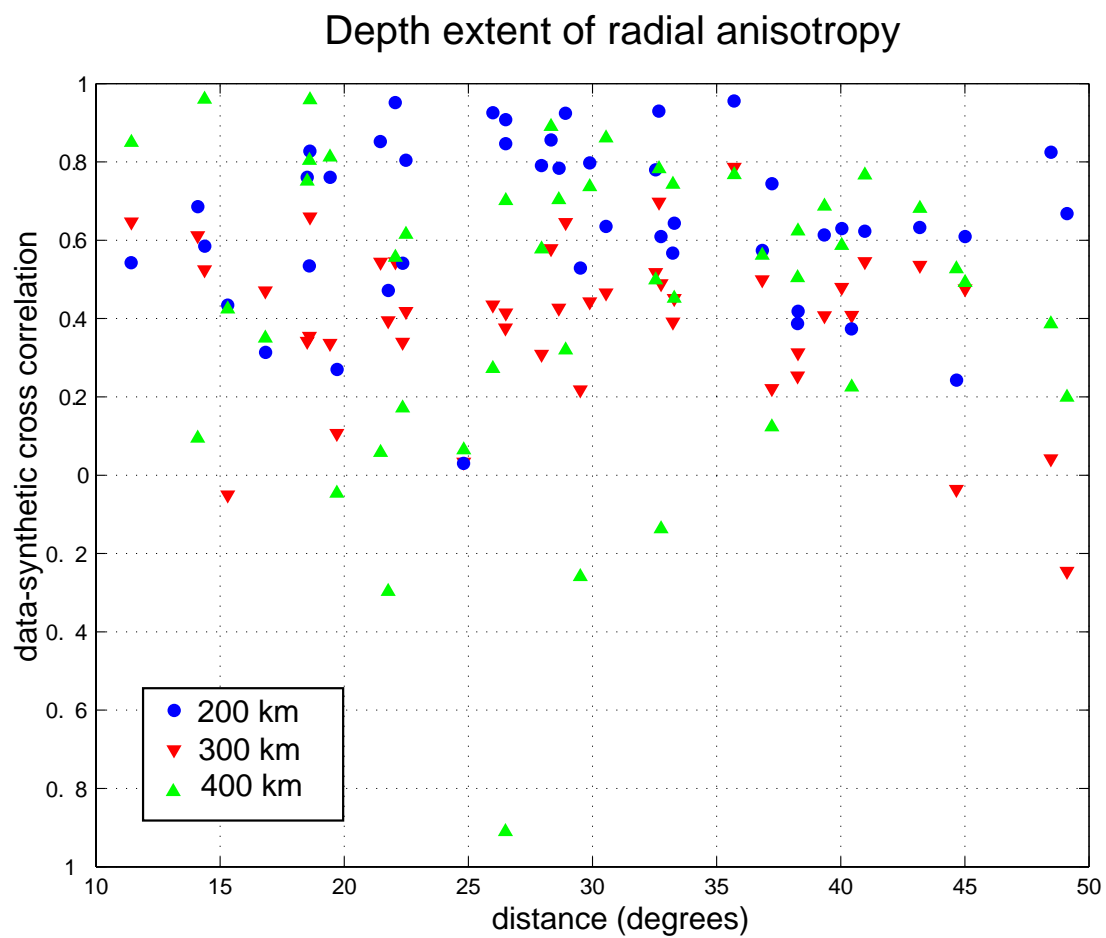
Figure 47. A test of the depth extent of radial anisotropy, focusing on body waves. The cross correlations between radial component data and synthetic seismograms for models with 5% anisotropy extending to 200 km (circles), 300 km (filled triangles) and 400 km (open triangles).
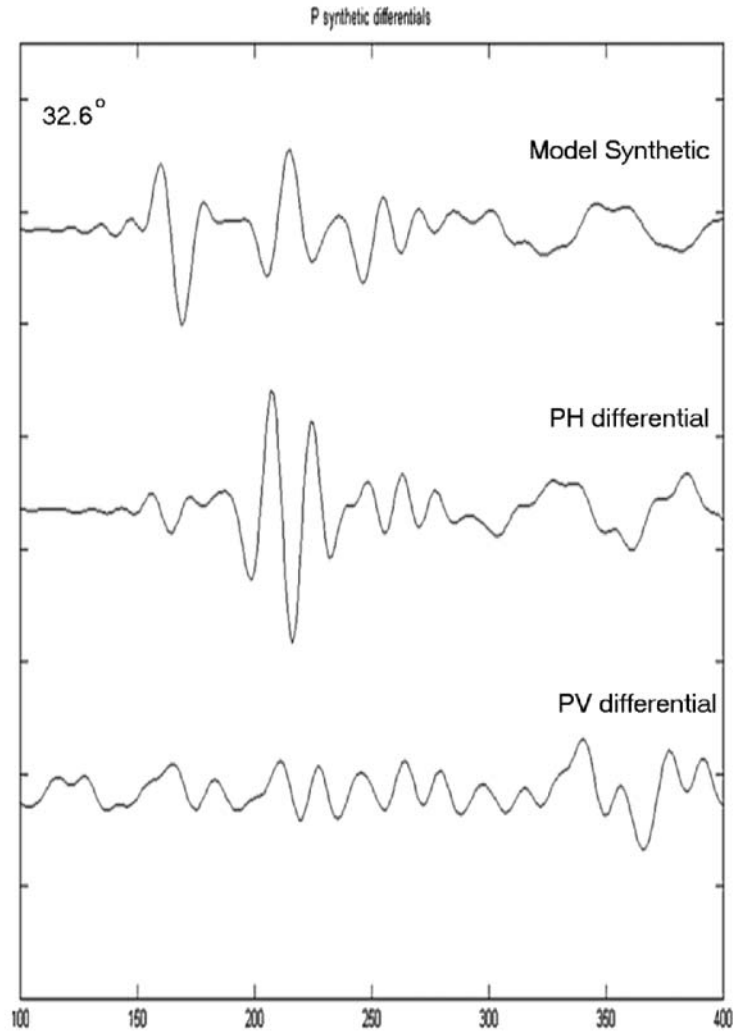
Figure 48. Sensitivity to P anisotropy: Vertical component synthetics and differentials focusing on the P arrival. The top trace is the synthetic for an anisotropic P model ($\alpha_V < \alpha_H$). The middle and bottom traces are differentials for that model with small perturbations in α_H and α_V respectively. A large signal is seen in the α_H differentials, while very little signal is seen on the α_V differentials, indicating that variations in α_V have very little effect on the seismograms.

Anisotropy also appears to be a characteristic of the seismic lid. Our final model includes a uniform 5% shear anisotropy in the mantle lid down to 200 km. No significant variation in the magnitude or gradient of anisotropy is present throughout the lid except at the very base of the lid 200 - 250 km. Below 250 km no measurable amount of anisotropy (less than 1%) is present Similarly both the Australian and Kaapvaal cratons were found to have a uniform 4-5% shear anisotropy in the lid extending to 250 km depth with a sharp transition to an isotropic mantle regime below that. Significantly, however, the results of the NARS profile through the east European continent identified large shear anisotropy (7%) beneath the Mediterranean, but no clear pattern in shear anisotropy beneath the EEP (Muyzert et al., 1999).

The similarity of the velocity structure, lid thickness, and distribution of anisotropy of these cratonic models points to a common mechanism for the formation and evolution of continental cratons globally. Our results support the conclusions of Gaherty and Jordan (1995) that 200 km beneath cratons is either an interface between an anisotropic lithosphere and a more dynamically active regime or is the location of a change in deformation from dislocation to diffusion creep (Karato, 1992). The Pn waveguide model (Ryberg et al., 1995) consisting of horizontally elongated scatterers could also produce anisotropic wave propagation, but their limit of 100 km as the maximum depth of the waveguide is too thin to account for all our observations.

Conclusions

The East European platform is underlain by a radially anisotropic seismic mantle lid extending to a depth of 200 km with a largely isotropic mantle below. The model has a positive velocity gradient from 41 km to 100 km depth, and a relatively uniform velocity structure from 100 km to 200 km depth with high S_H and P_H velocities (4.77 km /s, 8.45 km/s). Shear anisotropy is uniform at 5% ($\beta_H > \beta_V$) from 41 to 200 km depth, drops to 2% from 200 to 250 km and is isotropic below that. The average shear velocity from 100 to 250 km is also uniform at 4.65 km/s and the drop in anisotropy is matched by a drop in β_H to 4.70 km/s combined with an increase in β_V to 4.60 km/s. Below 250 km there is a positive velocity gradient in both P and S velocity down to 410 km. P anisotropy is not well resolved,

but P structure mimics the S_H velocity structure, suggesting that P is also anisotropic within the lid.

Comparison between this and other cratonic models allows us to make the following conclusions:

- Continental cratons have very similar seismic structure with a high velocity seismic lid with 4-5% shear anisotropy.
- The mantle beneath the lid is isotropic.
- Since anisotropy is concentrated at the top of the mantle and is uniform in magnitude it is likely a vestige of past tectonic activity.
- Seismic anisotropy is a characteristic of the mantle lithosphere and the cutoff depth between anisotropic and isotropic regimes may be a measure of the base of the petrologic lithosphere.
- The base of the lithosphere beneath cratons appears to be at 200-250 km based on the cutoff of seismic anisotropy and the correlation with thermobarometric data from mantle xenoliths.
- Seismic lids present below continental cratons appear to be an artifact of seismic anisotropy and isotropic models should be revisited with this understanding in mind.

References

Anderson, D. L., *Theory of the Earth*, Blackwell Sci. Publ., 1989.

Anderson, D. L., and Dziewonski, A. M., Upper mantle anisotropy – evidence from free oscillations, *Geophys. J. R. astr. Soc.*, 69, 383-404, 1982

Artyushkov, E. V., On the origin of the seismic anisotropy of the lithosphere, *Geophys. J. R. astr. Soc.*, 76, 173-178, 1984.

Backus, G. E., Long-wave elastic anisotropy produced by horizontal layering, *J. Geophys. Res.*, 67, 4427-4440, 1962.

Bostock, M. G., Anisotropic upper-mantle stratigraphy and architecture of the Slave craton, *Nature*, 390, 392-395, 1997.

Ekstrom, G. and Dziewonski, A. M., The unique anisotropy of the Pacific upper mantle, *Nature*, 168-172, 1998.

Fuchs, K. and G. Muller, Computation of synthetic seismograms with the reflectivity method and comparison with observations, *Geophys. J. R. Astron. Soc.*, 23, 417-433, 1971.

Gaherty, J. B., and Jordan, T. H., Lehmann discontinuity as the base of an anisotropic layer beneath continents, *Science*, 268, 1468-1471, 1995.

Gaherty, J. B., Kato, M., and Jordan, T. H., Seismological structure of the upper mantle: a regional comparison of seismic layering, *Phys. Earth Planet. Inter.*, 110, 21-41, 1999.

Gauthier, O., Virieux, J., Tarantola, A., Two-dimensional nonlinear inversion of seismic waveforms: Numerical results, *Geophysics*, 51, 7, 1387-1403, 1986.

Given, J. W. and Helmberger, D. V., Upper mantle structure of northwestern Eurasia, *J. Geophys. Res.*, 85, 7183-7194, 1980.

Glebovitsky, V. A., *The Early Precambrian of Russia*, Harwood Academic Publishers, 1997.

Grand, S. P. and Helmberger, D. V., Upper mantle shear structure of North America, *Geophys. J. R. Astron. Soc.*, 76, 399-438, 1984.

Jordan, T. H., Structure and formation of the continental tectosphere, *Journal of Petrology*, Special Lithosphere Issue, 11-37, 1988.

Jordan, T. H., Saltzer, R. L., Gaherty, J. B., Small-scale anisotropic heterogeneity in the continental upper mantle, *Seismological Research Letters*, 70 (2), 259-260, 1999.

Karato, S., On the Lehmann discontinuity, *Geophys. Res. Letts.*, 19, 22, 2255-2258, 1992.

Kern, H. P and S wave anisotropy and shear wave splitting at pressure and temperature in possible mantle rocks and their relationship to the rock fabric, *Phys. Earth Planet. Inter.*, 87, 245-256, 1993.

Kopylova, M. G., Russell, J.K. and Cookenboo, H., Upper mantle stratigraphy of the Slave craton, Canada: Insights into a new kimberlite province, *Geology*, 26, 4, 315-318, 1998 .

LeFevre, L. V. and Helmberger, D. V., Upper mantle P velocity structure of the Canadian shield, *J. Geophys. Res.*, 94, 17749-17765, 1989.

Li, A., Fischer, K. M., Wysession, M. E. and Clarke, T. J., Mantle discontinuities and temperature under the north American continental keel, *Nature*, 395, 160-163, 1998.

Marquering, H. and Snieder, R., Shear-wave velocity structure beneath Europe, the northeastern Atlantic and western Asia from waveform inversions including surface-wave mode coupling, *Geophys. J. Int.*, 127, 283-304,1996

Montagner, J.-P., and Kennett, B. L. N., How to reconcile body wave and normal mode reference earth models, *Geophys. J. Int.*, 125, 229-248, 1996.

Montagner, J.-P., Tanimoto, T., Global upper mantle tomography of anisotropy of seismic velocities and anisotropies, *J. Geophys. Res.*, 96, 20,337-20,351, 1991.

Mooney, W. D., Laske, G., Masters, T. G., CRUST 5.1; a global crustal model at 5 degrees X5 degrees, *J. Geophys. Res.*, 103, 727-747, 1998.

Mora, P. Elastic wave-field inversion of reflection and transmission data, *Geophysics*, 53, 6, 750-759, 1988.

Muyzert E, Paulssen H, Snieder R, A seismic cross-section through the east European continent, *Geophys. J. Int.*, 136, 695-704, 1999

Nicolas, A. and Christensen, N. I., Formation of anisotropy in upper mantle peridotites: A review, Composition, *Structure and Dynamics of the Lithosphere-Asthenosphere System*, 111-123, 1987.

O'Reilly, S. Y., Griffin, W. L., 4-D Lithosphere Mapping: methodology and examples, *Tectonophysics*, 262, 3-18, 1996.

Paulssen, H., Bukchin, B. G., Emelianov, A. P., Lazarenko, M., Muyzert, E., Snieder, R., Yanovskaya, T. B., The NARS-DEEP project, *Tectonophysics*, 313, 1-8, 1999

Pavlenkova, N. I., Pavlenkova, G. A. and Solodilov, L. N., High velocities in the uppermost mantle of the Siberian craton, *Tectonophysics*, 262, 51-65, 1996.

Pica, A., Diet, J. P., Tarantola, A., Nonlinear inversion of seismic reflection data in a laterally invariant medium, *Geophysics*, 55, 3, 284-292, 1990.

Priestley, K., Velocity structure of the continental upper mantle: evidence from southern Africa, *Lithos*, 48, 45-56, 1999

Qiu, X., Priestley, K., and McKenzie, D., Average lithospheric structure of southern Africa, *Geophys. J. Int.*, 127, 563-558, 1996.

Randall, G. E., Efficient calculation of complete differential seismograms for laterally homogeneous earth models, *Geophys. J. Int.*, 118, 245-254, 1994.

Regan, J. and D. J. Anderson, Anisotropic models of the upper mantle, *Phys. Earth Planet. Inter.*, 35, 227-263, 1984.

Ritsema, J., Nyblade, A. A., Owens, T. J., Langston, C. A., VanDecar, J. C., Upper mantle seismic velocity structure beneath Tanzania, East Africa; implications for the stability of cratonic lithosphere, *J. Geophys. Res.*, 103, 21,201-21,213, 1998.

Roult, G., Rouland, D. and Montagner, J. P., Antarctica II: Upper-mantle structure from velocities and anisotropy, *Phys. Earth Planet. Inter.*, 84, 33-57, 1994.

Ryberg, T., Fuchs, K., Egorkin, A. V. and Solodilov, L., Observations of high frequency teleseismic Pn on the long-range Quartz profile across northern Eurasia, *J. Geophys. Res.*, 100, 18,151-18,163, 1995.

Saltzer, R. L., Gaherty, J. B., Jordan, T. H., How are vertical shear wave splitting measurements affected by variations in the orientation of azimuthal anisotropy and depth?, *Geophys J. Int.*, 141 (2), 374-390, 2000.

Sen, M. and Stoffa, P. L., *Global optimization methods in geophysical inversion*, Elsevier, 1995.

Simons, F. J., Zielhuis, A. and van der Hilst, R. D., The deep structure of the Australian continent from surface wave tomography, *Lithos*, 48, 17-43, 1999

Tarantola, A., Linearized inversion of seismic reflection data, *Geophysical Prospecting*, 32, 998-1015, 1984.

van der Lee, S. and Nolet, G., Upper mantle S velocity structure of North America, *J. Geophys. Res.*, 102, 22,815-22,838, 1997.

Vinnik, L. P., Ryaboy, V. Z., Deep structure of the East European platform according to seismic data, *Phys Earth Planet. Inter.*, 25, 27-37, 1981

Vinnik, L. P., Green, R.W. E., Nicolaysen, L. O., Kosarev, G.L., Petersen, N. V., Deep seismic structure of the Kaapvaal craton, *Tectonophysics*, 262, 67-75, 1996.

Xu, Y. and Wiens, D., Upper mantle structure of the southwest Pacific from regional waveform inversion, *J. Geophys. Res.*, 102, 27,439-27,451, 1997.

Zhao, M., Langston, C. A., and Nyblade, A. A., and Owens, T. J., Upper mantle velocity structure beneath southern Africa from modeling regional seismic data, *J. Geophys. Res.*, 104, 4793-4794, 1999.

Zonenshain, L. P., Kuzmin, M. I. and Natapov, L. M., *Geology of the USSR: A plate-tectonic synthesis*, Geodynamics Series Volume 21, 1990.

Table 1. List of Sources and Receivers

event	latitude	longitude	depth
9/13/99	40.71^o	30.05^o	13 km

station	distance	azimuth
OBN	15.05^o	14.56^o
ARU	24.31^o	40.07^o
LVZ	27.36^o	3.79^o
KEV	28.94^o	357.79^o
KBS	39.00^o	354.53^o

event	latitude	longitude	depth
1/31/99	43.12^o	46.74^o	33 km

station	distance	azimuth
ARU	15.31^o	25.50^o
TRTE	19.70^o	327.71^o
KONO	27.95^o	319.22^o
KEV	28.32^o	345.54^o
KBS	38.27^o	349.77^o

event	latitude	longitude	depth
3/21/98	36.46°	70.00°	236 km

station	distance	azimuth
ARU	21.46°	342.29°
OBN	29.51°	319.91°
LVZ	37.23°	338.29°
KEV	40.45°	338.29°
KON	44.66°	321.10°
KBS	48.46°	347.36°

event	latitude	longitude	depth
3/21/98	79.84°	1.58°	10 km

station	distance	azimuth
KEV	11.43°	131.18°
LVZ	14.10°	122.89°
TRTE	22.06°	143.92°
SUW	25.99°	150.72°
OBN	26.51°	132.94°
ARU	28.92°	106.53°
KIEV	29.89°	144.15°
KIV	38.26°	130.38°
ANTO	40.97°	142.92°

event	latitude	longitude	depth
2/28/98	38.30^o	48.06^o	15 km

station	distance	azimuth
OBN	18.51^o	338.90^o
ARU	19.43^o	17.70^o
LVZ	30.55^o	350.08^o
KEV	33.24^o	346.70^o
KBS	43.19^o	350.44^o

event	latitude	longitude	depth
6/25/97	33.94^o	59.47^o	10 km

station	distance	azimuth
ARU	22.85^o	357.91^o
OBN	27.03^o	329.83^o
TRTE	33.30^o	328.26^o
LVZ	37.31^o	344.51^o
KEV	40.36^o	342.82^o
KBS	49.55^o	349.13^o

event	latitude	longitude	depth
2/04/97	37.82^o	57.50^o	15 km

station	distance	azimuth
ARU	18.62^o	1.84^o
OBN	22.35^o	327.38^o
TRTE	28.64^o	325.83^o
LVZ	32.68^o	344.24^o
KEV	35.70^o	342.23^o
KBS	45.01^o	348.78^o

event	latitude	longitude	depth
8/14/96	40.67^o	35.34^o	10 km

station	distance	azimuth
OBN	14.37^o	2.84^o
ARU	21.77^o	36.14^o
KBS	39.34^o	353.06^o

Table 2

Seismic model for the East European Platform

z (km)	α_H (km/s)	β_H (km/s)	β_V (km/s)	η
0	2.50	1.10	1.10	1
0.5	4.00	2.10	2.10	1
2.0	6.20	3.60	3.60	1
17.0	6.20	3.60	3.60	1
32.0	6.60	3.70	3.70	1
41.0	7.30	4.00	4.00	1
41.1	8.30	4.70	4.47	0.95
75.0	8.40	4.75	4.51	0.95
100.0	8.45	4.77	4.53	0.95
175.0	8.45	4.77	4.53	0.95
200.0	8.40	4.68	4.62	0.97
250.0	8.40	4.67	4.63	0.97
250.0	8.40	4.67	4.67	1
410.0	8.80	4.80	4.80	1

Appendix A
Calculating synthetic seismograms for radially anisotropic media

Backus (1962) demonstrated that a large subset of radially anisotropic models are long-wavelength equivalent to a series of thin isotropic layers in which the elastic constants vary rapidly. We have taken advantage of his work to create synthetic seismograms for radially anisotropic media using a reflectivity code that assumes isotropic layering. The procedure is first to determine if a given anisotropic model fits certain stability criteria and, if it does, to calculate the equivalent series of isotropic layers which are then written as an input model for the calculation.

A series of isotropic layers will appear, at long-wavelengths, to have the elastic constants of a radially anisotropic medium based on the averages of the isotropic elastic constants. Using Backus' notation these 5 elastic constants are:

$L = < 1/\mu >^{-1}$

$M = < \mu >$

$R = < \theta / \mu >$

$S = < \theta \mu >$

$T = < \theta >$

θ is the square of the ratio of shear to compressional velocity: $\theta = \mu / (\lambda + 2 \mu)$.

λ and μ are the Lame' parameters.

$<..>$ represents the average of the isotropic parameters in the series of layers, weighted by layer thickness.

These are related to the radially anisotropic elastic parameters (C_{11}, C_{33}, C_{44}, C_{66}, C_{13}) by:

$L = C_{44}$

$M = C_{66}$

$R = 1./C_{33}$

$S = (C_{13}^2 + 2 C_{66} C_{33} - C_{33} (C_{11} - 2C_{66}))/(4C_{33})$

117

$$T = (C_{33} - C_{13})/(2C_{33})$$

To obtain a layered equivalent to a radially anisotropic model, we input α_h, α_v, β_h, β_v, ρ, and η, calculate the C_{ij} and then L, M, R, S, T. Next, we verify the below inequalities and, if all are satisfied, calculate a multilayer model solution.

In general, a radially anisotropic medium is long-wavelength equivalent to a series of isotropic layers as long as the following stability criteria are met:

$$0 < R < 0.75 \, L^{-1} \quad (\sim 0 < <\beta^2> \ < \ <\alpha^2>)$$
$$0 < S < 0.75 \, M$$
$$0 < T < 0.75 \quad\quad (\sim \ 0 < <\beta^2/\alpha^2> < \ 0.75)$$
$$T^2 < R \, S$$
$$(0.75 - T)^2 < (0.75 \, L^{-1} - R) \, (0.75 \, M - S)$$

Backus further demonstrated that, as long as these conditions are met, a simple 2 or 3 layered medium is all that is required to match the equivalent radially anisotropic media. The two layered case falls into several subsets.

Set 1: $SM^{-1} < T < RL$

Set 2: $RL < T < SM^{-1}$

Sets 3 and 4

$RL = T = SM^{-1}$

Set 3: $L < M$ ($\beta_v < \beta_h$)

Set 4: $L = M$ ($\beta_v = \beta_h$)

Otherwise 3 layers are required.

If the stability criteria are met, we can solve directly to obtain the P and S velocities (α_i , β_i) and the relative thicknesses (p_i) of each layer (i) in the series. Summarizing the

relevant equations from Backus (33 - 37), we first solve for parameters μ_i and then input those results into equations for p_i and θ_i.

The sum of the layer series is normalized to 1.

$$\Sigma\ p_i = 1$$

For sets 1 and 2 we can solve uniquely for μ_i by solving the quadratic equation:

$$a\ \mu^2 + b\ \mu + c = 0$$

$a = (R\ L - T)$
$b = -(R\ L\ M - S)$
$c = L\ (M\ T - S)$
$sbac = \sqrt{(\ b^2 - 4\ a\ c\ )}$

$\mu_1 = (-b - sbac)/(2\ a)$
$\mu_2 = (-b + sbac)/(2\ a)$

$p_1 = (\mu_2 - M)/(\mu_2 - \mu_1)$
$p_2 = (M - \mu_1)/(\mu_2 - \mu_1)$

$\theta_1 = (T\ \mu_2 - S)/(\mu_2 - M)$
$\theta_2 = (S - T\ \mu_1)/(M - \mu_1)$

for set 3, solutions for μ_i are not unique, but can be any solution of:

$$\mu_1 + \mu_2 = M + L^{-1}\ (\mu_1\ \mu_2)$$

and p_i and θ_i are solved as above.

for set 4,

$$\mu_1 = \mu_2 = M$$

and p_i and θ_i are any solutions of

$$p_1 + p_2 = 1$$
$$p_1\theta_1 + p_2\theta_2 = T$$

For the 3-layered case, we set the values of p_3, μ_3 and θ_3, then solve for layer 1 and layer 2. Modifying L, M, R, S ,T:

$$I_b = 1 - p_3$$
$$M_b = M - p_3\,\mu_3$$
$$L_b = (L^{-1} - p_3/\mu_3)^{-1}$$
$$T_b = T - p_3\theta_3$$
$$S_b = S - p_3\,\theta_3\,\mu_3$$
$$R_b = R - p_3\,\theta_3/\mu_3$$

The quadratic equation now becomes:

$$a\,\mu^2 + b\,\mu + c = 0$$

$$a = (R_b\,I_b\,L_b - T_b)$$
$$b = -(R_b\,L_b\,M_b - S_b)$$
$$c = L_b\,(M_b\,T_b - S_b\,I_b)$$
$$sbac = \sqrt{(b^2 - 4\,a\,c)}$$

$$\mu1 = (-b - sbac)/(2\,a)$$
$$\mu2 = (-b + sbac)/(2\,a)$$

$$p_1 = (I_b\,\mu_2 - M_b)/(\mu_2 - \mu_1)$$

$$p_2 = (M_b - I_b\,\mu_1)/(\mu_2 - \mu_1)$$

$$\theta_1 = (T_b\,\mu_2 - S_b)/(I_b\,\mu_2 - M_b)$$

$$\theta_2 = (S_b - T_b\,\mu_1)/(M_b - I_b\,\mu_1)$$

The densities (ρ_i) and therefore the final velocities (α_i, β_i) are free variables. For simplicity, I select ρ_i to be constant throughout the layer series, but this is not required. Once the ρ_i are selected, the P and S velocities for each layer are:

$$\alpha_i = \sqrt{(\mu_i/(\theta_i\,\rho_i))}$$

$$\beta_i = \sqrt{(\mu_i/\rho_i)}$$

References

Agee, C. B., Petrology of the Mantle Transition zone, *Annu. Rev. Earth Planet. Sci.*, 21, 19-41, 1993

Anderson, D. L., Theory of the Earth, Blackwell Sci. Publ., 1989

Anderson, D. L., Lithosphere, asthenosphere and perisphere, *Reviews of Geophysics*, 33, 1, 125-149, 1995

Anderson, D. L. and Bass, J. D., Mineralogy and composition of the upper mantle, *Geophys. Res. Letts.*, 11, 7, 637-640, 1984

Anderson, D. L., and Dziewonski, A. M., Upper mantle anisotropy – evidence from free oscillations, *Geophys. J. R. astr. Soc.*, 69, 383-404, 1982

Artyushkov, E. V., On the origin of the seismic anisotropy of the lithosphere, *Geophys. J. R. astr. Soc.*, 76, 173-178, 1984

Babuska, V. and M. Cara., Seismic Anisotropy in the Earth, Kluwer Academic Publ., Boston, 1991

Backus, G. E., Long-wave elastic anisotropy produced by horizontal layering, *J. Geophys. Res.*,67, 4427-4440, 1962.

Bass, J. D. and Anderson, D. L., Composition of the upper mantle: geophysical tests of two petrological models, *Geophys. Res. Letts.*, 11, 3, 237-240, 1984

Bostock, M. G., Anisotropic upper-mantle stratigraphy and architecture of the Slave craton, *Nature*, 390, 392-395, 1997.

Christensen, N. I., and Salisbury, M. H., Seismic anisotropy in the oceanic upper mantle: evidence from the Bay of Islands ophiolite complex, *J. Geophys. Res.*, 84, 4601 – 4610, 1979

Chunduru R. K., Sen M. K. and Stoffa P. L., Hybrid optimization methods for geophysical inversion, *Geophysics*, 62, 4, 1196-1207, 1997

Duffy, T. S. and Anderson, D. L., Seismic velocities in mantle minerals and the mineralogy of the upper mantle, *J. Geophys. Res.*, 94, B2, 1895-1912, 1989

Ekstrom, G. and Dziewonski, A. M., The unique anisotropy of the Pacific upper mantle, *Nature*, 168-172, 1998

Estabrook, C. H. and Kind, R., The nature of the 660-kilometer upper mantle seismic discontinuity from precursors to the PP phase, *Science*, 274, 1179-1182, 1996

Estey, L. H., and Douglas, B. J., Upper mantle anisotropy: a preliminary model, *J. Geophys. Res.*, 91 (11), 11,393-11406, 1986.

Forsyth, D. W., The early structural evolution and anisotropy of the oceanic upper mantle, *Geophys. J. R. astr. Soc.*, 43, 103-162, 1975

Fuchs, K. and G. Muller, Computation of synthetic seismograms with the reflectivity method and comparison with observations, *Geophys. J. R. Astron. Soc.*, 23, 417-433, 1971.

Gaherty, J. B., and Jordan, T. H., Lehmann discontinuity as the base of an anisotropic layer beneath continents, Science, 268, 1468-1471, 1995

Gaherty, J. B., Kato, M., and Jordan, T. H., Seismological structure of the upper mantle: a regional comparison of seismic layering, *Phys. Earth Planet. Inter.*, 110, 21-41, 1999.

Gaherty, J. B., Wang, Y. B., Jordan, T. H., and Weidner, D. J., Testing plausible upper-mantle compositions using fine-scale models of the 410-km discontinuity, *Geophys. Res. Letts.*, 26, 11, 1641-1644, 1999

Gao, W., Grand, S. P.,Ni, J., Aster, R., Wilson, D., Schlue, J., Baldridge, S., Semken, S., Matzel, E., Mantle seismic structure beneath the Colorado Plateau, Rio Grande Rift and Great Plains from seismic tomography, Eos Trans. AGU, 82(47), Fall Meet. Suppl., Abstract S21F-07, 2001

Gauthier, O., Virieux, J., Tarantola, A., Two-dimensional nonlinear inversion of seismic waveforms: Numerical results, *Geophysics*, 51, 7, 1387-1403, 1986.

Ghose S., Hamburger M. W., Ammon C. J., Source parameters of moderate-sized earthquakes in the Tien Shan, central Asia from regional moment tensor inversion, *Geophys. Res. Letts.*, 25 (16), 3181-3184, 1998

Given, J. W. and Helmberger, D. V., Upper mantle structure of northwestern Eurasia, *J. Geophys. Res.*, 85, 7183-7194, 1980.

Glebovitsky, V. A., *The Early Precambrian of Russia*, Harwood Academic Publishers, 1997.

Grand, S. P. and Helmberger, D. V., Upper mantle shear structure of North America, *Geophys. J. R. Astron. Soc.*, 76, 399-438, 1984a.

Grand, S. P. and Helmberger, D. V., Upper mantle shear structure beneath the nortwest Atlantic ocean, *J. Geophys. Res.*, 89, 11,465-11,475, 1984b.

Ismail, W. B. and Mainprice, D., An olivine fabric database: an overview of upper mantle fabrics and seismic anisotropy, *Tectonophysics*, 296, 145-157, 1998

Ita, J. and Stixrude, L., Petrology, elasticity, and composition of the mantle transition zone, *J. Geophys. Res.*, 97, B5, 6849-6866, 1992

Jordan, T. H., Structure and formation of the continental tectosphere, *Journal of Petrology*, Special Lithosphere Issue, 11-37, 1988.

Jordan, T. H., The continental tectosphere, *Reviews of Geophysics*, 13, 1-12, 1975

Jordan, T. H., Saltzer, R. L., Gaherty, J. B., Small-scale anisotropic heterogeneity in the continental upper mantle, *Seismological Research Letters*, 70 (2), 259-260, 1999.

Karato, S., On the Lehmann discontinuity, *Geophys. Res. Letts.*, 19, 22, 2255-2258, 1992.

Kendall, J. M., and Silver, P. G., Constraints from seismic anisotropy on the nature of the lowermost mantle, *Nature*, 381, 409-412, 1996.

Kennett B.L.N., Engdahl E.R. and Buland R., Constraints on seismic velocities in the earth from travel times *Geophys. J. Int*, 122, 108-124, 1995

Kern, H., P and S wave anisotropy and shear wave splitting at pressure and temperature in possible mantle rocks and their relationship to the rock fabric, *Phys. Earth Planet. Inter.*, 87, 245-256, 1993

Knoche, R., Webb, S. L. and Rubie, D. C., Measurements of acoustic wave velocities at P-T conditions of the Earth's mantle, <u>Properties of Earth and Planetary Materials at High Pressure and Temperature</u>, Geophysical Monograph 101, AGU, 119-128, 1998

Kopylova, M. G., Russell, J.K. and Cookenboo, H., Upper mantle stratigraphy of the Slave craton, Canada: Insights into a new kimberlite province, *Geology*, 26, 4, 315-318, 1998 .

Kumazawa, M. and Anderson, O. L., Elastic moduli, pressure derivatives and temperature derivatives of single crystal olivine and single crystal forsterite, *J. Geophys. Res.*, 74, 5961-5971, 1969

Lay, T. and Helmberger, D. V., A lower mantle S-wave triplication and the shear velocity structure of D", *Geophys. J. R. Astron. Soc.*, 75, 799-837, 1983.

Leeds, A. R., Lithospheric thickness in the western Pacific, *Phys. Earth Planet. Inter.*, 11, 61-64, 1975

LeFevre, L. V. and Helmberger, D. V., Upper mantle P velocity structure of the Canadian shield, *J. Geophys. Res.*, 94, 17749-17765, 1989.

Li, A., Fischer, K. M., Wysession, M. E. and Clarke, T. J., Mantle discontinuities and temperature under the north American continental keel, *Nature*, 395, 160-163, 1998.

Li, B., Liebermann, R. C. and Weidner, D. J., Elastic Moduli of Wadsleyite (β-Mg_2SiO_4) to 7 Gigapascals and 873 Kelvin, *Science*, 281, 675-677, 1998b

Li, B., Chen, G., Gwanmesia, G. D., and Liebermann, R. C., Sound velocity measurements at mantle transition zone conditions of pressure and temperature using ultrasonic interferometry in a multianvil apparatus, Properties of Earth and Planetary Materials at High Pressure and Temperature, Geophysical Monograph 101, AGU, 41-59, 1998c

Long, C. and Christensen, N. I., Seismic anisotropy of South African upper mantle xenoliths, *EPSL*, 179, 551-565, 2000

Mainprice, D. and Silver, P. G., Interpretation of SKS-waves using smaples from the sub continental lithosphere, *Phys. Earth Planet. Inter.,* 78, 257 – 280, 1993

Marquering, H. and Snieder, R., Shear-wave velocity structure beneath Europe, the northeastern Atlantic and western Asia from waveform inversions including surface-wave mode coupling, *Geophys. J. Int.*, 127, 283-304,1996

Matzel, E., Sen, M. K. and Grand, S. P., Evidence for anisotropy in the deep mantle beneath Alaska, *Geophys. Res. Lett.,* 23, 18, 2417-2420, 1996

Mechie, J., Egorkin, A. V., Fuchs, K., Ryberg, T., Solodilov, L. and Wenzel, F., P-wave mantle velocity structure beneath northern Eurasia from long-range recordings along the profile QUARTZ, *Phys. Earth Planet. Inter.*, 79, 269-286, 1993

Ming, L. C., Madon, M. and Wang, L.-J., Phase transitions in a komatiite-rock at high pressures and high temperatures, <u>High Pressure Research: Application to Earth and Planetary Sciences</u>, AGU, 245-255, 1992

Montagner, J.-P., and Kennett, B. L. N., How to reconcile body wave and normal mode reference earth models, *Geophys. J. Int.*, 125, 229-248, 1996

Montagner, J.-P., Nataf, H. C., A simple method for inverting the azimuthal anisotropy of surface waves, *J. Geophys. Res.*, 91, 511-520, 1986.

Montagner, J-P., and Tanimoto, T., Global upper mantle tomography of seismic velocities and anisotropies, *J. Geophys. Res.*, 96, B12, 20,337-20,351, 1991.

Mooney, W. D., Laske, G., Masters, T. G., CRUST 5.1; a global crustal model at 5 degrees X5 degrees, *J. Geophys. Res.*, 103, 727-747, 1998.

Mora, P. Elastic wave-field inversion of reflection and transmission data, *Geophysics*, 53, 6, 750-759, 1988.

Morozova, E. A., Morozov, I. B., Smithson, S. B. and Solodilov, L. N., Heterogeneity of the uppermost mantle beneath Russian Eurasia from the ultra-long-range profile QUARTZ, *J. Geophys. Res*., 104, B9, 20,329-20,348, 1999.

Nataf, H.-C., Nakanishi, I. and Anderson, D. L., Measurements of mantle wave velocities and inversion for lateral heterogeneities and anisotropy: 3. Inversion, *J. Geophys. Res.*, 91, 7261-7307, 1986

Nicolas, A. and Christensen, N. I., Formation of anisotropy in upper mantle peridotites: A review, Composition, *Structure and Dynamics of the Lithosphere-Asthenosphere System*, 111-123, 1987.

O'Reilly, S. Y., Griffin, W. L., 4-D Lithosphere Mapping: methodology and examples, *Tectonophysics*, 262, 3-18, 1996.

Paulssen, H., Lateral heterogeneity of Europe's upper mantle as inferred from modelling of broad-band body waves, *Geophys. J. R. astr. Soc.*, 91, 171-199, 1987

Paulssen, H., Bukchin, B. G., Emelianov, A. P., Lazarenko, M., Muyzert, E., Snieder, R., Yanovskaya, T. B., The NARS-DEEP project, *Tectonophysics*, 313, 1-8, 1999

Pavlenkova, N. I. and Yegorkin, A. V., Upper mantle heterogeneity in the northern par of Eurasia, *Phys. Earth Planet. Inter.*, 33, 180-193, 1983

Peselnik, L. and Nicolas, A., Seismic anisotropy in an ophiolite peridotite: application to oceanic upper mantle, *J. Geophys. Res.*, 83, 1227-1235

Pica, A., Diet, J. P., Tarantola, A., Nonlinear inversion of seismic reflection data in a laterally invariant medium, *Geophysics*, 55, 3, 284-292, 1990.

Priestley, K., Velocity structure of the continental upper mantle: evidence from southern Africa, *Lithos*, 48, 45-56, 1999

Qiu, X., Priestley, K., and McKenzie, D., Average lithospheric structure of southern Africa, *Geophys. J. Int*., 127, 563-558, 1996.

Randall, G. E., Efficient calculation of complete differential seismograms for laterally homogeneous earth models, *Geophys. J. Int*., 118, 245-254, 1994.

Regan, J. and D. J. Anderson, Anisotropic models of the upper mantle, *Phys. Earth Planet. Inter.*, 35, 227-263, 1984

Ringwood, A. E., <u>Composition and petrology of the Earth's mantle</u>, McGraw-Hill Inc., 1975

Ritsema, J., Nyblade, A. A., Owens, T. J., Langston, C. A., VanDecar, J. C., Upper mantle seismic velocity structure beneath Tanzania, East Africa; implications for the stability of cratonic lithosphere, *J. Geophys. Res.*, 103, 21,201-21,213, 1998.

Rodgers, A. and Bhattacharyya, J., Upper mantle shear and compressional velocity structure of the Central US Craton: Shear wave low-velocity zone and anisotropy, *Geophys. Res. Letts.*, 28, 2, 383-386, 2001

Rodgers A. J., Walter W. R., Mellors R. J., Al-Amri A. M. S. and Zhang Y. S., Lithospheric structure of the Arabian Shield and Platform from complete regional waveform modelling and surface wave group velocities, *Geophys. J. Int*., 38 (3), 871-878, 1999

Roult, G., Rouland, D. and Montagner, J. P., Antarctica II: Upper-mantle structure from velocities and anisotropy, *Phys. Earth Planet. Inter.*, 84, 33-57, 1994.

Ryberg, T., Fuchs, K., Egorkin, A. V. and Solodilov, L., Observation of high-frequency teleseismic Pn on the long-range Quartz profile across norther Eurasia, *J. Geophys. Res*., 100, B9, 18,151-18,163, 1995

Ryberg, T., Wenzel, F., Egorkin, A. V. and Solodilov, L., Properties of the mantle transition zone in northern Eurasia, *J. Geophys. Res*., 103, B1, 811-822, 1998

Saltzer, R. L., Gaherty, J. B., Jordan, T. H., How are vertical shear wave splitting measurements affected by variations in the orientation of azimuthal anisotropy and depth?, *Geophys J. Int.*, 141 (2), 374-390, 2000.

Sen, M. and Stoffa, P. L., *Global optimization methods in geophysical inversion*, Elsevier, 1995.

Silver, P. G., Seismic anisotropy beneath the continents: probing the depths of geology, *Annu. Rev. Earth Planet. Sci.* 24, 385-432, 1996.

Simons, F. J., Zielhuis, A. and van der Hilst, R. D., The deep structure of the Australian continent from surface wave tomography, *Lithos*, 48, 17-43, 1999

Swenson J. L., Beck S. L. and Zandt G., Regional distance shear-coupled PL propagation within the northern Altiplano, central Andes, *Geophys. J. Int*., 139, 3, 743-753, 1999

Tarantola, A., The seismic reflection inverse problem, Inverse problems of acoustic and elastic waves, Soc. Industr. Appl. Mech.,104-181, 1984

van der Lee, S. and Nolet, G., Upper mantle S velocity structure of North America, *J. Geophys. Res.*, 102, 22,815-22,838, 1997.

Vinnik, L. P., Green, R. W. E., Nicolaysen, L. O., Kosarev, G. L., Petersen, N. V., Deep seismic structure of the Kaapvaal craton, *Tectonophysics*, 262, 67-75, 1996

Vinnik, L. P., Ryaboy, V. Z., Deep structure of the East European platform according to seismic data, *Phys Earth Planet. Inter.*, 25, 27-37, 1981

Walck, M. C., The P-wave upper mantle structure beneath an active spreading center - the Gulf of California, *Geophys. J. R. astr. Soc.*, 76, 697-723, 1984

Weidner, D., and Ito, E., Mineral physics constraints on a uniform mantle composition, High Pressure Research in Mineral Physics, 439-446, 1987

Xu, Y. B., and Wiens, D. A., Upper mantle structure of the southwest Pacific from regional waveform inversion, *J. Geophys. Res.*, 102, B12, 27,439-27,451, 1997

Zeng, Y. H. and Anderson, J. G., A method for direct computation of the differential seismogram with respect to the velocity change in a layered elastic solid, *Bull. Seism. Soc. Am.*, 85(1), 300-307, 1995

Zhao, L. S. and Helmberger, D. V., Upper mantle compressional velocity structure beneath the northwest Atlantic ocean, *J. Geophys. Res.*, 98, B8, 14,185-14,196, 1993

Zhao, M., Langston, C. A., and Nyblade, A. A., and Owens, T. J., Upper mantle velocity structure beneath southern Africa from modeling regional seismic data, *J. Geophys. Res.*, 104, 4793-4794, 1999.

Zonenshain, L. P., Kuzmin, M. I. and Natapov, L. M., *Geology of the USSR: A plate-tectonic synthesis*, Geodynamics Series Volume 21, 1990.

VITA

Eric M. Matzel was born in Washington, D.C. on January 30th, 1966, to Julie and Gerhard Matzel. He was raised in Boston, Massachusetts where he quickly developed a love of science. He attended public elementary and high schools in the city and graduated from Boston Latin Academy in 1984.

In August, 1984, he began his undergraduate studies at the University of Texas majoring in physics, but he gradually became more interested in geology and geophysics. He changed his major in 1987 and graduated with a bachelor's degree from the Department of Geological Sciences in 1989.

Upon graduating, he traveled to Tucson, Arizona where he spent a year and a half working as a research assistant at the Planetary Science Institute, studying the dynamics of asteroids. He also spent 6 months in Tennessee working as a geologist for the U.S. Army Corps of Engineers before returning to the University to pursue a graduate education. He received a Master's degree in May, 1997 and decided to continue research as a doctoral student.

Permanent Address: 6 Fairfax St., Boston, Ma. 02124
This dissertation was typed by the author.